Funded by
the European Union

TWIN-IT-ROMANS - 101160215

Technical Output Report 1

Rev-A

30.09.2025

Prepared by Gizem Gündüz, Berk Kurt, Hasan Cezayirli
Controlled by Gökhan Kiper, Halil Tetik, Büşra Karaş
Approved by Mehmet İsmet Can DEDE

1. EXPLANATION OF THE TECHNICAL WORK CARRIED OUT AND OVERVIEW OF THE TECHNICAL PROGRESS

1.1 Objectives Related to Technical Aspects of the Project

Work Package 2 (WP2) is the work package where the technical aspects of the project are carried out. The objective of the technical work is defined as follows: To step up and stimulate the scientific excellence and innovation capacity of the partners in the area of robotic systems in manufacturing and quality control, a fundamental part of the activities will be realized within the research project described in this work package. Improving S&T capacity of all partners by working on the research project aiming at the development of a highly innovative and sustainable TWIN-IT-ROMANS system, including a novel interchangeable toolhead, user interface, and inline quality control.

1.1.1 Summary of progress towards the achievement of the objectives

During the 1st year of the project, studies within WP2 are carried out in the following tasks: (1) Robot Cell Design, (2) Digital Twin and In-line Quality Control, (3) Investigation of Sustainability, (4) Prototype Development, and (5) System Integration and Demonstration. In all tasks, progress has been achieved. Robot cell design in Austria has already been established, and the cell design in Türkiye was carried out during the 1st year of the project. The components have been identified, and most of them are built or purchased. Inline quality control studies are initiated in the additive manufacturing domain. The possible defects during the additive manufacturing process have been identified, and a sample study has been conducted to train an AI-based model. The sustainability aims of the projects were established during the Workshop on Sustainability organized by POLITO. As an outcome of this study, a review paper on sustainability issues in additive manufacturing was published in a related conference. The robotic hybrid manufacturing prototype in Austria was developed by MCI, which is capable of performing additive and subtractive manufacturing operations using thermoplastic polymers as raw material and obtaining final products with enhanced surface quality and improved geometrical tolerances. The robotic hybrid manufacturing prototype in Türkiye is being developed at IZTECH with the assistance of HKTM. The expected date for the functional prototype is before the end of 2025. As the final prototype becomes functional, preliminary experiments on additive and subtractive manufacturing of fiber-reinforced thermoplastic composites will be carried out, and process parameter optimization studies will be performed. Following, via the embedded in-line quality control tools, process data will be obtained for developing AI models to estimate the condition of the final product before its use. The system at MCI has been integrated in terms of its manufacturing modes, and an initial demonstration has been carried out during the Summer School event at MCI. The information exchange and connection of components plan for the prototype in IZTECH has been formulated, and in the next months this plan will be implemented.

1.2 Explanation of the work carried out per task within WP2

The work carried out in every task of WP2 within the 1st year of the project is explained in the next subsections.

1.2.1 Robot Cell Design (T2.1) (M1-M36)

Objectives: In this task, a multi-axis positioner with the collaborative robot manipulator is modelled. Tool head design that can be interchangeable, adaptive, compact, and capable of precise production (Lead by POLITO). Finally, an algorithm to optimize tool head trajectory (depending on the desired manufacturing method) will be developed in the most sensitive, fast, and energy efficient way of the targeted operation (led by RWTH).

1.2.1.1. Selection of robotic cell

In the robot selection process, a detailed evaluation was conducted to match the operational requirements of the proposed robotic cell with the capabilities of available collaborative robots. As illustrated in Figure 1.2.1.1.1, 1.2.1.1.2, and 1.2.1.1.3, the machining of fiber composite materials is associated with cutting forces in the range of 80–100 N, which sets a critical design constraint for the robotic system. The selected cobot must therefore not only provide sufficient payload and stiffness to withstand these forces but also maintain high precision and reliability during continuous operation.

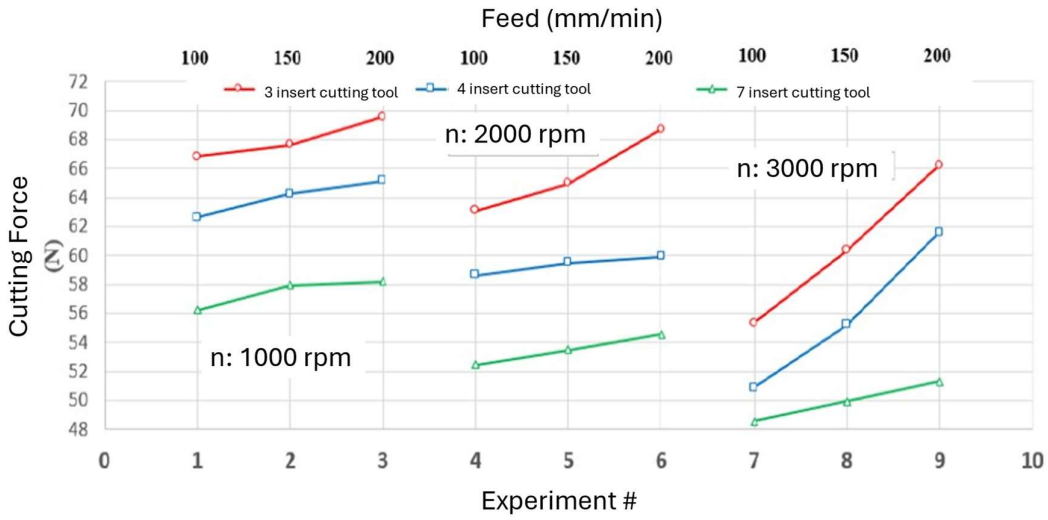

Figure 1.2.1.1.1. Cutting force of composite material [2]

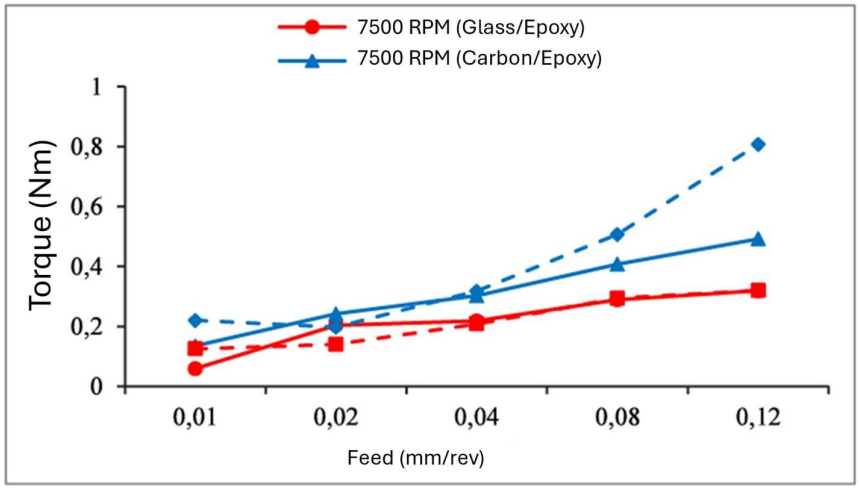

Figure 1.2.1.1.2. Cutting moment of composite material [2]

To support the selection, Table 1.2.1.1.1 presents a comparative overview of commercially available collaborative robots, with emphasis on payload, reach, control features, and the presence of synchronous auxiliary motors. This aspect is particularly significant, since the concept design foresees the integration of a redundant manipulator system in which the cobot must operate in synchronization with an additional positioner. Such coordination requires advanced motion control features that are not universally available among cobot manufacturers.

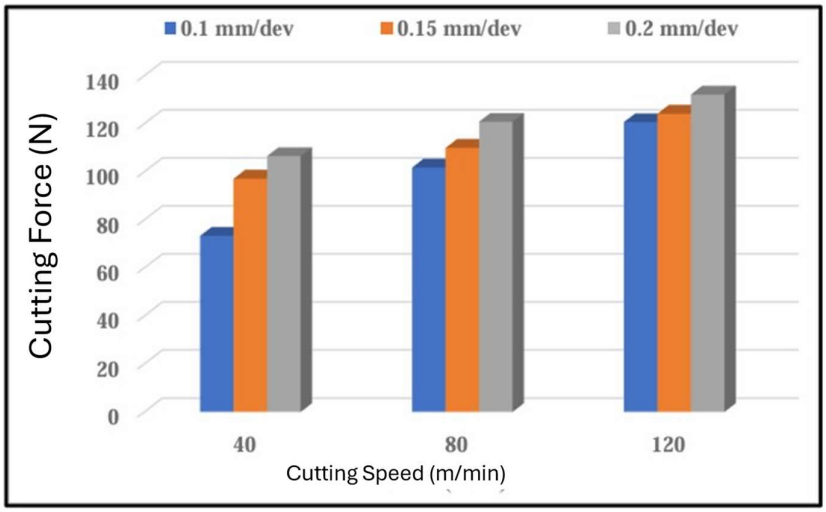

Figure 1.2.1.1.3. Cutting force of peek material [3]

Table 1.2.1.1.1. Possible robot options

#	Brand	Model	Payload (kg)	Reach (mm)	Repetability (± mm)	Is addtional Positioner possible	Synchronous / Positioning
1	FANUC	CRX-30iA	30	1756	0.05	Evet	Synchronous
2	HAN's Robot	S30	30	1800	0.05	-	-
3	AUBO	i20	20	1650	0.1	-	-
4	TM Robots	TM30S	30	1702	0.03	Evet	Positioning
5	Omron	RT6	20	1300	0.1	-	-
6	UR	UR30	30	1300	0.1	Evet	Positioning
7	Kuka	LBR iisy 15 R930	15	930	0.05	-	-
8	Doosan	H2515	25	1500	0.1	Evet	Positioning
9	Schneider	Lexium 18	18	1073	0.02	-	-

Upon review of the technical specifications, it was identified that only Fanuc offers the required capability of synchronous auxiliary motor control while simultaneously fulfilling the payload and precision demands dictated by the machining of fiber composites. On this basis, the Fanuc cobot was selected as the most suitable option, ensuring compatibility with both the machining requirements and the integrated system design of the robotic cell.

1.2.1.2. Positioner design

In the positioner design, several critical factors must be carefully considered to ensure both functional performance and seamless integration with the robotic cell. One of the foremost aspects is the dimensioning of the worktable. The table must be designed with sufficient surface area to accommodate the range of workpieces, including composite and plastic parts of varying geometries, while maintaining rigidity under operational loads. A well-dimensioned table not only provides stability during machining but also enhances the accuracy and repeatability of the entire process.

As part of the initial production planning, the first end product to be manufactured within the scope of the project has been defined as the “Naka profile” component, which was proposed by HKTM. This part has approximate dimensions of 50 × 50 × 150 mm, making it a representative benchmark for both design validation and process capability assessment. Since it reflects a realistic use case in terms of geometry and material, the airfoil profile has been strategically selected as the pilot component to evaluate the performance of the robotic cell under near-industrial conditions.

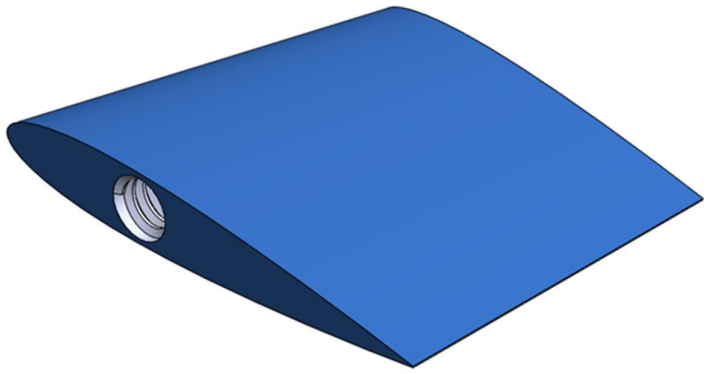

Figure 1.2.1.2.1. Airfoil Profile from HKTM

To accommodate the manufacturing of this component, particular attention was given to the worktable design. While the dimensions of the airfoil profile itself are relatively moderate, it was recognized that future operations would likely involve parts of different geometries and sizes. Therefore, the table was designed not only to meet the immediate requirements of this specific component but also to provide scalability and flexibility for subsequent use cases. In this context, the general industry-standard 3D printer table size of 300 × 300 mm was adopted as the design reference. This choice provides sufficient space for the airfoil profile while also ensuring compatibility with larger workpieces that may be introduced in later project phases.

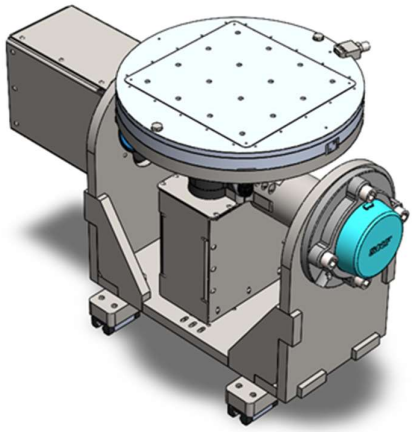

Figure 1.2.1.2.2. Positioner Design-1

The development of such a table required careful consideration of structural rigidity, thermal stability, and load distribution. The enlarged table surface enables multiple orientations of the part, which is particularly important for adaptive fixturing and for ensuring accessibility of the cobot and machining tools. At the same time, the increased table area necessitated enhancements in the support structure to minimize deflection and vibration during machining. By combining these design improvements with a temperature-controlled surface, the table was optimized for both composite processing and plastic additive manufacturing, thus extending its functionality beyond the immediate needs of the pilot part.

Through these measures, the positioner and its table have been tailored not only to the specific requirements of the airfoil profile but also to establish a versatile platform capable of addressing a wide range of parts and applications in the future. This ensures that the initial investment in development contributes directly to the scalability and long-term sustainability of the robotic cell concept.

In conclusion, the dynamic evaluation confirmed that the positioner operates well within the defined torque limits, and the obtained results indicate that the overall dynamic performance is satisfactory and consistent with the design objectives. The complete integrated design, including detailed schematics and supporting data, is provided in Appendix A.

1.2.1.3. Description of robotic cell

The robotic arm is placed in a cell specially designed for safety and functionality. Various components, enabling both additive and subtractive manufacturing, were planned to be added to the robotic cell. Appropriate locations for each component were determined and placed within the CAD model cell. Figure 1.2.1.3.1. shows the CAD model. Detailed information about the components in the robotic cell is available in Appendix B.

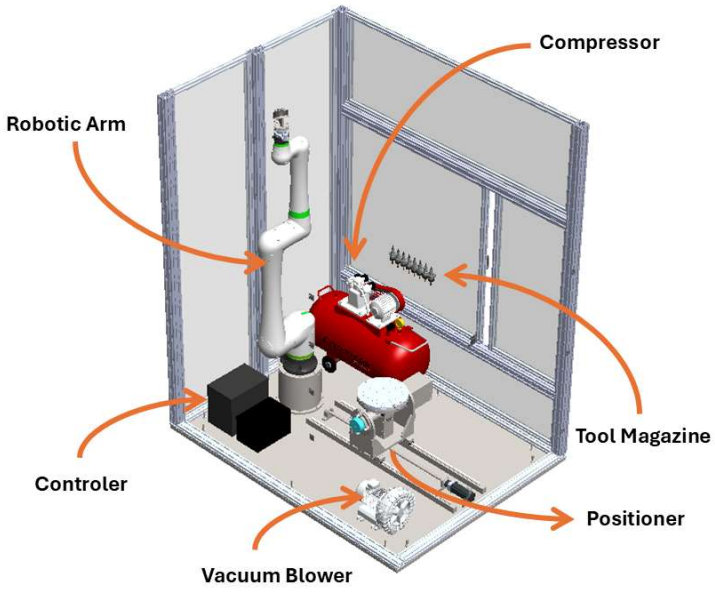

Figure 1.2.1.3.1. CAD model of robotic cell

Kinematic model of arm and positioner

To analyze the robotic system, forward and inverse kinematic models were created for both the robot and the 2R positioner. Determining the robotic arm's workspace, optimizing the distance between the robot and positioner, and the initial steps for path planning were carried out using the obtained inverse and forward equations. The procedures for obtaining inverse and forward kinematics are shown in Appendix C. Inverse and forward kinematics simulations for the robotic arm were created using both Excel and MATLAB. Figure 1.2.1.3.2. shows the MATLAB simulation.

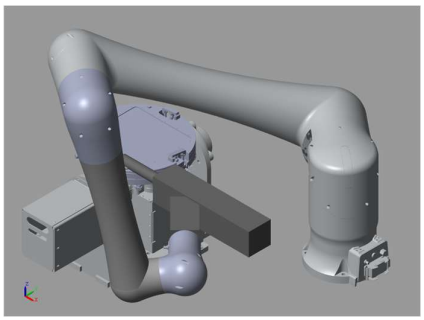

Figure 1.2.1.3.2. Image of robotic arm and positioner in MATLAB simulation

Parameters of the relative position of arm and positioner + initial results

Various design parameters were considered to optimize the distance between the positioner and the robot arm. These parameters directly impact the system's accessibility. The relevant parameters are presented in detail in Figure 1.2.1.3.3. This image provides a clearer picture of the robotic cell's geometric layout and the relationships between its components. During the simulation d_m, $d_{d1} + d_{d2}$ and d_{d3} are used as d_m = 200 mm, $d_{d1} + d_{d2}$ = 350 mm and d_{d3} = 53.5 mm. For the variable parameters are used as x_v = 700 / 800 / 900 / 1000 mm, z_v = 325 / 477.5 / 600 mm, α_d = 30° / 45°. By changing these parameters, the Collisions, Condition number and Manipulability values at certain end-effector points are examined.

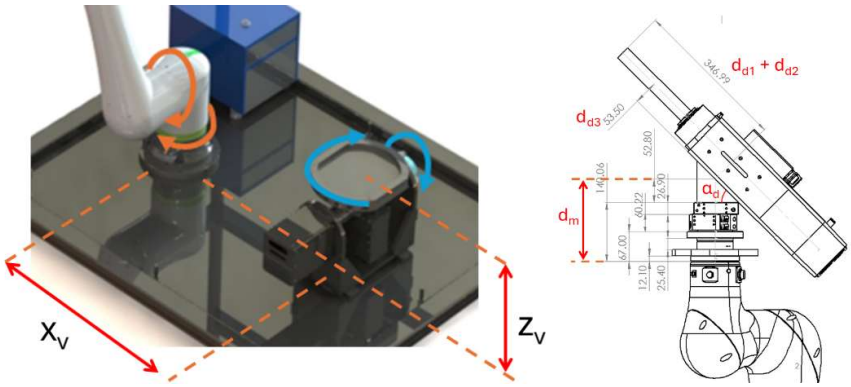

Figure 1.2.1.3.3. Optimization parameters

1.2.1.4. 3D Printer head design

The development of the 3D printer head focused on creating a versatile and functional design capable of processing both fiber composite and plastic materials, while integrating additional features to enhance performance and monitoring capability.

In the developed system, a total of four motors were integrated to enable precise control of the printing process. Of these, three motors drive the filament feed, while one motor adjusts the roller distance to regulate material flow. In addition, the print head incorporates a fiber cutter, allowing for controlled processing of continuous fiber materials.

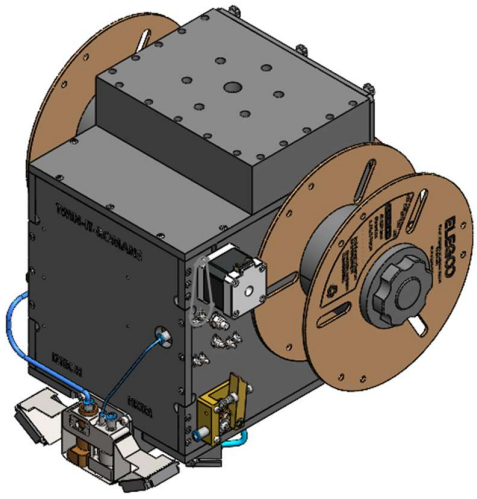

Figure 1.2.1.4.1**.** CAD Design of the 3D Printer Head

The synchronized operation of the motors, combined with the temperature control of the 3D printer, enables the printing process to be initiated reliably. To enhance process monitoring, a force sensor was added to the roller assembly, making it possible to track and regulate the applied force during printing. Furthermore, a retraction mechanism was integrated into the roller design to prevent excessive deposition of material, thereby ensuring print accuracy and surface quality.

Overall, these enhancements provide a printing head that not only supports fiber composite and plastic processing but also incorporates advanced control and monitoring features, improving both performance and reliability of the system.

1.2.1.5. CAD Design of the subtractive head

In the spindle selection process, special consideration was given to the integration of an interchangeable tool-changing mechanism. Such a feature is highly valuable for machining operations, as it enables the use of multiple tools within the same setup, significantly increasing flexibility and reducing downtime. However, the addition of this mechanism also increases the overall mass of the spindle assembly, making it essential to remain within the payload limits of the collaborative robot to ensure stable and safe operation.

After a detailed evaluation, the HS315 spindle from Hertz was selected. This spindle offers the required speed and torque performance while supporting automatic tool changing. Its total weight of approximately 16 kg remains well below the 30 kg payload capacity of the robot, ensuring that the system can accommodate not only the spindle itself but also the additional tool-changing mechanism and tooling without exceeding safe operating limits.

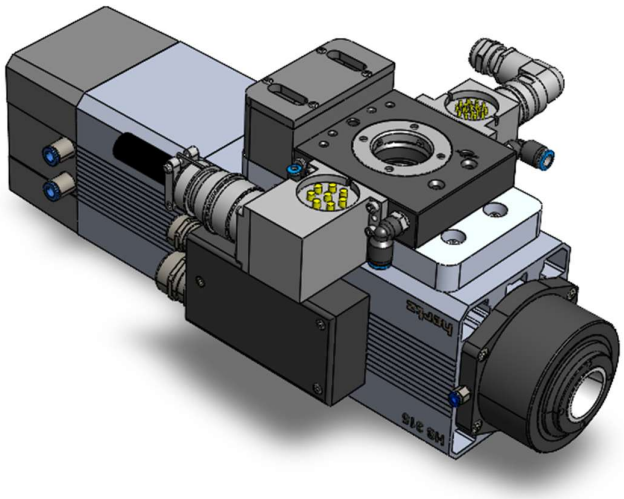

Figure 1.2.1.5.1. CAD Design of the Subtractive Tool Head

For the tool interface, the BT30 tool standard was chosen. This specification provides a well-balanced solution, offering sufficient rigidity for machining fiber composites and plastics, while also being lighter than larger alternatives such as BT40. The BT30 system is widely adopted, ensuring compatibility with a broad range of cutting tools and reliable tool clamping during operation.

In summary, the combination of the Hertz HS315 spindle with BT30 tooling delivers a robust, lightweight, and versatile solution that aligns with both the technical requirements of the subtractive head and the load constraints of the collaborative robot.

1.2.1.6. Gripper system design

To handle both the build plate and various auxiliary equipment required during the manufacturing process, a universal gripper head was selected from Schunk. This gripper is driven by pneumatic actuation, providing a robust and responsive solution for securely holding components of different shapes and sizes. The use of pneumatic actuation ensures quick gripping and releasing actions, which are essential for efficient operation in the robotic cell.

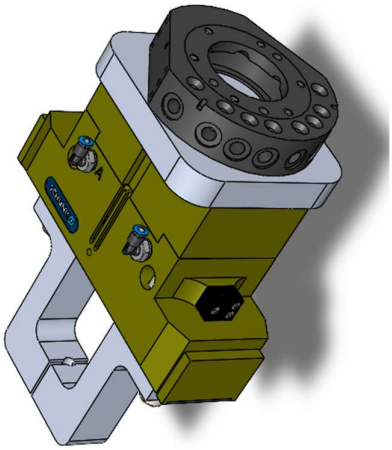

Figure 1.2.1.6.1. CAD Design of the Gripper Tool Head

The universal configuration of the Schunk gripper allows it to adapt to multiple applications without requiring frequent end-effector changes. This flexibility is critical for the proposed system, where the same gripper may be used to fix the build plate in place, transfer workpieces, or manipulate auxiliary tools and fixtures.

In addition, Schunk grippers are recognized for their high precision, durability, and repeatability, ensuring stable performance even under demanding industrial conditions. By integrating this gripper, the robotic cell gains the capability to perform a wide range of handling tasks, thereby enhancing its versatility and overall system efficiency.

1.2.1.7. Interchangeable Tool Head Design

Since the robotic cell is based on a single robot that must perform multiple operations, an interchangeable tool head system is required to switch between different end-effectors efficiently. This solution eliminates the need for multiple dedicated robots and ensures flexibility, adaptability, and space efficiency within the cell.

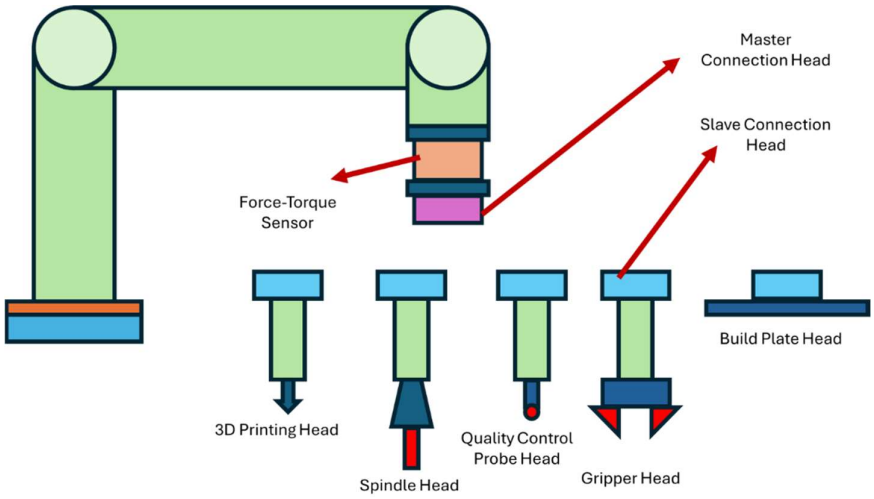

Figure 1.2.1.7. 1. Concept design of interchangeable toolheads

For this purpose, the SWA/K 40 model from Schunk was selected. This tool changer provides a payload capacity of up to 50 kg, which is well above the requirements of the current system, ensuring both reliability and a sufficient safety margin. Beyond its mechanical load-bearing ability, the SWA/K 40 also enables the transfer of power, data, and media flow (such as pneumatic or vacuum lines), making it suitable for supporting a wide range of tool heads, including the 3D printing head, subtractive spindle head, vacuum system, and gripper modules.

The integration of such a tool-changing system offers several advantages:

→ Operational flexibility, allowing seamless switching between additive, subtractive, and handling tasks.

→ Reduced downtime, since tool changes can be executed automatically without manual intervention.

→ Enhanced system integration, as power and communication lines are directly routed through the tool changer, minimizing external cabling and potential failure points.

→ Future scalability, with the capacity to integrate additional tool heads as new processes are introduced.

In summary, the Schunk SWA/K 40 was chosen as the optimal solution, providing the required strength, versatility, and connectivity to support the multifunctional operations of the robotic cell.

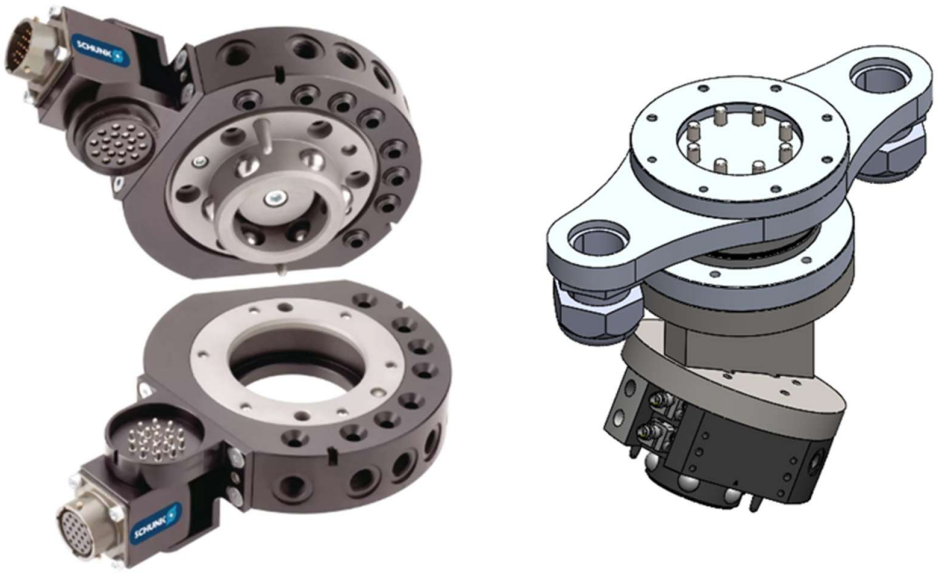

Figure 1.2.1.7.2. Schunk Interchangeable Toolheads

1.2.1.8. Vacuum System Design

During the machining and processing of composite materials, fine dust particles and fumes are released into the environment. Many of these particles are classified as carcinogenic,

particularly those originating from carbon fibers and resin-based matrices. If not properly managed, they pose serious risks both to human health and to the long-term reliability of sensitive equipment. Therefore, an integrated vacuum system was designed to ensure safe operation by removing these hazardous particles directly from the production environment.

The system consists of three main components: a vacuum blower, a filter unit, and a vacuum relief valve. The selected 0.85 kW Aduvac vacuum blower provides sufficient suction capacity to continuously extract airborne particles generated during cutting, drilling, or surface finishing of fiber composites. This blower maintains stable negative pressure within the system, ensuring that harmful particles are directed away from the operator and the robotic cell.

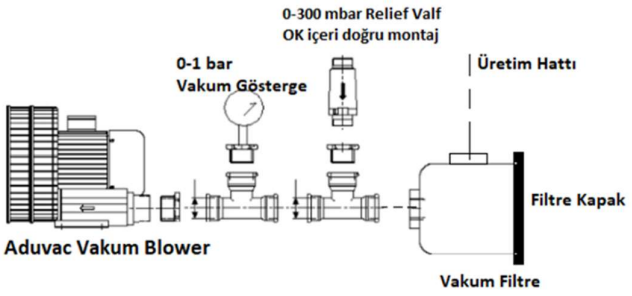

Figure 1.2.1.8.1. Vacuum system design

The extracted particles are collected in a vacuum filter equipped with a removable filter cap. This filter captures both coarse and fine particles, preventing them from being released back into the environment and protecting downstream equipment from contamination. The filter system is designed for easy maintenance, enabling periodic replacement or cleaning of the filter elements.

To ensure safe operation and protect the blower against overload, a vacuum relief valve (0–300 mbar) and a vacuum gauge (0–1 bar) were integrated into the system. These components allow real-time monitoring of vacuum pressure and provide a controlled pressure release in case of blockages or excessive suction. By doing so, they safeguard both the equipment and the operators, while maintaining a stable and efficient filtration process.

Figure 1.2.1.8.2. Advance Vacuum Blower

Overall, the designed vacuum system ensures that carcinogenic composite particles are effectively collected and removed, significantly improving workplace safety and compliance

with occupational health standards. By combining reliable suction, effective filtration, and safety mechanisms, this system provides a robust and sustainable solution for the safe processing of composite materials in the robotic cell.

1.2.1.9. Adaptive Fixture Subsystem

In order to ensure secure clamping of complex geometries produced by additive manufacturing, the project focuses on the development of adaptive fixtures. Unlike conventional universal fixtures, which are typically limited to simple shapes, the proposed system is designed to conform to irregular and intricate part geometries, thereby enabling accurate positioning during subsequent machining operations.

The current approach under investigation is based on vacuum-assisted granular jamming. In this method, a flexible membrane filled with particulate material can transition between a compliant and a rigid state depending on the applied vacuum. When a vacuum is applied, the grains interlock and form a solid-like structure that tightly conforms to the surface of the part, thereby providing a custom-fit support for each geometry. This principle offers a versatile solution for handling the highly variable and freeform designs that are common in composite and plastic additive manufacturing.

Different filler media are being explored to optimize fixture performance. Options include:

- Granular particles (e.g., sand, glass beads, or polymer granules) for simple and cost-effective implementation.
- Fibers (short or long) to improve the adaptability and load distribution characteristics of the fixture.
- Layered structures that combine rigid and compliant materials to achieve tailored stiffness.
- Hybrid approaches, where grains are mixed with fibers or layers, provide both fine adaptability and structural reinforcement.

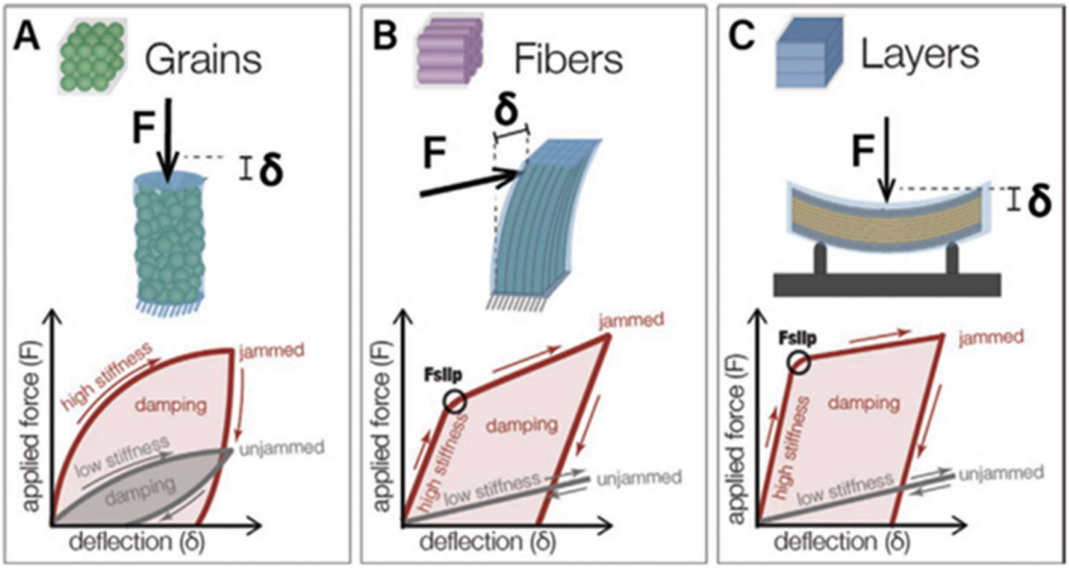

Figure 1.2.1.9.1. Different filler media of Jamming [1]

The literature review on adaptive fixtures has already been completed, and a basic test system for granular jamming is currently being developed. Once the prototype is ready, experimental tests will begin to evaluate different material types and fixture configurations.

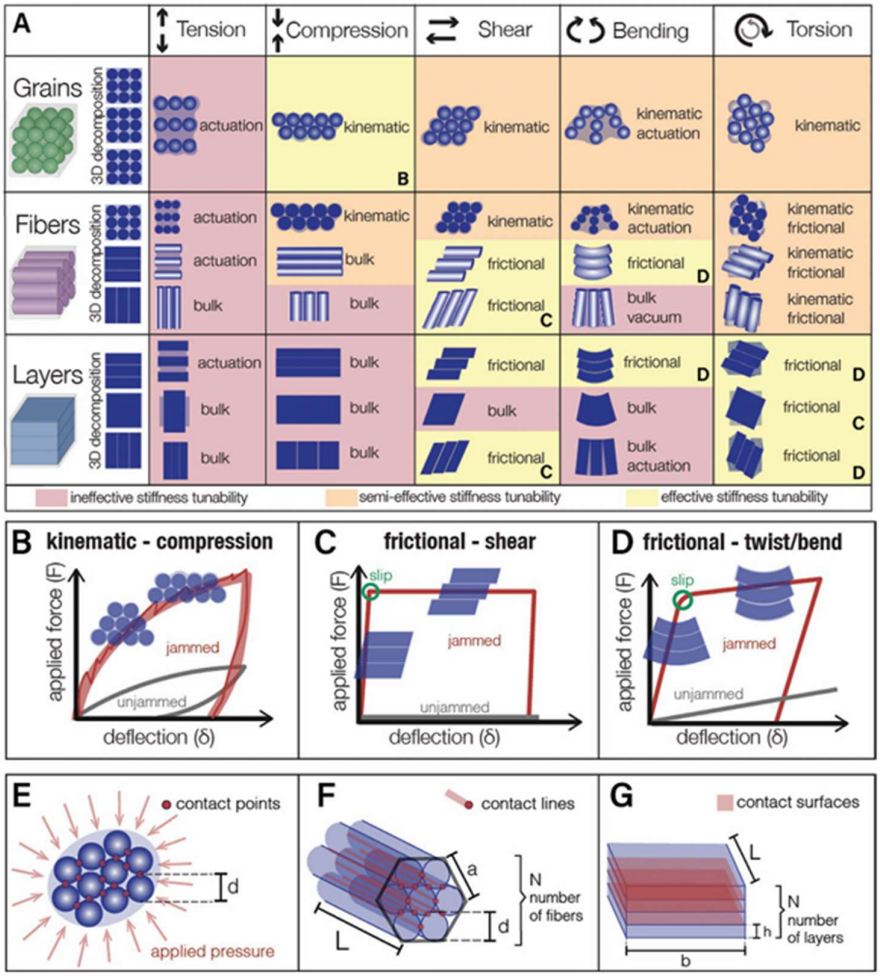

Figure 1.2.1.9.2. Stiffness Tunability Mechanisms for Adaptive Fixtures Using Grains, Fibers, and Layers [1]A1

Overall, the adaptive fixture development aims to create a flexible, reconfigurable, and reliable clamping system capable of handling the unique challenges posed by complex additively manufactured geometries.

1.2.1.10. Screwing System Design

Although adaptive fixture technologies such as granular jamming, fiber-based supports, or hybrid approaches provide significant flexibility in clamping complex geometries, they cannot guarantee flawless operation under all conditions. For instance, in some cases, highly irregular surfaces, extreme stiffness variations, or excessive local loads may lead to insufficient support or even fixture failure. In such scenarios, relying solely on adaptive methods could compromise the accuracy, surface quality, or overall stability of the machining or additive manufacturing process.

To address these limitations, an additional screwing system is considered essential as a complementary solution. This system functions as a more rigid and fail-safe method by mechanically fastening the produced part directly to the base or worktable. Using screw-type anchoring points, the part can be firmly fixed in place, independent of its geometry or surface condition. As a result, even if the adaptive fixture underperforms, the screwing system ensures that the part remains securely held during machining, preventing vibration, slippage, or displacement.

The inclusion of a screwing system also increases the versatility and reliability of the overall clamping strategy. It enables the fixture to handle not only standard geometries but also outlier cases where adaptive solutions may prove inadequate. In practice, this system can be used either as a primary clamping method for challenging parts or as a redundant safety mechanism in combination with adaptive fixtures.

In summary, while adaptive fixtures provide flexibility and efficiency, their potential limitations necessitate the integration of a screwing-based fixation system. This dual approach ensures that robotic cell can accommodate a wide spectrum of geometries and materials, thereby enhancing process robustness, operator safety, and product quality.

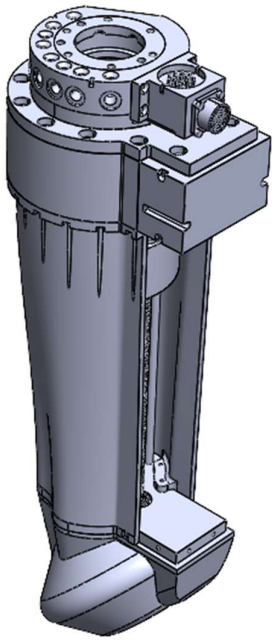

Figure 1.2.1.10.1. CAD Design of the Screwing System

1.2.1.11. Overall Cell Design

The overall robotic cell was designed to ensure that all subsystems are integrated in a safe, efficient, and ergonomic manner. The enclosure provides both operator safety and environmental isolation, while transparent side panels enable continuous monitoring of the internal processes. All essential units, including the collaborative robot, positioner, vacuum

system, compressor, and auxiliary equipment, have been arranged in accordance with functional and safety requirements.

An important feature of the design is the introduction of a single-axis linear guide between the positioner and the robot. This axis allows the robot to adjust its reach according to the specific tool head or fixture in use. Since the effective working distance varies depending on whether the robot is operating with the printing head, subtractive spindle head, or handling/gripping tools, the additional linear degree of freedom ensures that the robot can maintain optimal working positions across all tasks.

This configuration not only extends the operational flexibility of the robotic cell but also minimizes repositioning errors and maximizes the utilization of the robot's payload and reach capacity. By combining safety, accessibility, and adaptability in the layout, the developed cell establishes a robust foundation for performing additive, subtractive, and hybrid manufacturing processes in a single integrated environment.

1.2.1.12. Future Works on the Robot Cell System

For the upcoming term, the focus will be on further strengthening the system by addressing three major objectives.

First, efforts will be directed toward gaining know-how in adaptive fixture technologies. This will involve the development of a dedicated test system to evaluate different approaches such as granular jamming, fiber-based solutions, and hybrid methods. Experimental validation will provide critical insights into the performance, reliability, and applicability of these fixture concepts for complex geometries.

Second, the design of the robotic system will be finalized. This includes the mechanical arrangement of the robot, positioner, and auxiliary subsystems within the cell. By completing the design phase, the system layout will be ready for transition into prototype assembly and subsequent experimental trials.

Finally, significant emphasis will be placed on the integration of the robotic system with the Beckhoff control platform. Achieving real-time operation through this integration will be a major milestone, as it will enable synchronized control of tool heads, fixtures, and process monitoring modules. This step will also pave the way for advanced control strategies and virtual commissioning through digital twin technologies.

Together, these activities will ensure that the project progresses from subsystem-level developments toward a fully integrated, operational robotic cell capable of supporting advanced hybrid manufacturing processes.

1.2.2 Digital Twin and In-line Quality Control (T2.2) (M1-M36)

Objectives: This task aims to develop a digital twin platform that incorporates advanced machine-to-machine connectivity and AI-enabled in-line process quality control and monitoring capabilities (led by LSBU). The digital twin will be constructed utilising the latest industrial OPC-UA architecture, incorporating a 3D kinematic model capable of real-time functionality, and equipped with the capability to collect and retain operational data in diverse time-series databases. As an integral component of this WP, there will be a development of an

industrial gateway and communication platform. Moreover, the digital twin will be integrated with a machine learning-based quality control detection algorithm for the purpose of achieving the goals of zero-defect manufacturing. A range of dashboards and alerts will be developed to effectively communicate and notify operators/managers regarding the quality-related issues. The implementation of this WP will facilitate the integration of an in-line process quality control and monitoring system and provide valuable support for decision-making on the shop floor.

The work carried out:

1.2.2.1 Development of the Digital Twin and In-line Quality Control Concept

A general schematic of the overall concept that has been defined for the digital twin and in-line quality control of the hybrid robotic manufacturing cell is illustrated in Figure 1.2.2.1. The system is structured across two complementary layers: the physical layer and the cyber layer. The physical layer is composed of the robotic workstation and external sensor modules. The robotic workstation module includes the robot itself, the positioner, interchangeable tool heads (e.g., extruder and spindle), the build plate, and the PLC, among other components. The external sensor module consists of laser scanners, cameras, thermal imaging devices, and other measurement equipment. The cyber layer comprises the data management and storage layer, the digital twin module, and the intelligence module. The digital twin module replicates the robotic workstation and the manufactured part, enriched with anomaly severity scores. The intelligence module includes the key performance indicators (KPIs), an AI-based anomaly detection model, and the anomaly severity scoring model. As a part is being constructed by the hybrid robotic manufacturing cell, the data provided by the external sensors will be used for storing the process parameters and detecting the quality of the part that is under construction. This data will be implemented in the digital twin and intelligence modules so that the overall quality of the constructed parts will be known, and if any vital manufacturing defects are detected, the material wasted due to manufacturing defects will be minimized.

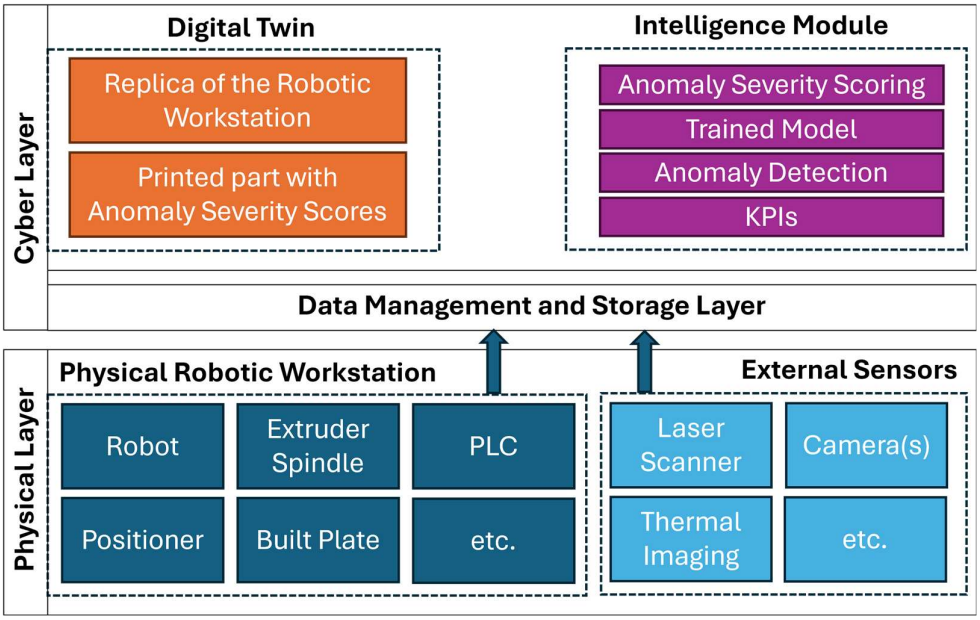

Figure 1.2.2.1 Overall system schematic

To realize this digital twin–enabled in-line quality control system, a dedicated pilot system is being established to facilitate data collection from a series of prints. The correlation between collected sensor data and manufacturing defects will then be analyzed. This process will enable the training and validation of a suitable AI model, which can later be deployed within the hybrid robotic cell.

The required data has been clearly defined and categorized according to source.

- **Internal sensors** (approx. 1 Hz):
  • X, Y, and Z coordinates, velocities and accelerations of the extruder tip
  • Extrusion/Print bed temperatures
  • Extrusion feed rate
  • Joint angles, velocities, and accelerations
- **External sensors** (approx. 1 Hz):
  • Height and width of the printed layer
  • Deviations in height and width
  • Visible defects (if any)
  • Temperature profiles

Using this data, a three-dimensional point cloud will be generated to represent the manufactured part. The AI model will evaluate the point cloud and predict potential defects. Each point will then be assigned a severity score based on a traffic-light coding system (red/yellow/green). This approach ensures that the resulting digital twin provides intuitive, easy-to-understand feedback, enabling end users to operate the system without requiring extensive training or a specialized background in robotics. Schematic of this process is given in Figure 1.2.2.2.

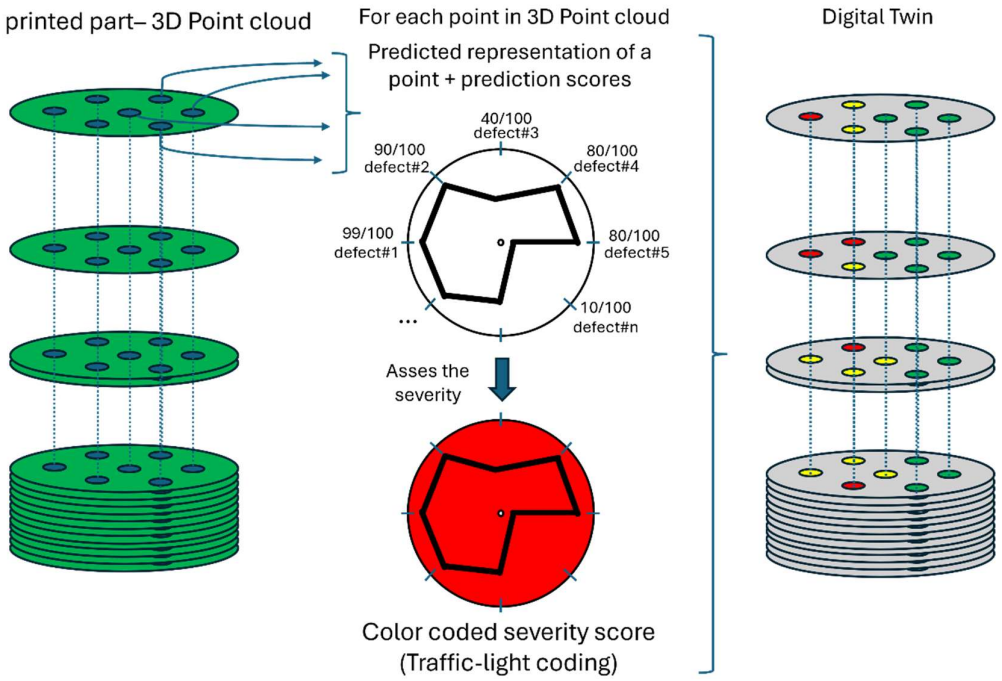

Figure 1.2.2.2 Digital twin and quality control schematic

1.2.2.2 Performed Studies

Within the first year, work has concentrated on laying the groundwork for digital twin development and defect detection in additive manufacturing. The primary emphasis was placed on quality control in fused deposition modelling (FDM) for thermoplastic polymers, as FDM represents a widely adopted technique for both thermoplastics and fiber-reinforced composites.

Several common FDM defects were investigated, including warping, spaghetti, layer shifting, cracking, curling, and stringing. These defects were approached using computer vision techniques, particularly by applying the You Only Look Once (YOLO) model for image-based recognition and classification. To further enhance detection accuracy, attention mechanisms were integrated into the baseline YOLO architecture. The modified models demonstrated improved performance in both defect classification and localization tasks.

This work resulted in a conference paper entitled *"A Comparative Study of Attention-Augmented YOLO Architectures for Defect Detection in Fused Deposition Modelling"*, presented at the 30th IEEE International Conference on Emerging Technologies and Factory Automation (ETFA2025). While the outcomes of this study are academic in nature, they serve as a critical step in developing in-house expertise and building the necessary know-how for later implementation within the TWIN-IT-ROMANS project. Moreover, the results provide an initial foundation for the advanced automated defect detection mechanisms that will eventually be integrated into the hybrid robotic cell. A more detailed information is provided in Appendix C.

1.2.2.3 Future Work

Building upon the progress achieved during the first year, the next phase will focus on moving from concept development and benchmarking towards implementation of the additive manufacturing within the hybrid robotic cell. The primary objective is to establish a functioning first iteration of a digital twin–enabled in-line quality control system that can directly support real manufacturing scenarios.

The immediate focus of the upcoming term is to move toward a proof-of-concept implementation of the digital twin and in-line quality control system. Although significant progress has been made in developing the underlying methods and defining the system architecture, a complete prototype has not yet been achieved. The forthcoming research visit to London South Bank University will be central to this effort, as it will concentrate on realizing the first iteration of the proof-of-concept. This stage will demonstrate how the digital twin framework can be applied to additive manufacturing within the hybrid robotic cell and is expected to conclude the initial cycle of concept validation.

A key priority will be the collection and structuring of sensor data from the dedicated pilot system. Internal data (motion parameters, joint states, extrusion and bed temperatures) and external data (layer geometry, defect visibility, thermal profiles) will be correlated with observed anomalies. This effort will enable the validation of defect detection models under realistic operating conditions and provide the foundation for linking severity scoring with adaptive process control.

In parallel with these developments, conceptual work will begin on extending the digital twin approach to the subtractive manufacturing side of the hybrid cell. At this stage, the work will remain exploratory, focusing on defining process parameters, identifying potential defect modes, and outlining data requirements. This approach mirrors the pathway taken for additive manufacturing during the first year and will provide the basis for future integration across both processes.

Together, these activities will serve to strengthen the existing results, establish the first proof-of-concept for additive manufacturing, and open a pathway toward a unified digital twin framework that encompasses both additive and subtractive manufacturing within the TWIN-IT-ROMANS project.

1.2.3 Investigation of Sustainability (T2.3) (M1-M36)

Objectives: The system to be developed is intended to include various manufacturing and quality control methods. For the product to be developed to be user-friendly, the system should have a simple, common user interface for all operations. Using various algorithms, learning by demonstration, autonomous task planning, and a common CAM program strategy will be used to generate the motion of the robotic manufacturing cell. For operators to make easy interventions, a special effort will be made to make the developed communication easy to understand. Furthermore, the developed manufacturing cell will be evaluated for its waste material generation, energy consumption, and personnel safety metrics to ensure the sustainability of the proposed concept (Led by UBAH).

The work carried out: In the Workshop on Sustainability, all partners presented their ongoing sustainability initiatives, exchanged best practices in responsible manufacturing, and identified key challenges in implementing sustainable solutions. Discussions focused on aligning project objectives with United Nations Sustainable Development Goals, covering both technical sustainability and social inclusion aspects.

The following sustainability goals for the TWIN-IT-ROMANS project were defined:

The project will aim to develop strategies to minimize material waste, improve energy efficiency, and enhance the overall resource efficiency of the hybrid robotic manufacturing.

The measurable sustainability targets will be defined with the help of key performance indicators below, aligned with SDG12:

- Raw material utilization rate: Percentage of raw material converted into the final product
- Scrap rate: Percentage of defective parts per batch
- Recycling rate: Percentage of materials reused or recycled in the system Manufacturing
- Cycle time: Time required to manufacture one unit

Aligned with SDGs 9 and 13, this project will aim to explore low-energy and environmentally friendly manufacturing processes for decarbonization efforts.

To assess progress, the following KPIs will be tracked:

- Energy consumption: The amount of energy consumed per part manufactured
- CO2 emissions per unit produced: Direct emissions associated with production
- Total greenhouse gas emissions (cradle to gate): a life cycle assessment metric to quantify the overall environmental footprint

Aligned with SDG 5 and 10, this project prioritizes diversity, inclusion, and equitable access to advanced engineering technologies.

- Outreach activities
- Ease of use
- Gender participation rate

1.2.4 Prototype development (T2.4) (M1-M36)

Objectives: The purpose of this task is to produce a system for testing and verifying the collaborative robot system that has been designed and researched. The system will be produced in two different countries. The designed parts of the system, including mechanical and electrical components, will be produced by subcontracting third-party manufacturing companies. The members of the consortium in which the manufacturing cells will be assembled are HKTM and MCI.

The work carried out: The modeling of the two-axis positioner with the collaborative robot has been carried out.

1.2.4.1. HKTM (IZTECH) Prototype

Following the system design and integration planning, the **prototype development phase** has been initiated. Procurement activities have already started, and a significant portion of the required components has been acquired. The progress of the main subsystems is as follows:

- **Positioner** – Mechanical design and dynamic analysis have been completed. Procurement of the reducer and motor has been finalized, and the system is being prepared for transition into manufacturing.
- **Interchangeable Tool Heads** – The Schunk SWA/K 40 system has been selected, and procurement has been completed. Integration studies for power, data, and pneumatic connections are ongoing.
- **Vacuum System** – The 0.85 kW vacuum pump, filter, and relief valve have been acquired. The design is finalized and ready for installation.
- **Spindle Unit** – The Hertz HS315 spindle with BT30 tooling has been selected and purchased. Integration with the reducer and robot payload analysis has been performed.
- **3D Printing Head** – Revision 1 of the printing head has been completed. The head supports fiber composite and plastic printing and includes additional force measurement mechanisms. Prototyping is in progress.
- **Adaptive Fixture** – Literature review has been completed. A simple test system based on granular jamming is being developed in collaboration with POLITO.
- **Gripper System** – The Schunk pneumatic universal gripper has been selected. Procurement is ongoing, and integration with the robot system is planned.
- **System Integration and Control** – The Beckhoff control architecture has been defined, and procurement of core modules has been completed. Siemens PLC interoperability has been designed, and HMI/camera modules are being integrated.

At this stage, the focus is on assembling the procured components, validating their compatibility, and conducting preliminary tests to ensure that each unit meets the specified requirements. The production of custom-designed parts, such as adaptive fixtures and tool head housings, has also begun, ensuring that both standard equipment and bespoke solutions are integrated into a coherent prototype.

In parallel, the control and communication architecture based on the Beckhoff platform is being configured, while auxiliary modules such as the camera system, HMI, and safety enclosures are progressing toward final installation. Once all elements are combined, the prototype will serve as a fully functional demonstrator, allowing the transition from conceptual design to real-world validation of the TWIN-IT-ROMANS system.

1.2.4.2. MCI Prototype

A robotic cell prototype has also been developed at MCI in Austria. Unlike fully automated systems, this prototype currently performs tool changes manually. The cell has been designed with hybrid manufacturing capabilities, as it is able to combine additive and subtractive processes within a single setup. Specifically, the integrated 3D printing head allows for the deposition of thermoplastic polymer-based materials, which are subsequently processed through machining operations to achieve the required geometrical accuracy and surface quality.

This hybrid approach not only demonstrates the feasibility of combining different manufacturing methods in a single robotic platform but also provides valuable insights into workflow integration, operator interaction, and potential pathways toward future automation of tool-changing mechanisms.

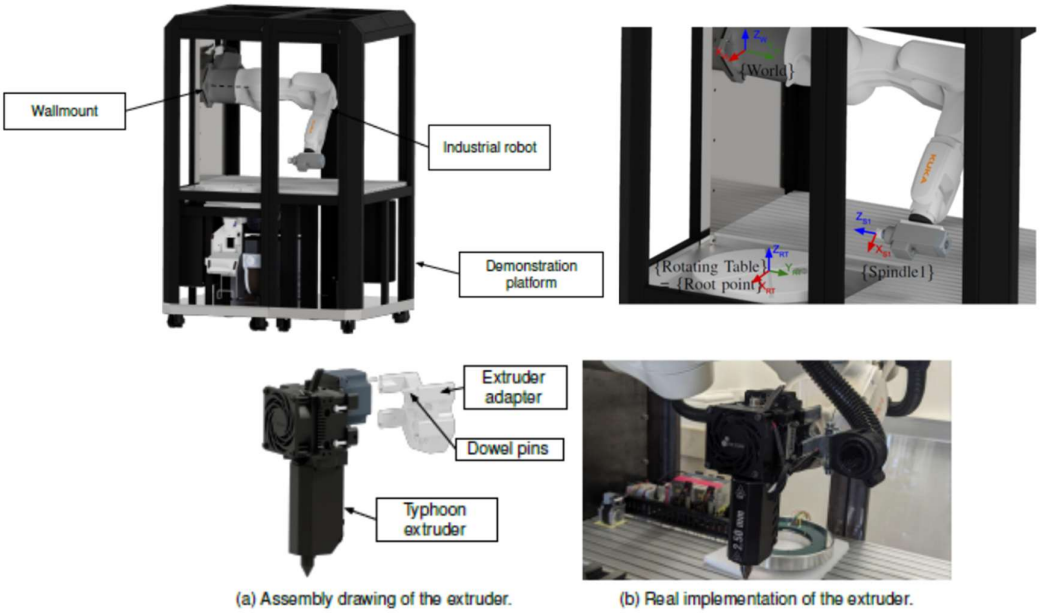

Figure 1.2.4.2.1. Robotic cell prototype developed at MCI

1.2.5 System Integration and Demonstration (T2.5) (M1-M36)

Objectives: The objective of this task is to (1) integrate the components developed in this project into the prototypes, (2) optimization of hybrid manufacturing process aligned with the sustainability goals mentioned in T2.3, and (3) to demonstrate the prototypes in environment of laboratory and in the test field of end user (TRL 6).

The work carried out: The modeling of the two-axis positioner with the collaborative robot has been carried out.

The integration and control of the robotic cell are based on a Beckhoff system architecture, which serves as the central backbone for coordinating all subsystems. Within this configuration, both data flow and power distribution are managed to ensure reliable communication and synchronized operation across the various modules. The diagram illustrates how every subsystem, from motion control to process monitoring, is interconnected through Beckhoff's modular I/O platform.

All previously described units—such as the interchangeable tool heads, positioner, 3D printing head, subtractive spindle, vacuum system, grippers, and adaptive fixtures—are directly interfaced with the Beckhoff controller. This centralized approach simplifies the integration of diverse processes (additive, subtractive, and handling) within a single robotic cell, while providing high flexibility for future expansions.

In addition to the core process equipment, auxiliary modules such as a camera system and a human–machine interface (HMI) are included. The camera enables visual monitoring and quality inspection of operations, while the HMI provides operators with intuitive access for control, diagnostics, and system adjustments.

The Beckhoff PC-based controller is also designed to communicate with a Siemens PLC, establishing interoperability between platforms. This dual-controller configuration enables the use of Siemens Tecnomatix software for virtual commissioning and digital twin simulations. By combining Beckhoff's real-time hardware control with Siemens' advanced simulation environment, the system ensures both accurate real-world performance and comprehensive virtual validation.

Overall, this integration strategy provides a robust, modular, and scalable control framework, capable of managing the complexity of hybrid manufacturing processes while supporting advanced monitoring, optimization, and operator interaction.

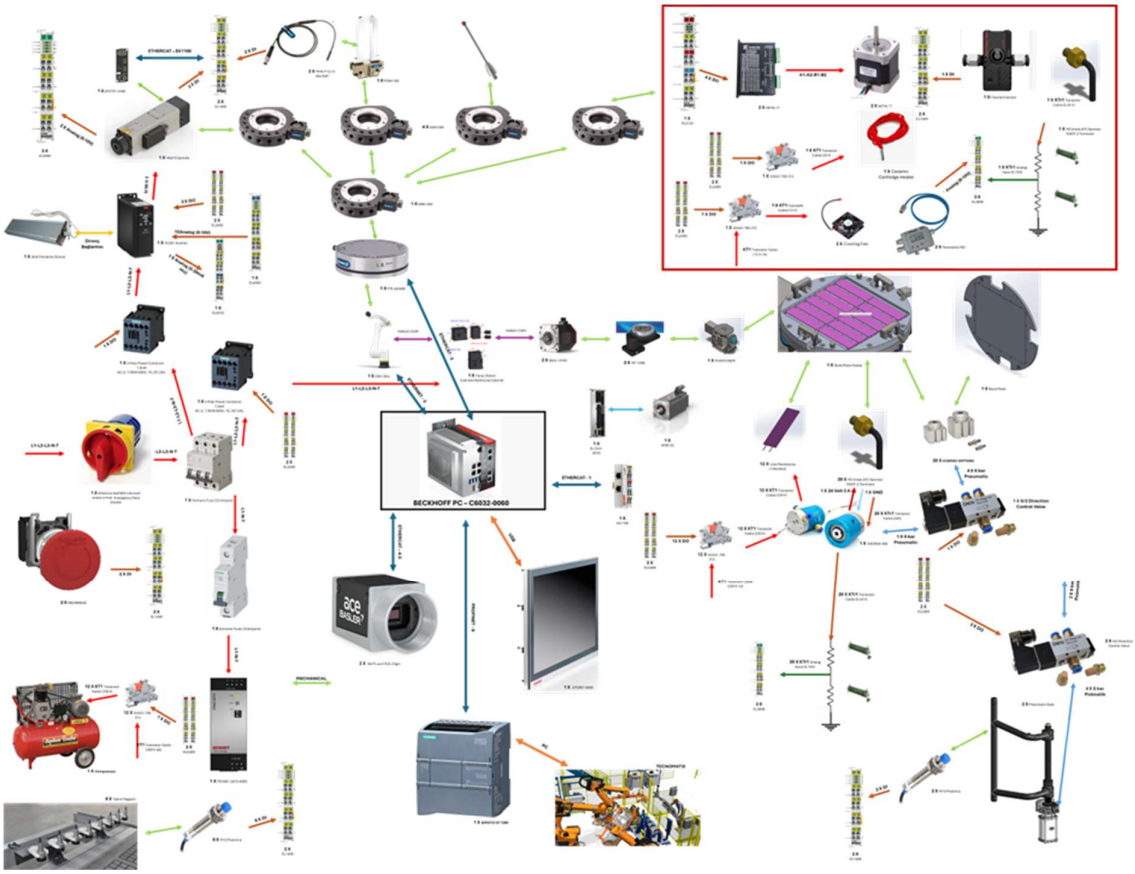

Figure 1.2.5.1. System Flow Diagram of the TWIN-IT-ROMANS Project

2. DISSEMINATION OF THE TECHNICAL OUTPUTS

2.1 Dissemination Objectives Related to Technical Aspects of the Project

The key performance indicators related to the technical aspects of the TWIN-IT-ROMAN project are presented in Table 1 and highlighted in yellow color.

Table 2.1. Improve S&T Capacity

Objective	Key Performance Indicators (KPIs)	Target Values
O1: Improve S&T Capacity	Research prototypes	2
	Joint journal & conference publications	6 & 6
	Patent applications	2
	Expert visits	8

The dissemination measures, the target audience, the expected impact, and the target values as appeared in "Table 2.2a: Dissemination strategy to share the project outputs so that others can make use of it" of the grant agreement are shown in Table 2. The dissemination objectives directly related to the technical outputs are highlighted in yellow.

Table 2.2. Dissemination

Dissemination												
Measure	**Target audience**							**Expected Impact**	**Target Value (KPIs per year)**			
	A	**B**	**C**	**D**	**E**	**F**	**G**		**1**	**2**	**3**	**Total**
Publications	X		X				X	Bringing TWIN-IT-ROMANS's concept and scientific results formally out to the community	1	2	3	6
Workshops	X	X	X	X	X			Audience questions about TWIN-IT-ROMANS's concept and scientific results can be answered	2	2	1	5
Conferences	X	X	X	X	X		X	Sharing TWIN-IT-ROMANS know-how with participants from different sectors	3	3	0	6
Academic dissertations	X						X	Presenting TWIN-IT-ROMANS's scientific results in academic literature	0	0	4	4
Outreach activities	X		X	X	X	X		Reaching general public through open-door activities	2	2	1	5
Open-source data	X		X	X	X	X	X	Open source to speed up technology take up	1	1	1	3
Short term trainings	X		X	X	X		X	Rapid and personal transfer to knowledge from experts via on-site or virtual trainings	6	8	6	20
Summer School	X		X	X			X	Sharing TWIN-IT-ROMANS know-how with researchers of TWIN-IT-ROMANS and researchers to contribute the target area	1	0	0	1

2.2 Explanation of the work carried out for dissemination objectives related to the technical aspects

2.2.1 Research prototypes

Two research prototypes are currently under development within the project: one at IZTECH and one at MCI. Both prototypes address key aspects of hybrid robotic manufacturing and sustainability. They are at the design and early testing stages. Progress is being tracked through internal reviews and will be documented with images and technical descriptions once the prototypes reach demonstration readiness.

2.2.2 Publications

Publications so far include three conference papers presented in IFToMM for Sustainable Development Goals (I4SDG 2025) and 30th IEEE International Conference on Emerging Technologies and Factory Automation.

- Türkcan, M.Y., Kurt, B., Karaş, B., Tetik, H., Shokrani, A., Dede, M.İ.C. (2025). Towards Sustainable Manufacturing: A Review and Future Directions in Additive Manufacturing of Fiber-Reinforced Polymer Composites. In: Carbone, G., Quaglia, G. (eds) Proceedings of I4SDG Workshop 2025 - IFToMM for Sustainable Development Goals. I4SDG 2025. Mechanisms and Machine Science, vol 179. Springer, Cham. https://doi.org/10.1007/978-3-031-91151-4_62
- Gündüz, G.M., Dede, M.İ.C., Kiper, G., Schmitz, M., Corves, B. (2025). Redundancy Resolution Options for the Twin-it-Romans Robotic Hybrid Manufacturing System. In: Carbone, G., Quaglia, G. (eds) Proceedings of I4SDG Workshop 2025 - IFToMM for Sustainable Development Goals. I4SDG 2025. Mechanisms and Machine Science, vol 179. Springer, Cham. https://doi.org/10.1007/978-3-031-91151-4_61
- Hasan Cezayirli, Halil Tetik, Mehmet İsmet Can Dede, Wai Lwin Phone, Bugra Alkan, (2025). A Comparative Study of Attention-Augmented YOLO Architectures for Defect Detection in Fused Deposition Modelling, 30th IEEE International Conference on Emerging Technologies and Factory Automation

2.2.3 Patent applications

At this stage of the project no patent applications have been filed. The consortium has been focusing on research, technology development and validation activities; therefore, potentially patentable results are still under evaluation. An internal procedure for identifying and protecting intellectual property has been established, including periodic innovation reviews and consultation with the partners' Technology Transfer Offices such as Atmosfer TTO in IZTECH. Any patentable findings emerging from the next phases of the project will be documented and, where appropriate, applications will be submitted under the consortium's agreed IPR management plan.

2.2.4 Academic Dissertations

Within the project, four academic dissertations (PhD level) are currently under development by consortium partners and affiliated students. These theses are aligned with the project's research topics. Each dissertation is being supervised jointly by partner institutions and is expected to

produce publishable results and potential intellectual property. Progress is monitored through periodic reviews, and final submissions are planned within the project timeframe. The ongoing studies are:

- “Autonomous Optimal Motion Planning and Task Scheduling of a Collaborative Robot” by Gizem Merve Gündüz supervised by Prof. Gökhan Kiper (IzTech) and Prof. Burkhard Corves (RWTH Aachen).
- “In-line Quality Control of a Robotic Manufacturing Cell” by Hasan Cezayirli supervised by Dr. Halil Tetik (IZTECH) and Dr. Buğra Alkan (LSBU)

References

[1] Shintake, J., Cacucciolo, V., Floreano, D., & Shea, H. (2018). Soft Robotic Grippers. *Advanced Materials, 30*(29), 1707035. https://doi.org/10.1002/adma.201707035

[2] Köklü, U., Avci, A., & Etyemez, A. (2015, November). *Fonksiyonel derecelendirilmiş kompozit malzemelerin talaşlı işlenebilme performansı*. Conference paper. Retrieved from https://www.researchgate.net/publication/298719461

[3] Boy, M. (2022). PEEK-CF30 termoplastik malzemenin delinmesinde delme parametrelerinin etkileri: İtme kuvveti, yüzey pürüzlülüğü ve delaminasyon. *Yüzüncü Yıl Üniversitesi Fen Bilimleri Enstitüsü Dergisi, 27*(3), 570–580. https://doi.org/10.53433/yyufbed.1104700

APPENDIX

Appendix A

A.1. Positioner Design

In the positioner design, several critical factors must be carefully considered to ensure both functional performance and seamless integration with the robotic cell. One of the foremost aspects is the dimensioning of the worktable. The table must be designed with sufficient surface area to accommodate the range of workpieces, including composite and plastic parts of varying geometries, while maintaining rigidity under operational loads. A well-dimensioned table not only provides stability during machining but also enhances the accuracy and repeatability of the entire process.

As part of the initial production planning, the first end product to be manufactured within the scope of the project has been defined as the “Naka profile” component, which was proposed by HKTM. This part has approximate dimensions of 50 × 50 × 150 mm, making it a representative benchmark for both design validation and process capability assessment. Since it reflects a realistic use-case in terms of geometry and material, the airfoil profile has been strategically selected as the pilot component to evaluate the performance of the robotic cell under near-industrial conditions.

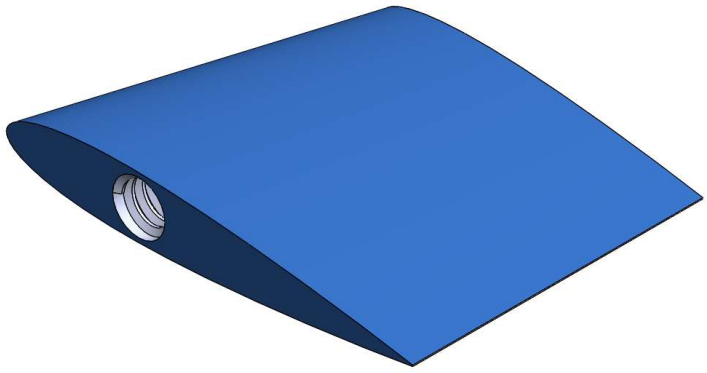

Figure A1. Airfoil Profile from HKTM

To accommodate the manufacturing of this component, particular attention was given to the worktable design. While the dimensions of the airfoil profile itself are relatively moderate, it was recognized that future operations would likely involve parts of different geometries and sizes. Therefore, the table was designed not only to meet the immediate requirements of this specific component but also to provide scalability and flexibility for subsequent use cases. In this context, the general industry-standard 3D printer table size of 300 × 300 mm was adopted as the design reference. This choice provides sufficient space for the airfoil profile while also ensuring compatibility with larger workpieces that may be introduced in later project phases.

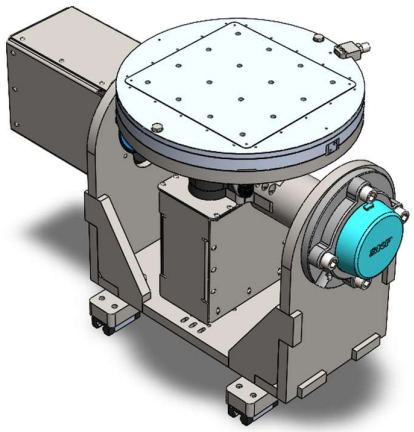

Figure A2. Positioner Design-1

The development of such a table required careful consideration of structural rigidity, thermal stability, and load distribution. The enlarged table surface enables multiple orientations of the part, which is particularly important for adaptive fixturing and for ensuring accessibility of the cobot and machining tools. At the same time, the increased table area necessitated enhancements in the support structure to minimize deflection and vibration during machining. By combining these design improvements with a temperature-controlled surface, the table was optimized for both composite processing and plastic additive manufacturing, thus extending its functionality beyond the immediate needs of the pilot part.

Through these measures, the positioner and its table have been tailored not only to the specific requirements of the airfoil profile but also to establish a versatile platform capable of addressing a wide range of parts and applications in the future. This ensures that the initial investment in development contributes directly to the scalability and long-term sustainability of the robotic cell concept.

A.1.1. Heated Worktable Design

Another important design element is the incorporation of a heated worktable. Since continuous fiber composites and certain thermoplastic materials are highly sensitive to processing temperature, the integration of a heating mechanism is essential. A temperature-controlled table not only allows for improved bonding between material layers but also helps reduce residual stresses, enhances the overall surface finish, and minimizes warping during both additive and subtractive operations. These aspects are critical for ensuring the dimensional accuracy and long-term durability of the manufactured components.

To achieve this functionality, the table design was optimized through the integration of heater resistors. The resistors were strategically positioned beneath the table surface to promote a uniform heat distribution across the entire working area. Such homogeneity is particularly important when processing larger components, as local hot or cold spots can result in uneven curing of composites or distortion of thermoplastic materials. By adopting a carefully arranged

resistor layout, the risk of temperature gradients within the work zone was significantly minimized.

In addition to the physical design, Finite Element Analysis (FEA) was employed to simulate the thermal behavior of the heated table. The analysis provided insights into temperature propagation, heat transfer rates, and potential concentration points of thermal stress. Based on these results, adjustments were made to the resistor placement, insulation layers, and table material selection to ensure efficient heating and long-term thermal stability. This predictive design approach not only validated the feasibility of the heating system but also enabled the identification of the most energy-efficient configuration, balancing power consumption with processing requirements.

Through this combined approach of mechanical design, thermal integration, and numerical simulation, the heated worktable was developed into a robust subsystem capable of supporting both continuous fiber composite processing and thermoplastic manufacturing under controlled and repeatable conditions.

A.1.2. Resistor Design

For the intermediate connection, a Usit ring is employed, featuring 36 cable connections and 2 pneumatic connections. Considering the integration of components such as resistors and sensors, the system allows for the use of up to 12 resistors at maximum capacity.

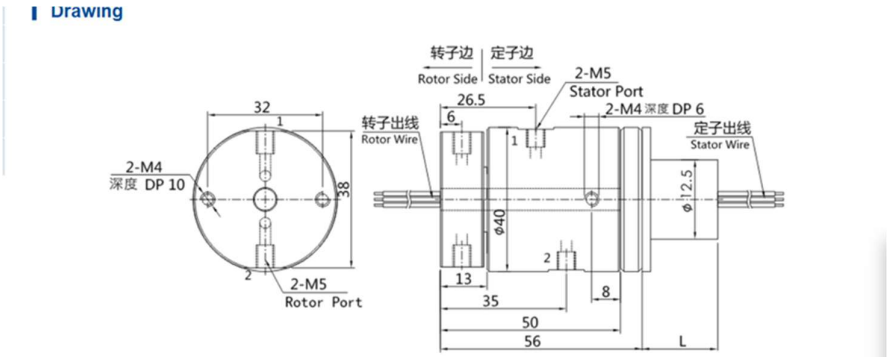

Standard model list

Model	Passages(Gas)	Port Size	Pipe Size	Signal Circuits(2A)	Length L(mm)
3002004-06S	2 passages	M5	4~6mm	6	14
3002004-12S	2 passages	M5	4~6mm	12	21
3002004-24S	2 passages	M5	4~6mm	24	35
3002004-36S	2 passages	M5	4~6mm	36	52

Figure A3. Usit Ring in the positioner

Considering the table dimensions, the number of resistors, and the fact that each resistor can carry a maximum of 2 A per cable, together with the specification that a single resistor generates approximately 3 W per cm², the resistor dimensions can be determined accordingly.

Table A1. Resistor Calculation

#	Name	Value	Unit
1	a	135	mm
2	b	35	mm
3	P	3	W
4	Area	47,25	cm^2
5	Power	141,75	W
6	Voltage	220	V
7	Eff	0,85	
8	Current	0,758021	A
9	Number of Resistor	12	
10	Total Power	1701	W
11	Total Current	9,096257	A

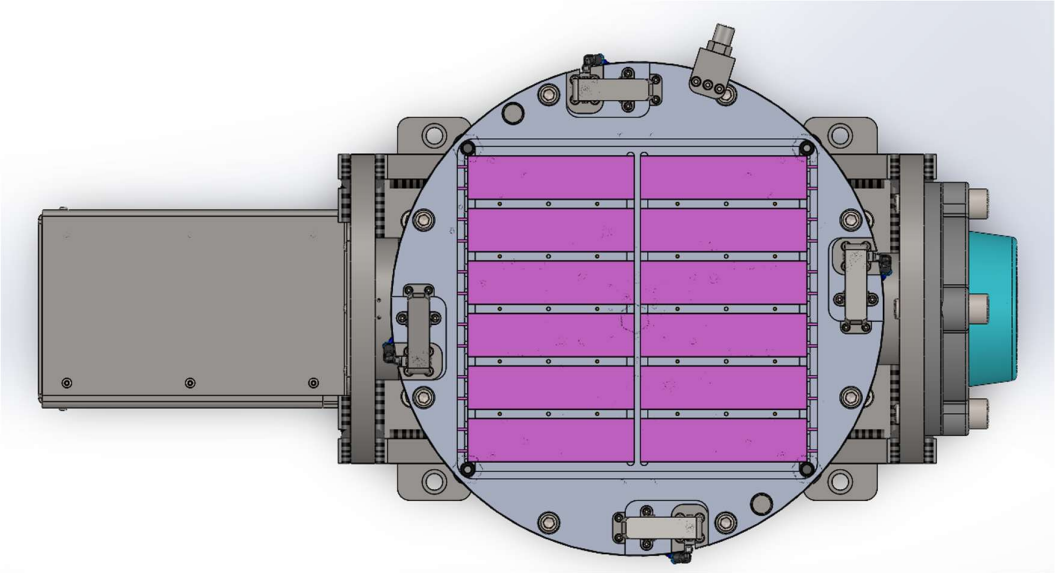

Figure A4. Placement of resistors on the worktable

A.2. FEA for Workable

Through Finite Element Analysis (FEA), the heat distribution achieved by the resistors was examined in detail, and the most optimal resistor configuration and connection layout was identified.

A.2.1. Mesh Quality

A.2.1.1. Skewness

In the FEA analysis, the skewness value was monitored as an indicator of element quality. This parameter was checked to ensure that it remained within the acceptable range, since maintaining proper skewness values is essential for accurate and reliable simulation results. According to common meshing guidelines:

→ 0 – 0.25 → Excellent element quality

→ 0.25 – 0.50 → Good quality (acceptable for most analyses)

→ 0.50 – 0.90 → Marginal, should be improved if possible

→ > 0.90 → Poor quality, results may be unreliable

Mesh Metric	Skewness
Min	4,5119e-004
Max	0,90644
Average	0,25246
Standard Deviation	0,14058

Figure A5. Skewness Values

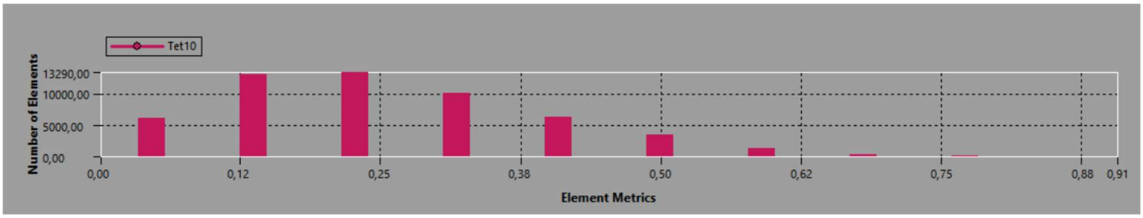

Figure A6. Skewness value distribution based on mesh

A.2.1.2. Aspect Ratio

In the FEA analysis, the aspect ratio of the elements was also evaluated as a key quality metric. This parameter was monitored to ensure that the mesh remained within acceptable limits, since excessively high aspect ratios can lead to numerical inaccuracies and convergence issues. According to common meshing guidelines:

→ 1 – 3 → Excellent element quality

→ 3 – 5 → Good quality (acceptable for most analyses)

→ 5 – 10 → Marginal, should be improved if possible

→ > 10 → Poor quality, results may be unreliable

Mesh Metric	Aspect Ratio
Min	1,1676
Max	6,5938
Average	1,8935
Standard Deviation	0,47633

Figure A7. Aspect Ratio Values

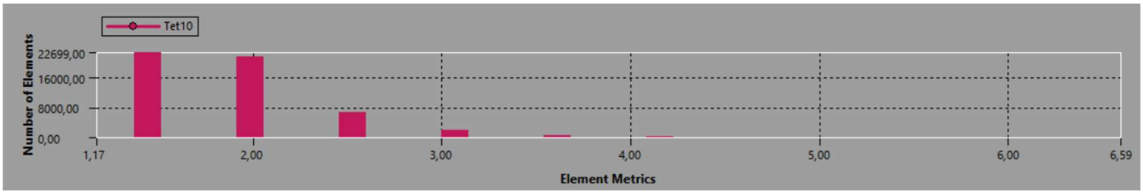

Figure A8. Aspect Ratio value distribution based on mesh

As a result, since the average values of both criteria (skewness and aspect ratio) remained within the "excellent" range, the mesh quality can be considered high and reliable.

A.2.1.3. Specification of Boundary Conditions

Since a transient-state heat transfer analysis was performed, the heat flux generated by the resistors was applied as a boundary condition. This approach allows the simulation to capture the time-dependent temperature distribution and evaluate how the applied heating power propagates through the worktable.

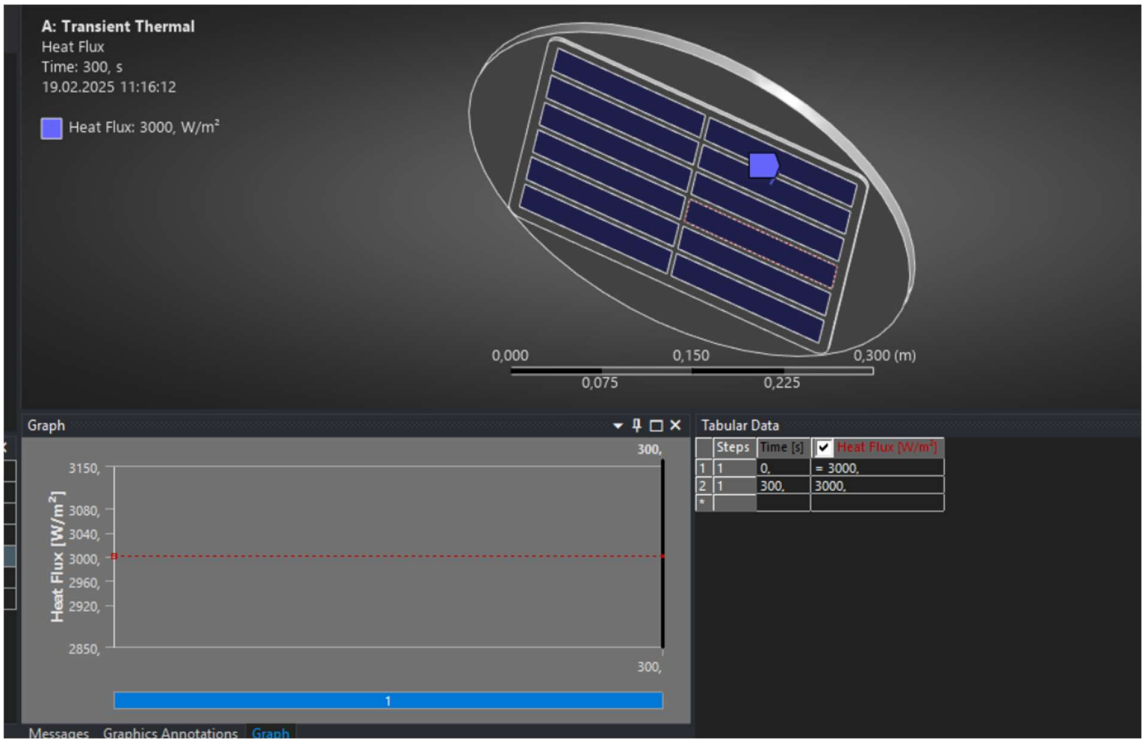

Figure A9. Specification of Boundary Conditions

A.2.2. Results of FEA

In this analysis, the time required to reach 40 °C, 60 °C, and 220 °C was evaluated under uncontrolled heating conditions, while the corresponding temperature distribution across the worktable was also examined. The primary objective was to assess whether significant thermal gradients would occur during the heating process. If the results demonstrate that the temperature distribution remains relatively uniform, with no substantial differences across the surface, the design can be considered successful and effective.

A.2.2.1. Results of FEA at 40°

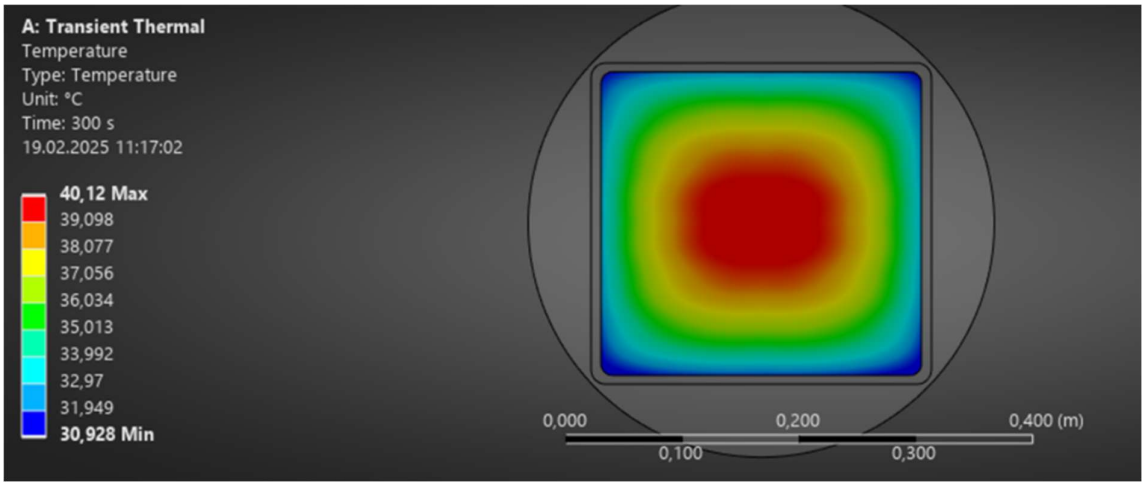

Figure A10. Results of FEA at 40° - 1

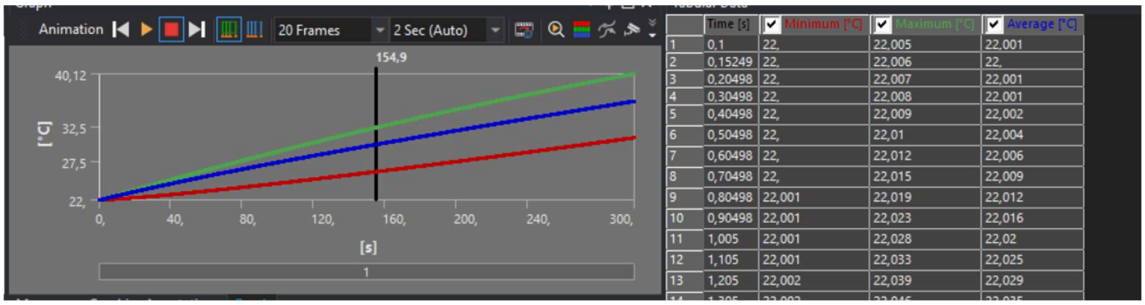

Figure A11. Results of FEA at 40° - 1

The system reaches a temperature of 40 °C within 150 seconds, demonstrating a rapid thermal response under the applied heating conditions.

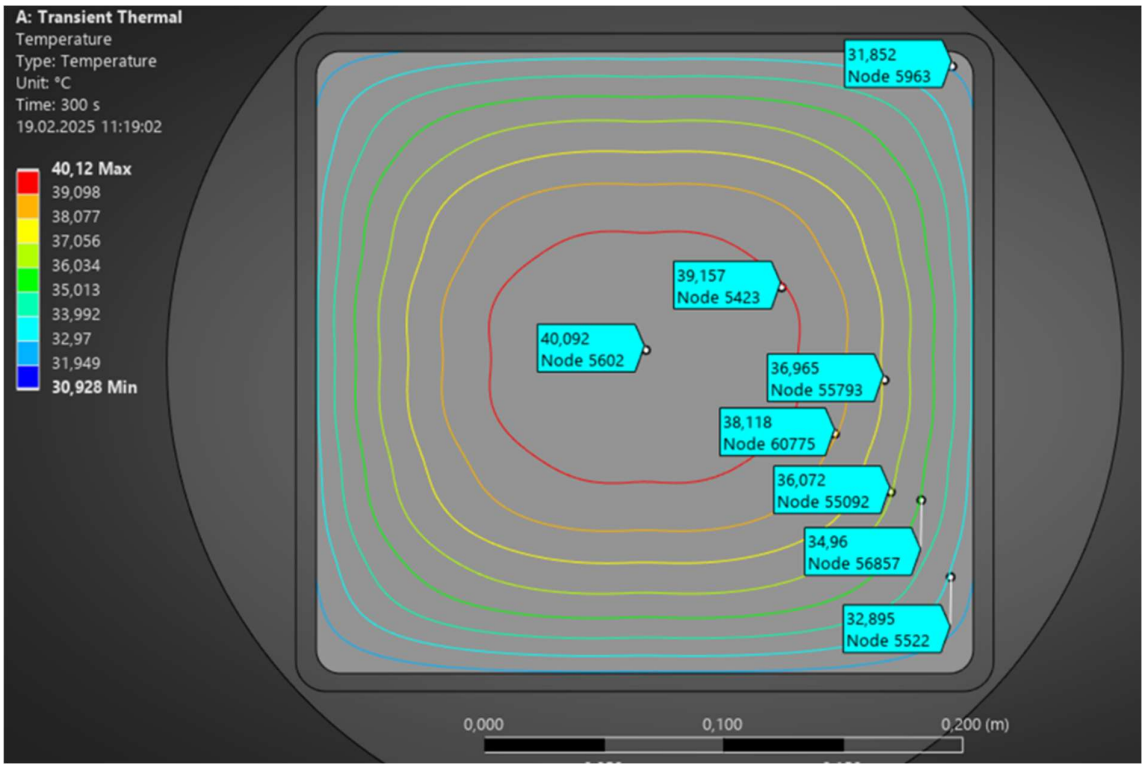

Figure A12. Results of FEA at 40° - 3

A.2.2.2. Results of FEA at 60°

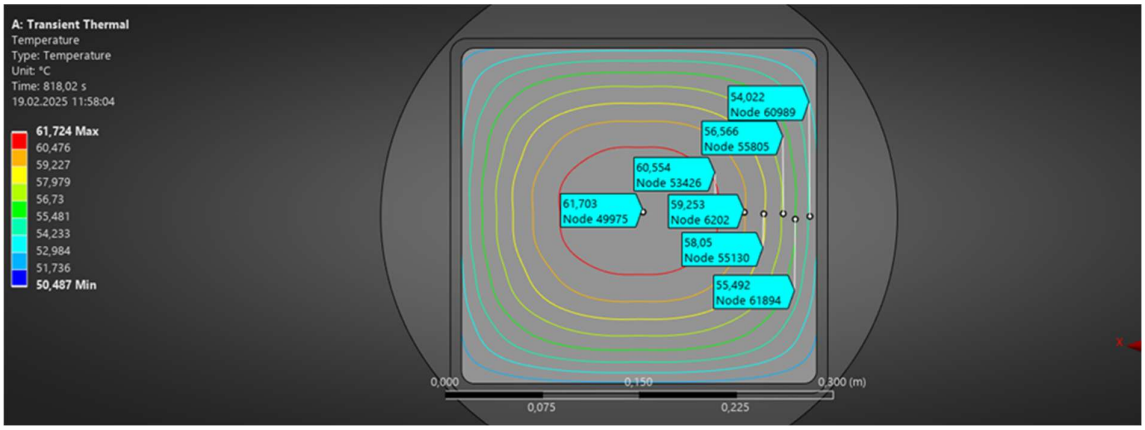

Figure A13. Results of FEA at 60° - 1

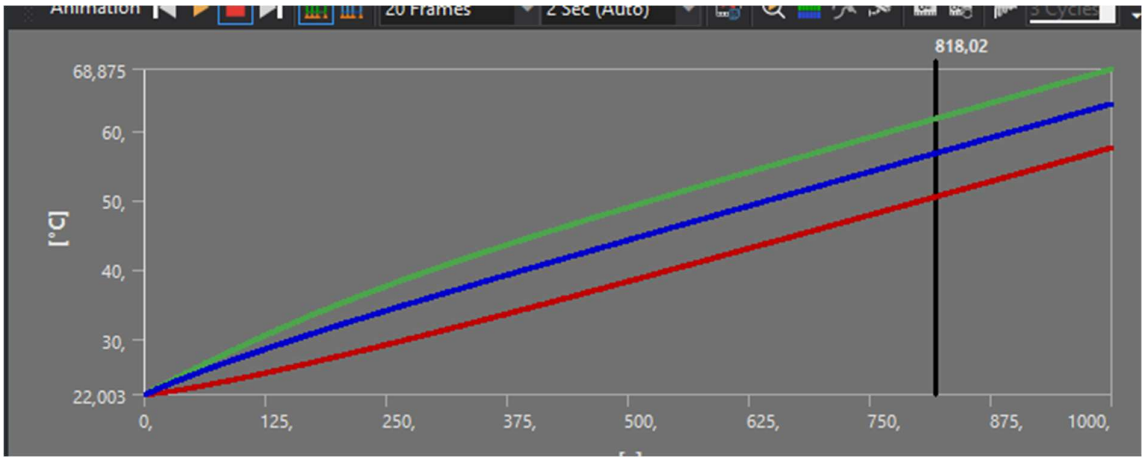

Figure A14. Results of FEA at 60° - 2

The system reaches a temperature of 40 °C within 800 seconds, demonstrating a rapid thermal response under the applied heating conditions.

A.2.2.3. Results of FEA at 220°

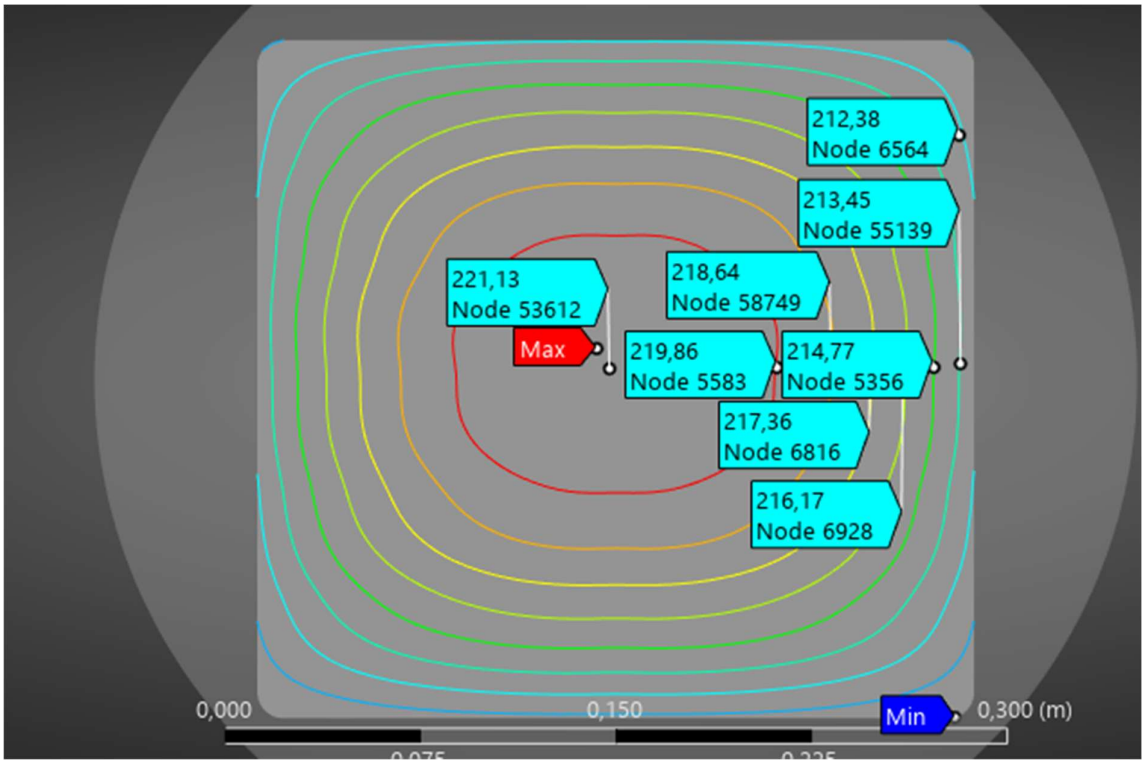

Figure A15. Results of FEA at 220° - 1

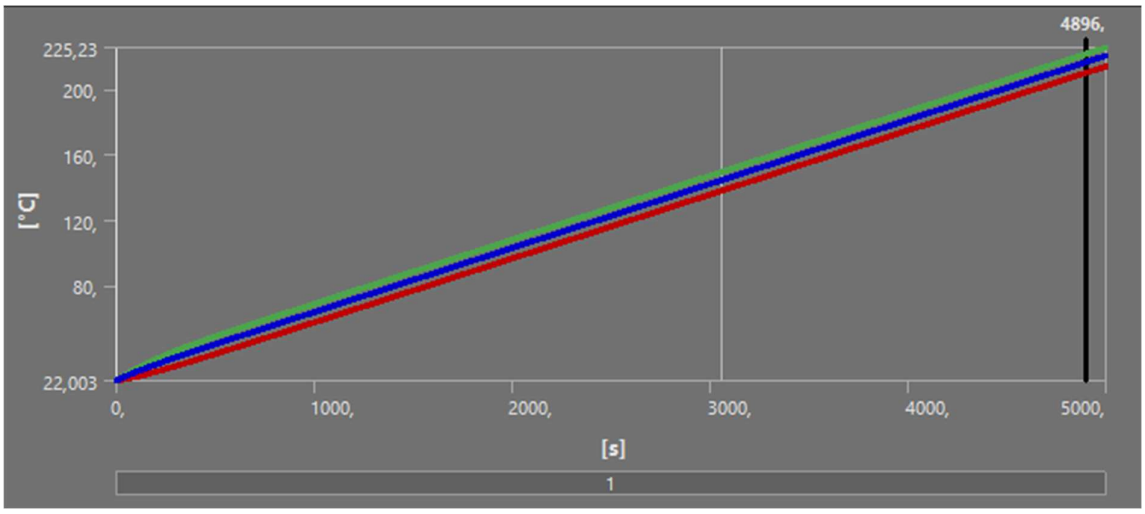

Figure A16. Results of FEA at 220° - 2

The system reaches a temperature of 220 °C within 3000 seconds, demonstrating a rapid thermal response under the applied heating conditions.

As a result, even under uncontrolled conditions, the heat distribution was found to be sufficient, and following the analyses, the resistor layout was validated and accepted as final.

A.3. Gearbox Selection

The selection of the reduction system represents an equally significant step. The reduction ratio must be chosen to balance speed and torque, ensuring that the positioner can provide both fine precision at low speeds and sufficient force to withstand machining forces. Incorrect reduction sizing could result in either excessive backlash or insufficient dynamic response, both of which would compromise process reliability.

For this design, the motor selected from Fanuc was a 4 Nm αi series motor. The reasoning behind this choice lies in the limitation of the additional cabinet connected to the cobot, which can support a maximum of two 4 Nm motors, corresponding to a total power of approximately 850 W. Within these constraints, the reduction system must be carefully matched to the motor in order to achieve the desired performance without exceeding the available capacity.

Figure A16. Fanuc αi series motor

After evaluating multiple alternatives, the GT-135B reducer with a 1/10 reduction ratio was identified as the most suitable candidate. This configuration offers an optimal balance between torque amplification and dynamic responsiveness, while also ensuring mechanical compatibility with the selected Fanuc motor. In addition, the reducer provides low backlash and high repeatability, both of which are critical for maintaining positioning accuracy and ensuring consistent machining quality. Thus, the chosen motor–reducer combination delivers not only efficiency and reliability but also the precision required for the positioner design.

Table A1. Gearbox Mechanical Properties

Characteristic / Özellikler	Unit / Birim	GT-135B
Output Table Supporting Bearing	–	Ball Bearing / Bilyalı Rulman
Rated Output Torque	N·m	43
Max. Output Torque	N·m	2 × Rated Output Torque
Inertia Moment	kg·m²	2.918×10^{-6}
Output Permissible Speed	rpm	300
Torsional Backlash	arcmin	≤ 1
Lost Motion	arcmin	2 (0.033°)
Repetitive Positioning Accuracy	arcsec	±10 (0.0028°)
Permissible Thrust Load	N	1,45
Permissible Moment Load	N·m	30
Runout of Output Table Surface	mm	0.015
Runout of Output Table Inner / Outer Diameter	mm	0.015
Parallelism of Output Table	mm	0.025
Protection Class	–	IP 65
Weight	kg	3,83

Figure A17. GT-135B Gearbox

The maximum output torque of the gearbox is 40 N·m, and the motor–gearbox combination can likewise deliver up to 40 N·m at the output. Consequently, the commanded/actuating torque must remain below this limit when the system dynamics (transients, impact loads, and uncertainty) are taken into account. Exceeding this threshold would risk saturation and potential mechanical overstress.

The subsequent section presents the overall mechanical and dynamic analysis, in which the applied loads, peak/transient torques, and safety factors are evaluated to verify compliance with the 40 N·m constraint.

A.4. Mechanical Design of Positioner

The mechanical design of the positioner was developed with a focus on structural rigidity, precision, and modular integration. The base frame was constructed to provide maximum stability while minimizing vibrations transmitted to the worktable. Special attention was given to the mounting interfaces, ensuring accurate alignment between the gearbox, motor, and rotary table. This guarantees both mechanical reliability and ease of assembly during production.

The rotary table was designed with sufficient surface area and a bolted pattern to accommodate different fixture configurations. Its geometry allows the processing of both composite and plastic parts, while also leaving space for potential heating elements and sensors. The table's parallelism and runout values were carefully evaluated against industrial tolerances to ensure repeatability in machining and additive operations.

A GT-135B reducer (1/10 ratio) was integrated to match the torque-speed requirements of the Fanuc 4 Nm IA motor. This combination provides up to 40 N·m of output torque with minimal backlash (≤ 1 arcmin) and high repetitive positioning accuracy (±10 arcsec). Such performance characteristics are essential to maintain consistent positioning under machining forces and to synchronize with the collaborative robot during dual-axis operations.

The design also incorporated cable routing and pneumatic channels, enabled by the usit ring, to ensure a clean and reliable interface for resistors, sensors, and auxiliary systems. Furthermore, weight distribution and structural stiffness were analyzed to reduce deflection under load, while maintaining a compact form factor suitable for robotic cell integration.

Overall, the mechanical design of the positioner combines robustness, accuracy, and flexibility, establishing a reliable foundation for subsequent dynamic and thermal analyses.

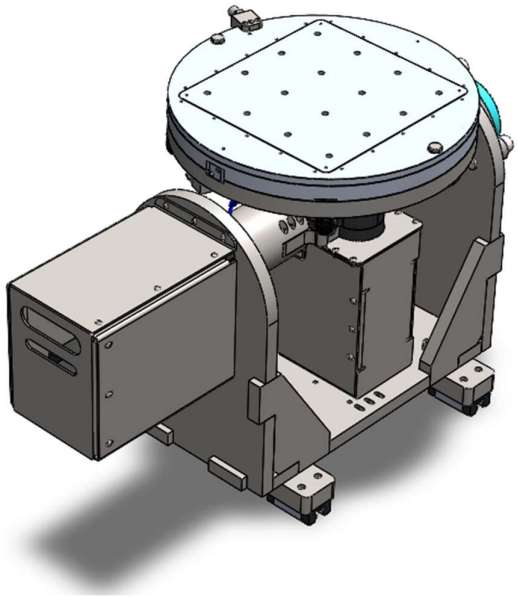

Figure A18. Positioner Design-2

A.5. Dynamic Analysis of Positioner

The dynamic analysis of the positioner was carried out to assess its performance under time-dependent operating conditions. In particular, the study focused on the effect of inertia and torque demand during acceleration and deceleration phases.

The combined inertia of the rotary table and workpiece was calculated, and the corresponding torque requirements were evaluated. The results confirmed that the actuating torque must remain below the 40 N·m limit defined by the motor–reducer configuration to ensure safe and reliable operation.

Furthermore, transient simulations were performed to observe the torque variation over time. These analyses demonstrated that the system is capable of maintaining stable performance without exceeding the allowable torque capacity.

Finally, the analytical results were verified using MATLAB/Simulink, which provided time-domain validation of the dynamic model and confirmed the suitability of the selected drivetrain configuration.

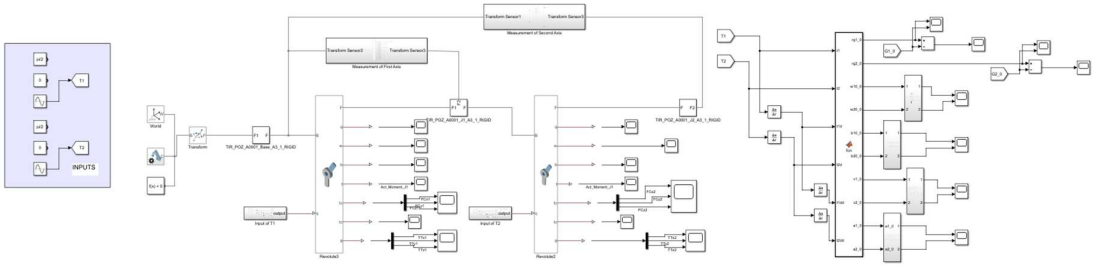

Figure A19. SIMULINK Diagram of Positioner

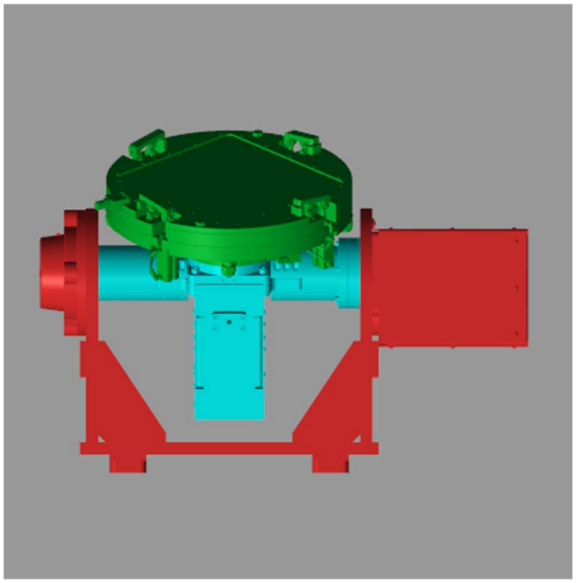

Figure A20. Positioner Simulation in SIMULINK

In the following simulations, a sinusoidal input signal was applied to the positioner model without the use of a counter-mass system. This scenario represents a more challenging case, since the absence of a counter-mass increases the effective inertia that must be handled by the motor–reducer assembly. Despite these conditions, the analysis results show that the actuating torque consistently remains below 40 N·m, which is the maximum allowable torque for the drivetrain.

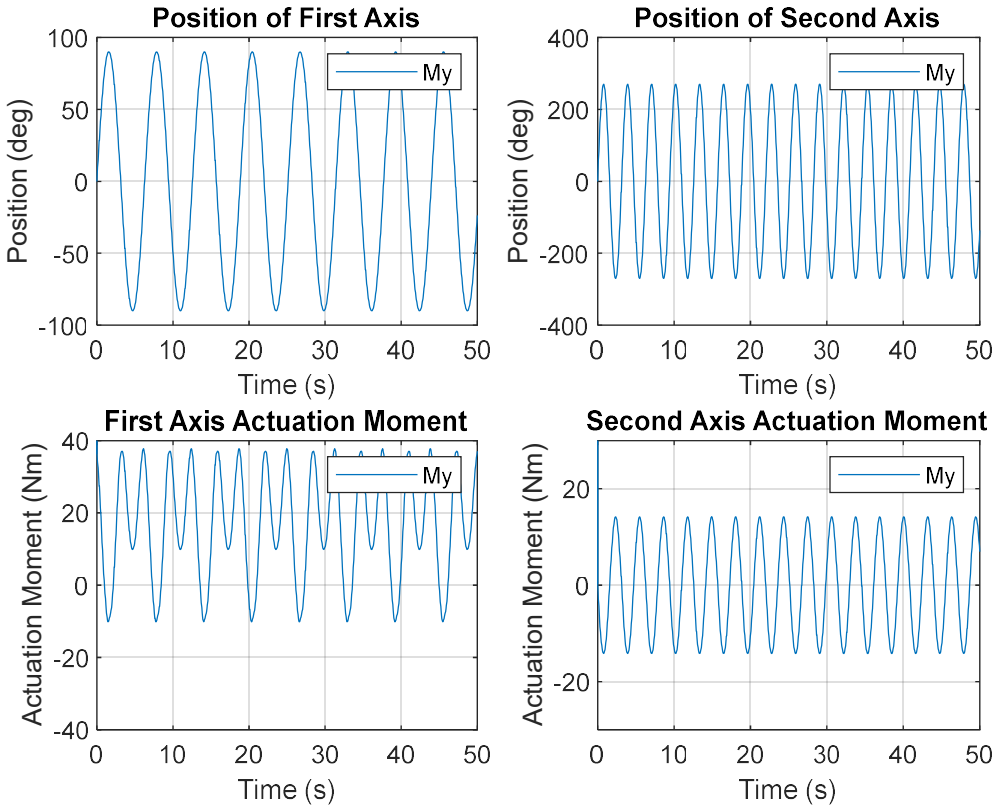

Figure A21. Actuating Moment Response Without Countermass

This outcome demonstrates that the selected motor–reducer configuration provides sufficient torque capacity even under unfavorable loading conditions. The system is therefore capable of handling dynamic input variations without risk of saturation or mechanical overstress. The sinusoidal excitation further validates the robustness of the design, as it simulates a continuous cyclic load that resembles realistic operating scenarios.

As a result, the absence of a counter-mass does not compromise the functionality or safety of the system, and the positioner can operate reliably within the specified torque limits. These findings reinforce the suitability of the chosen drivetrain and provide a solid foundation for subsequent mechanical integration and prototype development.

The graph below illustrates the configuration with the addition of a countermass. In this case, the torque demand is significantly adjusted and reduced, demonstrating the positive effect of the countermass on balancing system inertia and improving overall dynamic performance.

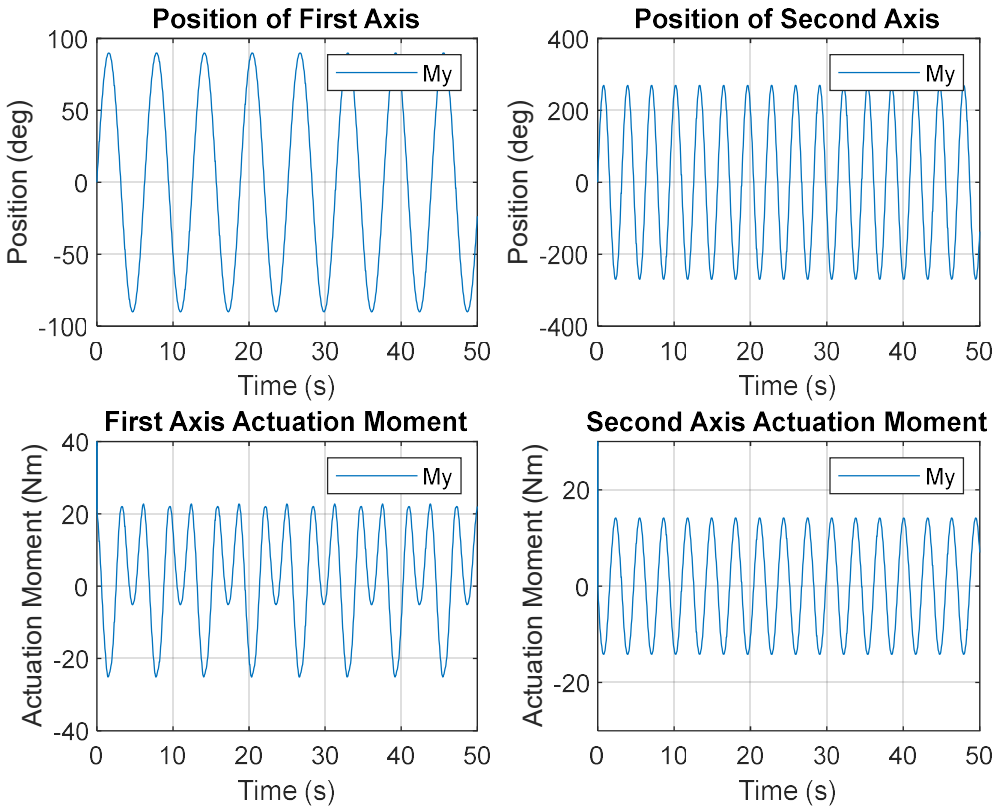

Figure A22. Actuating Moment Response With Countermass

In conclusion, the dynamic evaluation confirmed that the positioner operates well within the defined torque limits, and the obtained results indicate that the overall dynamic performance is satisfactory and consistent with the design objectives.

Appendix B

This report presents a comprehensive overview of the key components of the robotic system. Specifically, it covers the robot, the positioner and their measurements. Also, this report focuses on the types of end effectors utilized, and the master-slave structure. Additionally, the report details the dimensions of the cage

Robotic arm:

The robotic arm belongs to the Fanuc CRX series. Its name is CRX-30i. The structure of this robot and symbol of the link length are shown at figure B1. b. For the CRX-30i d_1 equal 370mm, d_2 and d_3 equal to each other (W is 537 mm), d_4 equal 750 mm, d_5 equal 185 mm, d_6 equal 180 mm and a_2 equal 950mm. All joints have limits for their motions range and maximum speed of joints. Let's symbol motions range as J_i and maximum speed as J_i'. These values are shown at table.1. Additionally, robots' repeatability equal $\pm 0.05^o$.

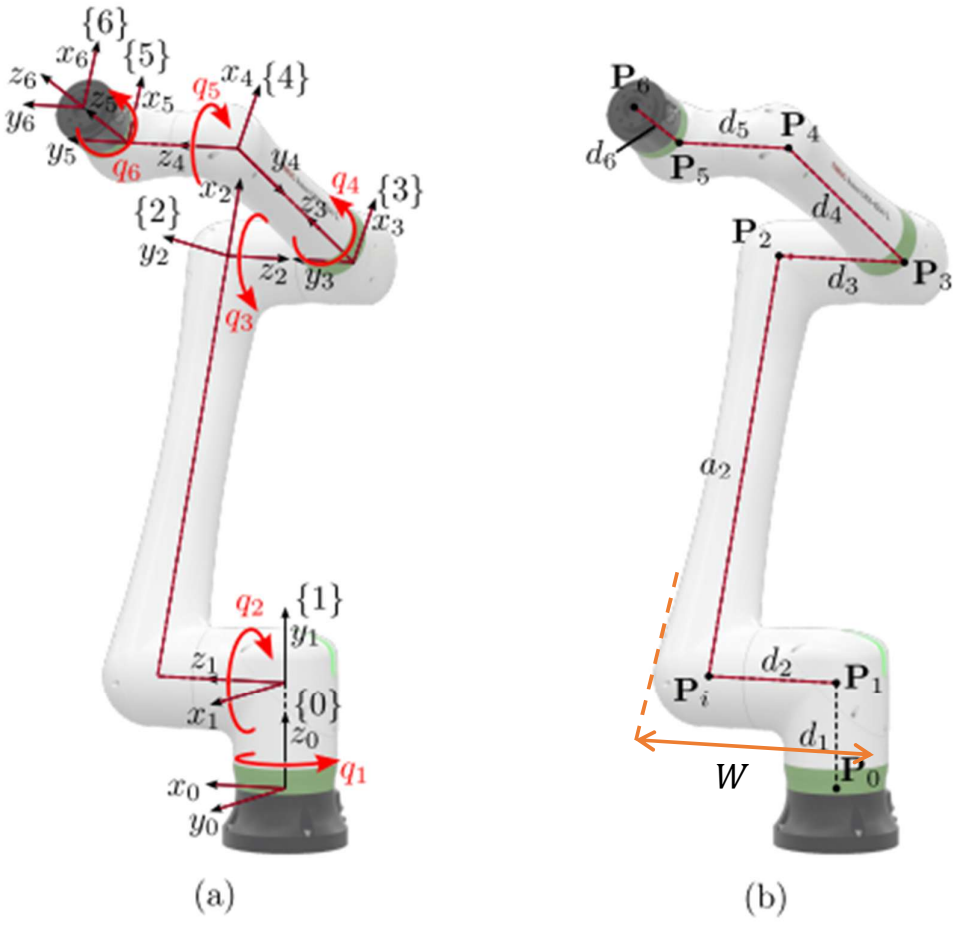

Figure B1. Fanuc CRX series robotic arm structure [B.1]

Table B.1. Motion range and maximum speed of CRX-30i's Joints

Motion range (deg)					
J_1	J_2	J_3	J_4	J_5	J_6
360	360	540	380	360	450
Maximum speed (deg/sec)					
J_1'	J_2'	J_3'	J_4'	J_5'	J_6'
80	80	120	180	180	180

CRX-30i has some special condition. Firstly, it isn't a spherical robot. Coordinates of the end-effector are directly related to all joint angels instead of the last one not just first three. Orientation is also related to all joint values. Also z_0 axis and y_4 axis (axes are shown at the figure1.a) coincide for every situation. Also z_4 and z_6 axes are perpendicular to each other.

Positioner:

The system also has a positioner. This positioner has 2 revoulute joints. That's mean the system has extra 2 DoF. This positioner makes a redundant system. This positioner was designed by a project member. The dimensions of the positioner are shown at figure B2 as a technical drawing.

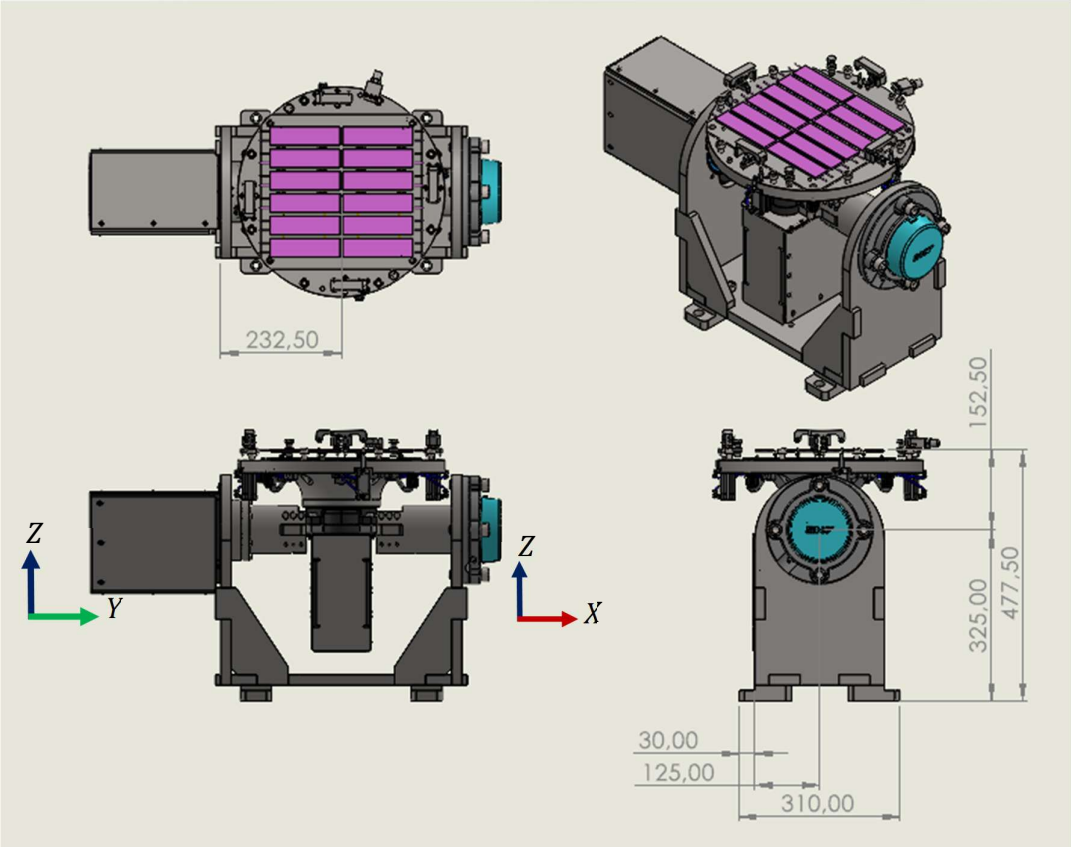

Figure B2. Positioner dimensions

Master:

To connect between end-effector and tools master-slave structure is used. Master part is located at the end effector and slave part located at the tools. Thus, at this part only master structure is shown. Slave structure added the end effectors, and it is shown with their parts. At figure B3. master structure dimension are given.

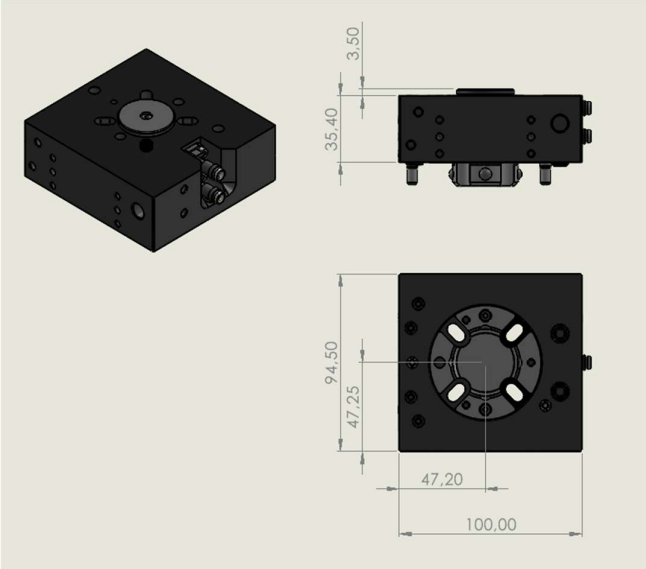

Figure B3. Master structure

End effector- Griper-slave:

Griper, slave structure and their dimensions are shown at figure B4.

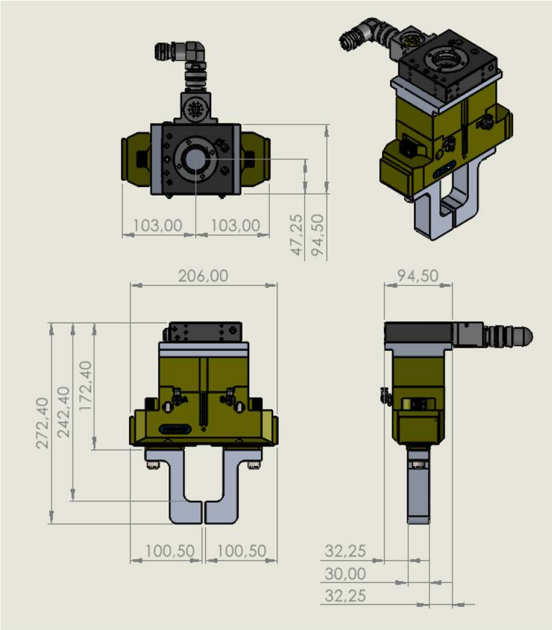

Figure B4. Griper structure with slave

End effector- machining-slave:

Machining end-effector with slave structure and their dimensions are shown at figure B5.

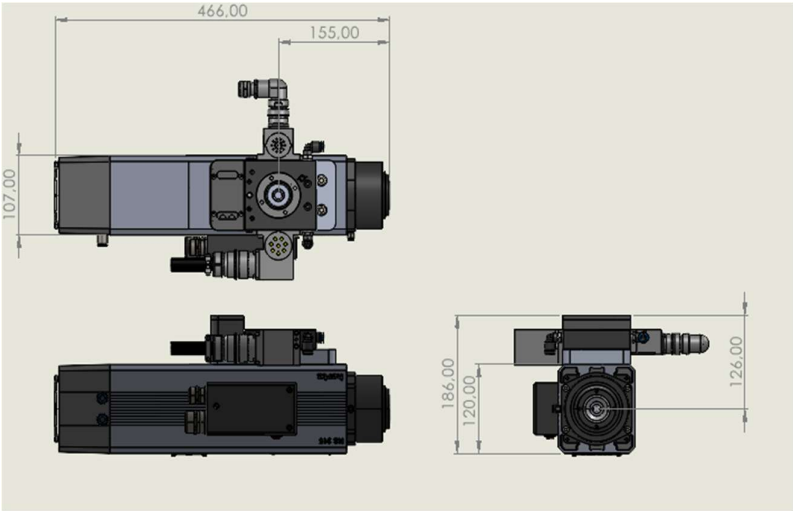

Figure B5. Machining end-effector structure with slave

End effector- additive manufacturing:

Additive manufacturing end-effector structure and its dimensions are shown at figure B6.

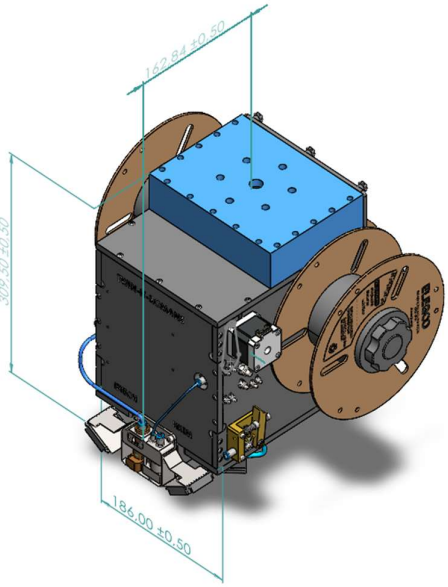

Figure B6. Additive manufacturing end-effector structure

B. References

[B.1] Carbonari L., Palpacelli M.C., and Callegari M., “Inverse Kinematics of a Class of 6R Collaborative Robots with Non-Spherical Wrist,” Robotics 12, no. 2: 36. 2023

Appendix C

Kinematics of the Robot Arm:

For of the kinematic formulation, [C.1] book was used. Section 9.1 of this book provides a detailed discussion on the Puma manipulators. The forward and inverse kinematic equations for the robot were derived. For the kinematic representation of the arm, the coordinate frames in Figure B.1 and the Denavit-Hartenberg parameters in Table C.1 are used.

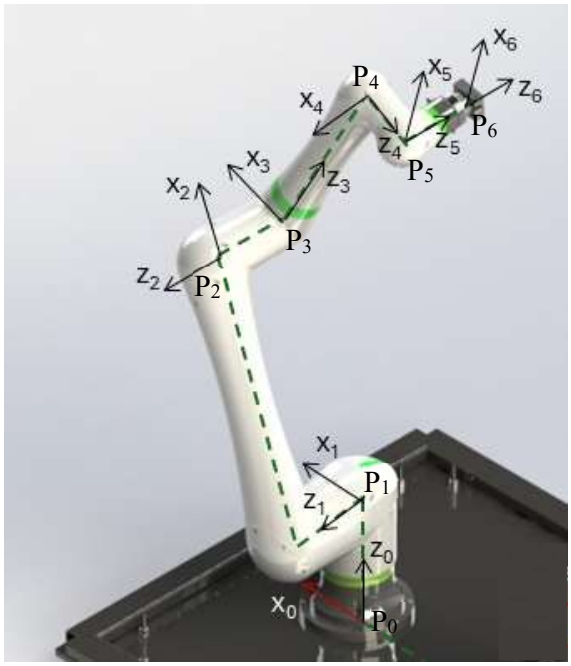

Figure C1. Coordinate frames of the robotic arm

Table B.1. DH parameters of the robot arm

i	θ_i (rad)	a_i (mm)	d_i (mm)	α_i
1	$-\pi/2$	0	$d_1 = 370$	θ_1
2	0	$a_2 = 950$	$d_2 = -200$	θ_2
3	$\pi/2$	0	$d_3 = 200$	θ_3
4	$-\pi/2$	0	$d_4 = 750$	θ_4
5	$\pi/2$	0	$d_5 = 185$	θ_5
6	0	0	$d_6 = 180$	θ_6

The task space is parametrized as the (x, y, z) coordinates of point P_6 (Figure 10) for the end-effector point, and a 123 Euler angle sequence (θ, θ, θ). Orientation matrices (parametrized with joint angles and task space angles):

$$[C] = e^{\theta_1 \tilde{u}_3} e^{-\frac{\pi}{2}\tilde{u}_1} e^{\theta_{23}\tilde{u}_3} e^{\frac{\pi}{2}\tilde{u}_1} e^{\theta_4 \tilde{u}_3} e^{-\frac{\pi}{2}\tilde{u}_1} e^{\theta_5 \tilde{u}_3} e^{\frac{\pi}{2}\tilde{u}_1} e^{\theta_6 \tilde{u}_3} = e^{\theta_1 \tilde{u}_3} e^{\theta_{23}\tilde{u}_2} e^{\theta_4 \tilde{u}_3} e^{\theta_5 \tilde{u}_2} e^{\theta_6 \tilde{u}_3}$$
$$= \begin{bmatrix} c\theta_1 & -s\theta_1 & 0 \\ s\theta_1 & c\theta_1 & 0 \\ 0 & 0 & 1 \end{bmatrix} \begin{bmatrix} c\theta_{23} & 0 & s\theta_{23} \\ 0 & 1 & 0 \\ -s\theta_{23} & 0 & c\theta_{23} \end{bmatrix} \begin{bmatrix} c\theta_4 & -s\theta_4 & 0 \\ s\theta_4 & c\theta_4 & 0 \\ 0 & 0 & 1 \end{bmatrix} \begin{bmatrix} c\theta_5 & 0 & s\theta_5 \\ 0 & 1 & 0 \\ -s\theta_5 & 0 & c\theta_5 \end{bmatrix} \begin{bmatrix} c\theta_6 & -s\theta_6 & 0 \\ s\theta_6 & c\theta_6 & 0 \\ 0 & 0 & 1 \end{bmatrix}$$
$$= \begin{bmatrix} C_{11} & C_{12} & C_{13} \\ C_{21} & C_{22} & C_{23} \\ C_{31} & C_{32} & C_{33} \end{bmatrix} \quad \text{(C.1)}$$

$$[C] = e^{\gamma \tilde{u}_3} e^{\beta \tilde{u}_2} e^{\phi \tilde{u}_3} = \begin{bmatrix} c\gamma & -s\gamma & 0 \\ s\gamma & c\gamma & 0 \\ 0 & 0 & 1 \end{bmatrix} \begin{bmatrix} c\beta & 0 & s\beta \\ 0 & 1 & 0 \\ -s\beta & 0 & c\beta \end{bmatrix} \begin{bmatrix} c\phi & -s\phi & 0 \\ s\phi & c\phi & 0 \\ 0 & 0 & 1 \end{bmatrix}$$
$$= \begin{bmatrix} c\gamma c\beta c\phi - s\gamma s\phi & -c\gamma c\beta s\phi - s\gamma c\phi & c\gamma s\beta \\ s\gamma c\beta c\phi + c\gamma s\phi & -s\gamma c\beta s\phi + c\gamma c\phi & s\gamma s\beta \\ -s\beta c\phi & s\beta s\phi & c\beta \end{bmatrix} \quad \text{(C.2)}$$

Solving for □, □, □:

$$\phi = \text{atan2}\left(\frac{-C_{12}}{c\beta}, \frac{C_{11}}{c\beta}\right)$$
$$= \tan^{-1}\left(-\frac{c\theta_1 c\theta_{23}(-c\theta_4 c\theta_5 s\theta_6 - s\theta_4 c\theta_6) - s\theta_1(-s\theta_4 c\theta_5 s\theta_6 + c\theta_4 c\theta_6) + c\theta_1 s\theta_{23}(\ )}{c\theta_1 c\theta_{23}(c\theta_4 c\theta_5 c\theta_6 - s\theta_4 s\theta_6) - s\theta_1(s\theta_4 c\theta_5 c\theta_6 + c\theta_4 s\theta_6) + c\theta_1 s\theta_{23}(-s}\right) \quad \text{(C.3}$$

$$\gamma = \text{atan2}\left(-\frac{C_{23}}{c\beta}, \frac{C_{33}}{c\beta}\right) = \tan^{-1}\left(-\frac{s\theta_1 c\theta_{23} c\theta_4 s\theta_5 + c\theta_1 s\theta_4 s\theta_5 + s\theta_1 s\theta_{23} c\theta_5}{-s\theta_{23} c\theta_4 s\theta_5 + c\theta_{23} c\theta_5}\right) \quad \text{(C.4)}$$

Position equations:

$$\bar{P}_6 = d_1 \bar{u}_3 + a_2 C_2 \bar{u}_1 + d_4 C_3 \bar{u}_3 + d_5 C_4 \bar{u}_3 + d_6 C_6 \bar{u}_3 \quad \text{(C.5)}$$

$$= d_1 \bar{u}_3 + a_2 e^{\theta_1 \tilde{u}_3} e^{\theta_2 \tilde{u}_2} e^{-\frac{\pi}{2}\tilde{u}_1} \bar{u}_1 + d_4 e^{\theta_1 \tilde{u}_3} e^{\theta_{23}\tilde{u}_2} \bar{u}_3 + d_5 e^{\theta_1 \tilde{u}_3} e^{\theta_{23}\tilde{u}_2} e^{\theta_4 \tilde{u}_3} e^{-\frac{\pi}{2}\tilde{u}_1} \bar{u}_3 + d_6 e^{\theta_1 \tilde{u}_3} e^{\theta_{23}\tilde{u}_2} e^{\theta_4 \tilde{u}_3} e^{\theta_5 \tilde{u}_2} e^{\theta_6 \tilde{u}_3} \bar{u}_3 \quad \text{(C.6)}$$

$$= d_1 \bar{u}_3 + a_2 e^{\theta_1 \tilde{u}_3} e^{\theta_2 \tilde{u}_2} \bar{u}_1 + d_4 e^{\theta_1 \tilde{u}_3} e^{\theta_{23}\tilde{u}_2} \bar{u}_3 + d_5 e^{\theta_1 \tilde{u}_3} e^{\theta_{23}\tilde{u}_2} e^{\theta_4 \tilde{u}_3} \bar{u}_2 + d_6 e^{\theta_1 \tilde{u}_3} e^{\theta_{23}\tilde{u}_2} e^{\theta_4 \tilde{u}_3} e^{\theta_5 \tilde{u}_2} \bar{u}_3 \quad \text{(C.7)}$$

$$= d_1 \bar{u}_3 + a_2 e^{\theta_1 \tilde{u}_3} e^{\theta_2 \tilde{u}_2} \bar{u}_1 + d_4 e^{\theta_1 \tilde{u}_3} e^{\theta_{23}\tilde{u}_2} \bar{u}_3 + d_5 e^{\theta_1 \tilde{u}_3} e^{\theta_{23}\tilde{u}_2} e^{\theta_4 \tilde{u}_3} \bar{u}_2 + d_6 e^{\theta_1 \tilde{u}_3} e^{\theta_{23}\tilde{u}_2} e^{\theta_4 \tilde{u}_3} e^{\theta_5 \tilde{u}_2} \bar{u}_3 \quad \text{(C.8)}$$

$$\begin{aligned}\bar{P}_6 = d_1\begin{bmatrix}0\\0\\1\end{bmatrix} + a_2\begin{bmatrix}c\theta_1 & -s\theta_1 & 0\\ s\theta_1 & c\theta_1 & 0\\ 0 & 0 & 1\end{bmatrix}\begin{bmatrix}c\theta_2 & 0 & s\theta_2\\ 0 & 1 & 0\\ -s\theta_2 & 0 & c\theta_2\end{bmatrix}\begin{bmatrix}1\\0\\0\end{bmatrix}\\ + d_4\begin{bmatrix}c\theta_1 & -s\theta_1 & 0\\ s\theta_1 & c\theta_1 & 0\\ 0 & 0 & 1\end{bmatrix}\begin{bmatrix}c\theta_{23} & 0 & s\theta_{23}\\ 0 & 1 & 0\\ -s\theta_{23} & 0 & c\theta_{23}\end{bmatrix}\begin{bmatrix}0\\0\\1\end{bmatrix}\\ + d_5\begin{bmatrix}c\theta_1 & -s\theta_1 & 0\\ s\theta_1 & c\theta_1 & 0\\ 0 & 0 & 1\end{bmatrix}\begin{bmatrix}c\theta_{23} & 0 & s\theta_{23}\\ 0 & 1 & 0\\ -s\theta_{23} & 0 & c\theta_{23}\end{bmatrix}\begin{bmatrix}c\theta_4 & -s\theta_4 & 0\\ s\theta_4 & c\theta_4 & 0\\ 0 & 0 & 1\end{bmatrix}\begin{bmatrix}0\\1\\0\end{bmatrix}\\ + d_6\begin{bmatrix}c\theta_1 & -s\theta_1 & 0\\ s\theta_1 & c\theta_1 & 0\\ 0 & 0 & 1\end{bmatrix}\begin{bmatrix}c\theta_{23} & 0 & s\theta_{23}\\ 0 & 1 & 0\\ -s\theta_{23} & 0 & c\theta_{23}\end{bmatrix}\begin{bmatrix}c\theta_4 & -s\theta_4 & 0\\ s\theta_4 & c\theta_4 & 0\\ 0 & 0 & 1\end{bmatrix}\begin{bmatrix}c\theta_5 & 0 & s\theta_5\\ 0 & 1 & 0\\ -s\theta_5 & 0 & c\theta_5\end{bmatrix}\begin{bmatrix}0\\0\\1\end{bmatrix}\end{aligned} \quad (C.9)$$

$$\begin{aligned}\bar{P}_6 = d_1\begin{bmatrix}0\\0\\1\end{bmatrix} + a_2\begin{bmatrix}c\theta_1c\theta_2\\ s\theta_1c\theta_2\\ -s\theta_2\end{bmatrix} + d_4\begin{bmatrix}c\theta_1s\theta_{23}\\ s\theta_1s\theta_{23}\\ c\theta_{23}\end{bmatrix} + d_5\begin{bmatrix}-c\theta_1c\theta_{23}s\theta_4 - s\theta_1c\theta_4\\ -s\theta_1c\theta_{23}s\theta_4 + c\theta_1c\theta_4\\ s\theta_{23}s\theta_4\end{bmatrix}\\ + d_6\begin{bmatrix}c\theta_1c\theta_{23}c\theta_4s\theta_5 - s\theta_1s\theta_4s\theta_5 + c\theta_1s\theta_{23}c\theta_5\\ s\theta_1c\theta_{23}c\theta_4s\theta_5 + c\theta_1s\theta_4s\theta_5 + s\theta_1s\theta_{23}c\theta_5\\ -s\theta_{23}c\theta_4s\theta_5 + c\theta_{23}c\theta_5\end{bmatrix}\end{aligned} \quad (C.10)$$

Due to the non-spherical wrist of the robot, it is not possible to obtain an analytical solution for the inverse kinematics. The calculations are reduced to a single equation with a single unknown, and this is solved numerically. The Newton-Raphson method was utilized to facilitate the solution. The generated equations are presented below.

Orientation equation:

$$[C_6] = \begin{bmatrix}C_{11} & C_{12}C_{13}\\ C_{21} & C_{22}C_{23}\\ C_{31} & C_{32}C_{33}\end{bmatrix}$$

$$= e^{\theta_1\tilde{u}_3}e^{-\frac{\pi}{2}\tilde{u}_1}e^{\theta_{23}\tilde{u}_3}e^{\frac{\pi}{2}\tilde{u}_1}e^{\theta_4\tilde{u}_3}e^{-\frac{\pi}{2}\tilde{u}_1}e^{\theta_5\tilde{u}_3}e^{\frac{\pi}{2}\tilde{u}_1}e^{\theta_6\tilde{u}_3} = e^{\theta_1\tilde{u}_3}e^{\theta_{23}\tilde{u}_2}e^{\theta_4\tilde{u}_3}e^{\theta_5\tilde{u}_2}e^{\theta_6\tilde{u}_3} \quad (C.11)$$

Rearranging:

$$e^{-\theta_4\tilde{u}_3}e^{-\theta_{23}\tilde{u}_2}e^{-\theta_1\tilde{u}_3}C_6 = C^* = e^{\theta_5\tilde{u}_2}e^{\theta_6\tilde{u}_3} =$$

$$\begin{bmatrix}c\theta_5 & 0 & s\theta_5\\ 0 & 1 & 0\\ -s\theta_5 & 0 & c\theta_5\end{bmatrix}\begin{bmatrix}c\theta_6 & -s\theta_6 & 0\\ s\theta_6 & c_{\theta6} & 0\\ 0 & 0 & 1\end{bmatrix} = \begin{bmatrix}c_{\theta5}c\theta_6 & -c\theta_5s\theta_6 & s\theta_5\\ s\theta_6 & c\theta_6 & 0\\ -s\theta_5c\theta_6 & s\theta_5s\theta_6 & c\theta_5\end{bmatrix} \quad (C.12)$$

Or

$$e^{\frac{\pi}{2}\tilde{u}_1}e^{-\theta_4\tilde{u}_3}e^{-\theta_{23}\tilde{u}_2}e^{-\theta_1\tilde{u}_3}C_6 = C^{**} = e^{\theta_5\tilde{u}_3}e^{\frac{\pi}{2}\tilde{u}_1}e^{\theta_6\tilde{u}_3}$$
$$= \begin{bmatrix} c\theta_5 & -s\theta_5 & 0 \\ s\theta_5 & c\theta_5 & 0 \\ 0 & 0 & 1 \end{bmatrix}\begin{bmatrix} 1 & 0 & 0 \\ 0 & 0 & -1 \\ 0 & 1 & 0 \end{bmatrix}\begin{bmatrix} c\theta_6 & -s\theta_6 & 0 \\ s\theta_6 & c\theta_6 & 0 \\ 0 & 0 & 1 \end{bmatrix}$$
$$= \begin{bmatrix} c\theta_5 & -s\theta_5 & 0 \\ s\theta_5 & c\theta_5 & 0 \\ 0 & 0 & 1 \end{bmatrix}\begin{bmatrix} c\theta_6 & -s\theta_6 & 0 \\ 0 & 0 & -1 \\ s\theta_6 & c\theta_6 & 0 \end{bmatrix} = \begin{bmatrix} c\theta_5c\theta_6 & -c\theta_5s\theta_6 & s\theta_5 \\ s\theta_5c\theta_6 & -s\theta_5s\theta_6 & -c\theta_5 \\ s\theta_6 & c_6 & 0 \end{bmatrix}$$

Then

$$[0 \quad 1 \quad 0]e^{-\theta_4\tilde{u}_3}e^{-\theta_{23}\tilde{u}_2}e^{-\theta_1\tilde{u}_3}C_6\begin{bmatrix} 0 \\ 0 \\ 1 \end{bmatrix} = 0 \tag{C.13}$$

$$\begin{aligned}\bar{P} = \overline{P_1P_5} = \bar{P}_6 - d_6C_6\bar{u}_3 - d_1\bar{u}_3 = a_2C_2\bar{u}_1 + d_4C_3\bar{u}_3 + d_5C_4\bar{u}_3 \\ = e^{\theta_1\tilde{u}_3}e^{-\frac{\pi}{2}\tilde{u}_1}e^{\theta_2\tilde{u}_3}\left(a_2\bar{u}_1 + d_4e^{\theta_3\tilde{u}_3}e^{\frac{\pi}{2}\tilde{u}_1}\bar{u}_3\right. \\ \left. + d_5e^{\theta_3\tilde{u}_3}e^{\frac{\pi}{2}\tilde{u}_1}e^{\theta_4\tilde{u}_3}e^{-\frac{\pi}{2}\tilde{u}_1}\bar{u}_3\right)\end{aligned} \tag{C.14}$$

$$c_{13}(-s\theta_1c\theta_4 - c\theta_1s\theta_4c\theta_{23}) + c_{23}(c\theta_1c\theta_4 - s\theta_1s\theta_4c\theta_{23}) + c_{33}(s\theta_4s\theta_{23}) = 0 \tag{C.15}$$

$$\begin{bmatrix} P_{5x} \\ P_{5y} \\ P_{5z} - d_1 \end{bmatrix} = \begin{bmatrix} c\theta_1c\theta_2 & -c\theta_1s\theta_2 & -s\theta_1 \\ s\theta_1c\theta_2 & -s\theta_1s\theta_2 & -c\theta_1 \\ s\theta_2 & -c\theta_2 & 0 \end{bmatrix}\begin{bmatrix} a_2 + d_4s\theta_3 - d_5c\theta_3s\theta_4 \\ -d_4c\theta_3 - d_5s\theta_3s\theta_4 \\ d_5c\theta_4 \end{bmatrix} \tag{C.16}$$

$$\begin{bmatrix} c\theta_1c\theta_2 & -c\theta_1s\theta_2 & -s\theta_1 \\ s\theta_1c\theta_2 & -s\theta_1s\theta_2 & -c\theta_1 \\ s\theta_2 & -c\theta_2 & 0 \end{bmatrix}^T\begin{bmatrix} P_{5x} \\ P_{5y} \\ P_{5z} - d_1 \end{bmatrix} = \begin{bmatrix} a_2 + d_4s\theta_3 - d_5c\theta_3s\theta_4 \\ -d_4c\theta_3 - d_5s\theta_3s\theta_4 \\ d_5c\theta_4 \end{bmatrix} \tag{C.17}$$

$$\begin{bmatrix} c\theta_1c\theta_2 & s\theta_1c\theta_2 & -s\theta_2 \\ -c\theta_1s\theta_2 & -s\theta_1s\theta_2 & -c\theta_2 \\ -s\theta_1 & c\theta_1 & 0 \end{bmatrix}\begin{bmatrix} P_{5x} \\ P_{5y} \\ P_{5z} - d_1 \end{bmatrix} = \begin{bmatrix} a_2 + d_4s\theta_3 - d_5c\theta_3s\theta_4 \\ -d_4c\theta_3 - d_5s\theta_3s\theta_4 \\ d_5c\theta_4 \end{bmatrix} \tag{C.18}$$

$$P_{5x}c\theta_1c\theta_2 + P_{5y}s\theta_1c\theta_2 - (P_{5z} - d_1)s\theta_2 = a_2 + d_4s\theta_3 - d_5c\theta_3s\theta_4 \tag{C.19}$$

$$-P_{5x}c\theta_1s\theta_2 - P_{5y}s\theta_1s\theta_2 - (P_{5z} - d_1)c\theta_2 = -d_4c\theta_3 - d_5s\theta_3s\theta_4 \tag{C.20}$$

$$-P_{5x}s\theta_1 + P_{5y}c\theta_1 = d_5c\theta_4 \tag{C.21}$$

Let's define the connection between θ_1 and θ_4 with equation 4.2.

$$c\theta_4 = \frac{-P_{5x}s\theta_1 + P_{5y}c\theta_1}{d_5} \tag{C.22}$$

$$\theta_4 = atan2\left(\sigma_3\sqrt{1 - \left(\frac{-P_{5x}s\theta_1 + P_{5y}c\theta_1}{d_5}\right)^2}, \frac{-P_{5x}s\theta_1 + P_{5y}c\theta_1}{d_5}\right) \tag{C.23}$$

θ_3 can be defined as a θ_1 and θ_4 function with equation 2.2 and 3.2

$$\begin{aligned}&\left(P_{5x}c\theta_1c\theta_2+P_{5y}s\theta_1c\theta_2-(P_{5z}-d_1)s\theta_2\right)^2\\&\quad+\left(-P_{5x}c\theta_1s\theta_2-P_{5y}s\theta_1s\theta_2-(P_{5z}-d_1)c\theta_2\right)^2\\&\quad=(a_2+d_4s\theta_3-d_5c\theta_3s\theta_4)^2+(-d_4c\theta_3-d_5s\theta_3s\theta_4)^2\end{aligned}\tag{C.24}$$

$$\begin{aligned}&\left((P_{5x}c\theta_1+P_{5y}s\theta_1)c\theta_2-(P_{5z}-d_1)s\theta_2\right)^2\\&\quad+\left(-(P_{5x}c\theta_1-P_{5y}s\theta_1)s\theta_2-(P_{5z}-d_1)c\theta_2\right)^2\\&\quad=a_2^2+2a_2(d_4s\theta_3-d_5c\theta_3s\theta_4)+(d_4s\theta_3-d_5c\theta_3s\theta_4)^2\\&\quad+(-d_4c\theta_3-d_5s\theta_3s\theta_4)^2\end{aligned}\tag{C.25}$$

$$\begin{aligned}&\left(P_{5x}c\theta_1+P_{5y}s\theta_1\right)^2+(P_{5z}-d_1)^2\\&\quad=a_2^2+2a_2(d_4s\theta_3-d_5c\theta_3s\theta_4)+{d_4}^2+d_5^2s^2\theta_4\end{aligned}\tag{C.26}$$

$$\begin{aligned}d_4s\theta_3-d_5s\theta_4c\theta_3&=\frac{\left(P_{5x}c\theta_1+P_{5y}s\theta_1\right)^2+(P_{5z}-d_1)^2-a_2^2-{d_4}^2-d_5^2s^2\theta_4}{2a_2}\\&=D_3=R_3\sin(\theta_3+\phi_3)\end{aligned}\tag{C.27}$$

$$R_3=\sqrt{d_4^2+d_5^2s^2\theta_4}\tag{C.28}$$

$$\theta_3+\phi_3=atan2\left(\frac{D_3}{R_3},\sigma_3\sqrt{1-\left(\frac{D_3}{R_3}\right)^2}\right)\tag{C.29}$$

$$\phi_3=atan2(-d_5s\theta_4,d_4)\tag{C.30}$$

$$\theta_3=atan2\left(\frac{D_3}{R_3},\sigma_3\sqrt{1-\left(\frac{D_3}{R_3}\right)^2}\right)-atan2(-d_5s\theta_4,d_4)\tag{C.31}$$

θ_3 can be defined as a θ_1 and θ_4 function with sum of the equations 2.2 and 3.2

$$(P_{5x}c\theta_1+P_{5y}s\theta_1)c\theta_2-(P_{5z}-d_1)s\theta_2=a_2+d_4s\theta_3-d_5c\theta_3s\theta_4\tag{C.32}$$

$$(-P_{5x}c\theta_1-P_{5y}s\theta_1)s\theta_2-(P_{5z}-d_1)c\theta_2=-d_4c\theta_3-d_5s\theta_3s\theta_4\tag{C.33}$$

$$\begin{aligned}&P_{5x}c\theta_1c\theta_2+P_{5y}s\theta_1c\theta_2-(P_{5z}-d_1)s\theta_2-P_{5x}c\theta_1s\theta_2-P_{5y}s\theta_1s\theta_2-(P_{5z}-d_1)c\theta_2\\&\quad=a_2+d_4s\theta_3-d_5c\theta_3s\theta_4-d_4c\theta_3-d_5s\theta_3s\theta_4\end{aligned}\tag{C.34}$$

$$\begin{aligned}&\left(P_{5x}c\theta_1+P_{5y}s\theta_1-P_{5z}+d_1\right)c\theta_2-\left(P_{5z}-d_1+P_{5x}c\theta_1+P_{5y}s\theta_1\right)s\theta_2\\&\quad=a_2+d_4s\theta_3-d_5c\theta_3s\theta_4-d_4c\theta_3-d_5s\theta_3s\theta_4=D_2\\&\quad=R_2\sin(\theta_2+\phi_2)\end{aligned}\tag{C.35}$$

$$R_2=\sqrt{\left(P_{5x}c\theta_1+P_{5y}s\theta_1-P_{5z}+d_1\right)^2+\left(P_{5z}-d_1+P_{5x}c\theta_1+P_{5y}s\theta_1\right)^2}\tag{C.36}$$

$$\theta_2 + \phi_2 = atan2\left(\frac{D_2}{R_2}, \sigma_3\sqrt{1-\left(\frac{D_2}{R_2}\right)^2}\right) \tag{C.37}$$

$$\phi_2 = atan2\left(\left(P_{5x}c\theta_1 + P_{5y}s\theta_1 - P_{5z} + d_1\right), -\left(P_{5z} - d_1 + P_{5x}c\theta_1 + P_{5y}s\theta_1\right)\right) \tag{C.38}$$

$$\begin{aligned}\theta_2 = atan2\left(\frac{D_2}{R_2}, \sigma_3\sqrt{1-\left(\frac{D_2}{R_2}\right)^2}\right) \\ - atan2\left(\left(P_{5x}c\theta_1 + P_{5y}s\theta_1 - P_{5z} + d_1\right), -\left(P_{5z} - d_1 + P_{5x}c\theta_1 \right.\right. \\ \left.\left. + P_{5y}s\theta_1\right)\right)\end{aligned} \tag{C.39}$$

Now we can define θ_{23}.

$$\begin{aligned}\theta_{23} = \theta_2 + \theta_3 = atan2\left(\frac{D_3}{R_3}, \sigma_3\sqrt{1-\left(\frac{D_3}{R_3}\right)^2}\right) - atan2(-d_5 s\theta_4, d_4) \\ + atan2\left(\frac{D_2}{R_2}, \sigma_3\sqrt{1-\left(\frac{D_2}{R_2}\right)^2}\right) \\ - atan2\left(\left(P_{5x}c\theta_1 + P_{5y}s\theta_1 - P_{5z} + d_1\right), -\left(P_{5z} - d_1 + P_{5x}c\theta_1 \right.\right. \\ \left.\left. + P_{5y}s\theta_1\right)\right)\end{aligned} \tag{C.40}$$

θ_4 and θ_{23} depend on θ_1. θ_1 can be numerically solved from equation 1.2:

$$c_{13}(-s\theta_1 c\theta_4 - c\theta_1 s\theta_4 c\theta_{23}) + c_{23}(c\theta_1 c\theta_4 - s\theta_1 s\theta_4 c\theta_{23}) + c_{33}(s\theta_4 s\theta_{23}) = 0 \tag{C.41}$$

For θ_5 and θ_6:

$$\begin{aligned}e^{-\theta_{23}u_2}e^{-\theta_1 u_3}C_6 = C' = e^{\theta_4 u_3}e^{\theta_5 u_2}e^{\theta_6 u_3} \\ = \begin{bmatrix} -s\theta_4 s\theta_6 + c\theta_4 c\theta_6 & -s\theta_4 c\theta_6 - c\theta_4 c\theta_5 s\theta_6 & c\theta_4 s\theta_5 \\ s\theta_4 c\theta_5 c\theta_6 + c\theta_4 s\theta_6 & -s\theta_4 c\theta_5 s\theta_6 + c\theta_4 s\theta_6 & s\theta_4 s\theta_5 \\ -s\theta_5 c\theta_6 & s\theta_5 s\theta_6 & c\theta_5 \end{bmatrix}\end{aligned} \tag{C.42}$$

$$C'_{33} = c\theta_5 \tag{C.43}$$

$$\theta_5 = atan2\left(\sigma_5\sqrt{1 - {C'_{33}}^2}, C'_{33}\right) \tag{C.44}$$

$$C'_{32} = s\theta_5 \tag{C.45}$$

$$s\theta_6 \tag{C.46}$$

$$C'_{31} = -s\theta_5 c\theta_6 \tag{C.47}$$

$$\theta_6 = atan2(\sigma_5 C'_{32}, -\sigma_5 C'_{31}) \tag{C.48}$$

Inverse and Froward Kinematics of the positioner:

The robot arm and the positioner are shown together in Figure C2. The DH parameters are given in Table C2. Variable values (x_v, y_v, θ_v) are defined in the DH table. x_v is distance of the first axis of the arm to the positioner's universal joint center, y_v is the height above the ground and θ_v is the orientation angle of the positioner about the z-axis of the first joint of positioner measured from x_0-axis to x_{P0}-axis.

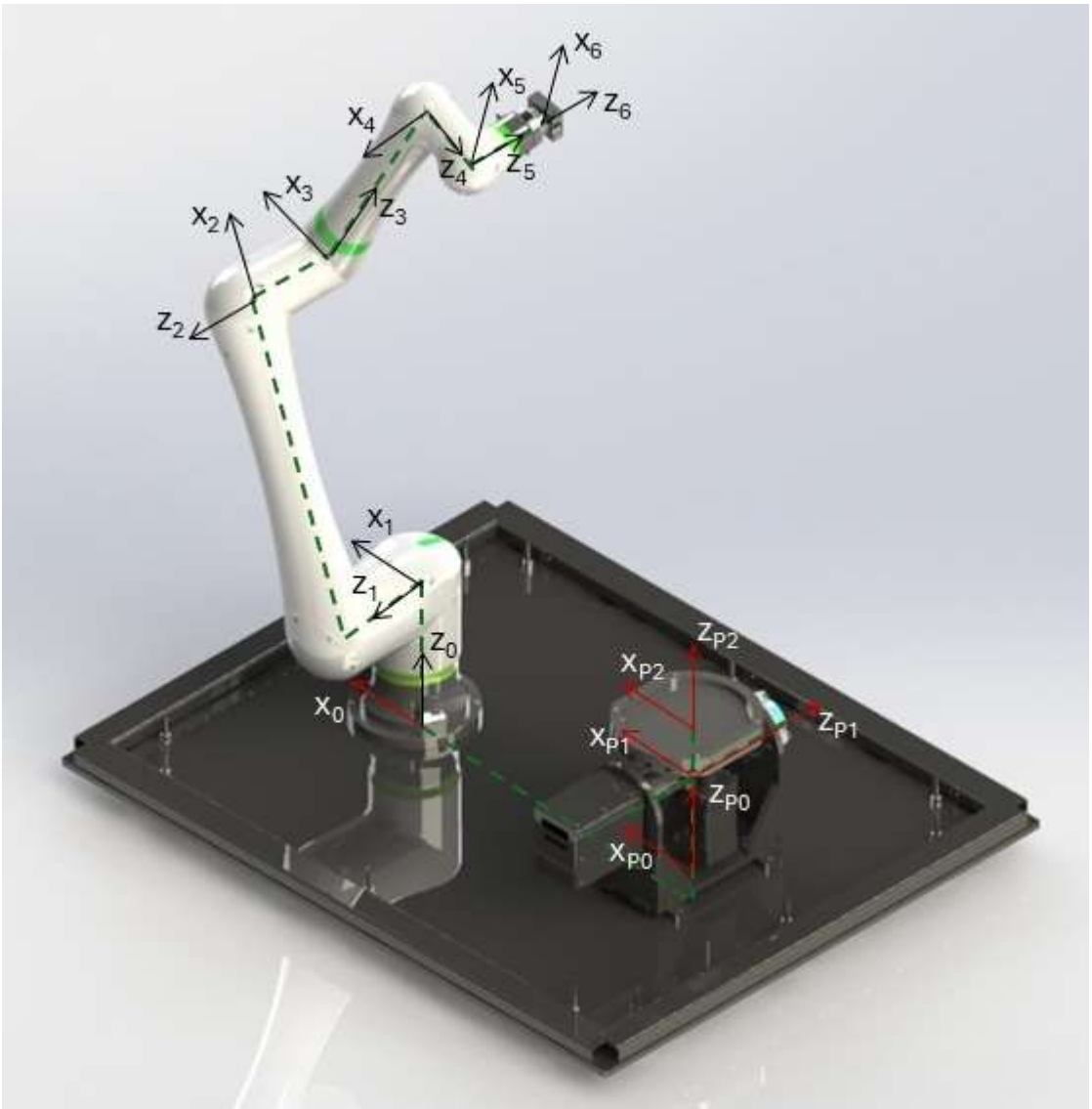

Figure C2. Joint axes of the robotic system

Table C2. DH parameters for the robot arm and the positioner

i	□ᵢ (rad)	aᵢ (mm)	dᵢ (mm)	□ᵢ
P1	□/2	0	-152.5	□P2
P0	–□/2	0	0	□P1
0	0	x_v	$-z_v - d_{P0}$(350mm)	θ_v
1	–□/2	0	$d_1 = 370$	□1
2	0	$a_2 = 950$	$d_2 = -260.4$	□2
3	□/2	0	$d_3 = 260.4$	□3
4	–□/2	0	$d_4 = 750$	□4
5	□/2	0	$d_5 = 180$	□5
6	0	0	$d_6 = 185$	□6

Let's say the center of the build plate is P_2.

$$\bar{P}_2 = \overline{OP_0} + \overline{P_0P_1} + \overline{P_1P_2} \tag{C.49}$$

$$\overline{OP_0} = -x_v\bar{u}_1 + z_v\,\bar{u}_3 \tag{C.50}$$

$$\overline{P_0P_1} = d_{P0}\,\bar{u}_3 \tag{C.51}$$

$$\overline{P_1P_2} = d_{P2}C_{p2}\bar{u}_3 \tag{C.52}$$

$$\overline{P_2} = -x_v\bar{u}_1 + z_v\,\bar{u}_3 + d_{P0}\,\bar{u}_3 + d_{P2}C_{p2}\bar{u}_3 \tag{C.53}$$

One of the coordinate of the corner of the workspace at build plate is P_3

$$\bar{P}_3 = \bar{P}_2 + 250C_{P2}\bar{u}_1 + 250C_{P2}\bar{u}_2 \tag{C.54}$$

$$[C_{P0}] = e^{\theta_v u_3} = \begin{bmatrix} c\theta_v & -s\theta_v & 0 \\ s\theta_v & c\theta_v & 0 \\ 0 & 0 & 1 \end{bmatrix} \tag{C.55}$$

$$[C_{P1}] = [C_{P0}]\, e^{\frac{\pi}{2}\tilde{u}_1} e^{\theta_{P1}\tilde{u}_3} = e^{\theta_v\tilde{u}_3} e^{\frac{\pi}{2}\tilde{u}_1} e^{\theta_{P1}\tilde{u}_3} \tag{C.56}$$

$$[C_{P1}] = \begin{bmatrix} c\theta_v & -s\theta_v & 0 \\ s\theta_v & c\theta_v & 0 \\ 0 & 0 & 1 \end{bmatrix} \begin{bmatrix} 1 & 0 & 0 \\ 0 & 0 & -1 \\ 0 & 1 & 0 \end{bmatrix} \begin{bmatrix} c\theta_{P1} & -s\theta_{P1} & 0 \\ s\theta_{P1} & c\theta_{P1} & 0 \\ 0 & 0 & 1 \end{bmatrix} \tag{C.57}$$

$$[C_{P1}] = \begin{bmatrix} c\theta_v & -s\theta_v & 0 \\ s\theta_v & c\theta_v & 0 \\ 0 & 0 & 1 \end{bmatrix} \begin{bmatrix} c\theta_{P1} & -s\theta_{P1} & 0 \\ 0 & 0 & -1 \\ s\theta_{P1} & c\theta_{P1} & 0 \end{bmatrix} = \begin{bmatrix} c\theta_v c\theta_{P1} & -c\theta_v s\theta_{P1} & s\theta_v \\ s\theta_v c\theta_{P1} & -s\theta_v s\theta_{P1} & -c\theta_v \\ s\theta_{P1} & c\theta_{P1} & 0 \end{bmatrix} \tag{C.58}$$

$$[C_{P2}] = [C_{P1}]e^{-\frac{\pi}{2}\tilde{u}_1}e^{\theta_{P2}\tilde{u}_3} = e^{\theta_{input}\tilde{u}_3}e^{\frac{\pi}{2}\tilde{u}_1}e^{\theta_{P1}\tilde{u}_3}e^{-\frac{\pi}{2}\tilde{u}_1}e^{\theta_{P2}\tilde{u}_3} = e^{\theta_{input}\tilde{u}_3}e^{-\theta_{P1}\tilde{u}_2}e^{\theta_{P2}\tilde{u}_3} \quad \text{(C.59)}$$

$$[C_{P2}] = [C_{P1}]\, e^{-\frac{\pi}{2}\tilde{u}_1}e^{\theta_{P2}\tilde{u}_3} = \begin{bmatrix} c\theta_v c\theta_{P1} & -c\theta_v s\theta_{P1} & s\theta_v \\ s\theta_v c\theta_{P1} & -s\theta_v s\theta_{P1} & -c\theta_v \\ s\theta_{P1} & c\theta_{P1} & 0 \end{bmatrix}\begin{bmatrix} 1 & 0 & 0 \\ 0 & 0 & 1 \\ 0 & -1 & 0 \end{bmatrix}\begin{bmatrix} c\theta_{P2} & -s\theta_{P2} & 0 \\ s\theta_{P2} & c\theta_{P2} & 0 \\ 0 & 0 & 1 \end{bmatrix} \quad \text{(C.60)}$$

$$[C_{P2}] = \begin{bmatrix} c\theta_v c\theta_{P1} & -c\theta_v s\theta_{P1} & s\theta_v \\ s\theta_v c\theta_{P1} & -s\theta_v s\theta_{P1} & -c\theta_v \\ s\theta_{P1} & c\theta_{P1} & 0 \end{bmatrix}\begin{bmatrix} c\theta_{P2} & -s\theta_{P2} & 0 \\ 0 & 0 & 1 \\ -s\theta_{P2} & -c\theta_{P2} & 0 \end{bmatrix} \quad \text{(C.61)}$$

$$[C_{P2}] = \begin{bmatrix} c\theta_v c\theta_{P1}c\theta_{P2} - s\theta_v s\theta_{P2} & -c\theta_v c\theta_{P1}s\theta_{P2} - s\theta_v c\theta_{P2} & -c\theta_v s\theta_{P1} \\ s\theta_v c\theta_{P1}c\theta_{P2} + c\theta_v s\theta_{P2} & -s\theta_v c\theta_{P1}s\theta_{P2} + c\theta_v c\theta_{P2} & -s\theta_v s\theta_{P1} \\ s\theta_{P1}c\theta_{P2} & -s\theta_{P1}s\theta_{P2} & c\theta_{P1} \end{bmatrix} \quad \text{(C.62)}$$

$$\bar{P}_2 = -x_v\bar{u}_1 + z_v\,\bar{u}_3 + d_{P1}\,\bar{u}_3 + d_{P2}[C_{p2}]\bar{u}_3 \quad \text{(C.63)}$$

$$\bar{P}_2 = \begin{bmatrix} -x_v \\ 0 \\ 0 \end{bmatrix} + \begin{bmatrix} 0 \\ 0 \\ z_v \end{bmatrix} + \begin{bmatrix} 0 \\ 0 \\ d_{P0} \end{bmatrix} + d_{P2}\begin{bmatrix} -c\theta_v s\theta_{P1} \\ -s\theta_v s\theta_{P1} \\ c\theta_{P1} \end{bmatrix} \quad \text{(C.64)}$$

$$\bar{P}_2 = \begin{bmatrix} -x_v - d_{P2}c\theta_v s\theta_{P1} \\ -d_{P2}s\theta_v s\theta_{P1} \\ z_v + d_{P1} + d_{P2}c\theta_{P1} \end{bmatrix} \quad \text{(C.65)}$$

Let x_{P2}, y_{P2} and z_{P2} be the coordinates of the target point on the table in the P2 coordinate frame.

$$\bar{P}_3 = \bar{P}_2 + x_{P2}[C_{P2}]\bar{u}_1 + y_{P2}[C_{P2}]\bar{u}_2 + z_{P2}[C_{P2}]\bar{u}_3 \quad \text{(C.66)}$$

$$\begin{aligned} \bar{P}_3 = \begin{bmatrix} -x_v - d_{P2}c\theta_v s\theta_{P1} \\ -d_{P2}s\theta_v s\theta_{P1} \\ z_v + d_{P0} + d_{P2}c\theta_{P1} \end{bmatrix} + x_{P2}\begin{bmatrix} c\theta_v c\theta_{P1}c\theta_{P2} - s\theta_v s\theta_{P2} \\ s\theta_v c\theta_{P1}c\theta_{P2} + c\theta_v s\theta_{P2} \\ s\theta_{P1}c\theta_{P2} \end{bmatrix} \\ + y_{P2}\begin{bmatrix} -c\theta_v c\theta_{P1}s\theta_{P2} - s\theta_v c\theta_{P2} \\ -s\theta_v c\theta_{P1}s\theta_{P2} + c\theta_v c\theta_{P2} \\ -s\theta_{P1}s\theta_{P2} \end{bmatrix} + z_{P2}\begin{bmatrix} -c\theta_v s\theta_{P1} \\ -s\theta_v s\theta_{P1} \\ c\theta_{P1} \end{bmatrix} \end{aligned} \quad \text{(C.67)}$$

Inverse Kinematics:

Orientation:

$$[C_{P2}] = e^{\gamma\tilde{u}_1}e^{\beta\tilde{u}_2}e^{\phi\tilde{u}_3} = \begin{bmatrix} 1 & 0 & 0 \\ 0 & c\gamma & -s\gamma \\ 0 & s\gamma & c\gamma \end{bmatrix}\begin{bmatrix} c\beta & 0 & s\beta \\ 0 & 1 & 0 \\ -s\beta & 0 & c\beta \end{bmatrix}\begin{bmatrix} c\phi & -s\phi & 0 \\ s\phi & c\phi & 0 \\ 0 & 0 & 1 \end{bmatrix} \quad \text{(C.68)}$$

$$[C_{P2}] = \begin{bmatrix} c\beta c\phi & -c\beta s\phi & s\beta \\ s\gamma s\beta c\phi + c\gamma s\phi & -s\gamma s\beta s\phi + c\gamma c\phi & -s\gamma c\beta \\ -c\gamma s\beta c\phi + s\gamma s\phi & c\gamma s\beta s\phi + s\gamma c\phi & c\gamma c\beta \end{bmatrix} \quad \text{(C.69)}$$

Also, we calculate same matrix before:

$$[C_{P2}] = \begin{bmatrix} c\theta_v c\theta_{P1} c\theta_{P2} - s\theta_v s\theta_{P2} & -c\theta_v c\theta_{P1} s\theta_{P2} - s\theta_v c\theta_{P2} & -c\theta_v s\theta_{P1} \\ s\theta_v c\theta_{P1} c\theta_{P2} + c\theta_v s\theta_{P2} & -s\theta_v c\theta_{P1} s\theta_{P2} + c\theta_v c\theta_{P2} & -s\theta_v s\theta_{P1} \\ s\theta_{P1} c\theta_{P2} & -s\theta_{P1} s\theta_{P2} & c\theta_{P1} \end{bmatrix} \quad \text{(C.70)}$$

For the inverse equation γ, β, Φ values are known. Thus, θ values can be found.

$$c\theta_{P1} = c\gamma c\beta \quad \text{(C.71)}$$

$$s\theta_{P1} = \sigma_{P1}\sqrt{1 - (c\gamma c\beta)^2} \quad \text{(C.72)}$$

$$\theta_{P1} = atan2(s\theta_{P1}, c\theta_{P1}) \quad \text{(C.73)}$$

$$\theta_{P2} = atan2(-c\gamma s\beta s\phi - s\gamma c\phi, -c\gamma s\beta c\phi + s\gamma s\phi) \quad \text{(C.74)}$$

C. References

[C.1] Ozgoren M. K, "Kinematics of General Spatial Mechanical Systems," Wiley, 2020.

Appendix D

D.1. Report of the work carried out

Additive manufacturing (AM), particularly fused deposition modelling (FDM), facilitates the fabrication of complex geometries with increasing flexibility and efficiency. Ensuring consistent print quality in FDM processes necessitates the development of accurate defect detection mechanisms. Attention-augmented YOLO (You Only Look Once) models have emerged as a promising solution for addressing this challenge. In this exchange study, we systematically benchmark and evaluate the performance of YOLO architectures enhanced with attention mechanisms within the context of FDM 3D printing applications. The models were trained and evaluated using representative defect datasets. The attention-augmented models demonstrate improved detection performance.

D.1.1. Motivation

Fused Deposition Modelling (FDM), which is one of the most versatile Additive Manufacturing (AM) methods for 3D printing of thermoplastic polymers such as Acrylonitrile Butadiene Styrene (ABS) and Polylactic Acid (PLA), enables the creation of complex geometries from digital designs in a cost-effective manner with shorter cycle times [D.1, D.2]. This approach employs heat to soften thermoplastic filaments extruded by the printhead which follows the path generated to create the cross-sectional geometry of the part to be fabricated so that 3D parts can be created from CAD models in a layer-by-layer approach [D.3]. Despite its many advantages such as fast production, cost efficiency, ease of access, broad material adaptation, and the ability to produce complex components, FDM is susceptible to defects such as warping, stringing, layer shifting, and extrusion inconsistencies, which compromise print quality and increase material waste [D.4, D.5]. Traditional defect detection methods, including manual inspection and basic sensor systems, are inefficient and lack the precision required for large-scale production [D.6]. This has prompted the development of automated, vision-based solutions leveraging machine vision and deep learning, particularly Convolutional Neural Networks (CNNs) such as You Look Only Once (YOLO) [D.7].

The evolution from YOLOv1 to YOLOv11 reflects significant performance enhancements [D.7]. For instance, Sani et al. improved YOLOv4 for flow defect detection in FDM and compared YOLOv3 and YOLOv4 variants for anomaly detection, emphasizing the balance between speed and precision [D.8]. They also evaluated advanced YOLOv11 models for defect detection in FDM workflows, benchmarking their performance against other YOLO variants. The YOLOv11s model achieved a mean Average Precision (mAP) of 0.8308 at IoU threshold 0.5 (mAP@0.5) and 0.5361 across IoU thresholds ranging from 0.5 to 0.95 (mAP@0.5:0.95). Attention mechanisms enhance YOLO models by improving feature focus and reducing false positives. An attention-enhanced YOLOv8 model integrating Multi-Headed Self Attention (MHSA) and Convolutional Block Attention Module (CBAM) achieved a 92.1% mAP in extrusion defect detection for large-scale FDM printing [D.8]. YOLOv11 further integrates advanced attention mechanisms to enhance feature representation and detection accuracy, primarily through its C2PSA (Convolutional block with Parallel Spatial Attention) module and Partial Self-Attention (PSA) [D.9]. The C2PSA mechanism combines parallel convolutional pathways with spatial attention, allowing the model to dynamically focus on critical regions of

an image, such as small or occluded objects, by weighting feature maps based on spatial importance. Additionally, YOLOv11 employs Partial Self-Attention to selectively apply self-attention to specific regions [D.10].

Although attention mechanisms have been explored in previous studies, the systematic benchmarking of their performance on real-world industrial datasets has received limited attention. In response, this study aims to analyse the effectiveness of attention-augmented YOLO models through a structured benchmarking approach. Five distinct attention mechanisms were carefully integrated into the YOLOv11 architecture and evaluated against a benchmark dataset, with YOLOv11 and YOLOv8 models employed as baselines. Several key performance indicators were used to assess their efficacy. The defect types analysed include warping, spaghetti, cracking, stringing, layer shifting, and curling. The results demonstrated that attention-augmented YOLO models achieved improved performance across all selected defect types, thereby enhancing object detection outcomes without considerable degradation in computational efficiency.

D.1.2. Background

D.1.2.A. Common FDM Defects and Detection Technologies

Some commonly observed issues in the FDM process, such as thermal inconsistencies, inferior gear feeding, filament winding, nozzle blockage, or poor bed leveling, result in certain defects in the parts being 3D printed and/or even unsuccessful prints at all [D.1]. Frequently observed defects during FDM printing were recently listed and summarized by He et al. [D.11]. Among those, warping, cracking, stringing, layer-shifting and off-platform types of defects are most commonly observed during FDM process [D.12]. In warping the contact surface of the part to the build plate forms a curve due to internal stress created by uneven cooling of layers [D.13]. Cracking usually occurs due to weak inter-layer bonding and results in 3D printed parts with irreversible damage [D.11]. Stringing is the defect where an excess amount of filament is deposited and thin strands between the different sections of prints are created [D.14]. Layer-shifting is the incorrect positioning of a layer in x-y plane relative to the previously printed layers [D.15]. Off-platform occurs due to failed bonding between the first layer of the print and the build plate [D.12]

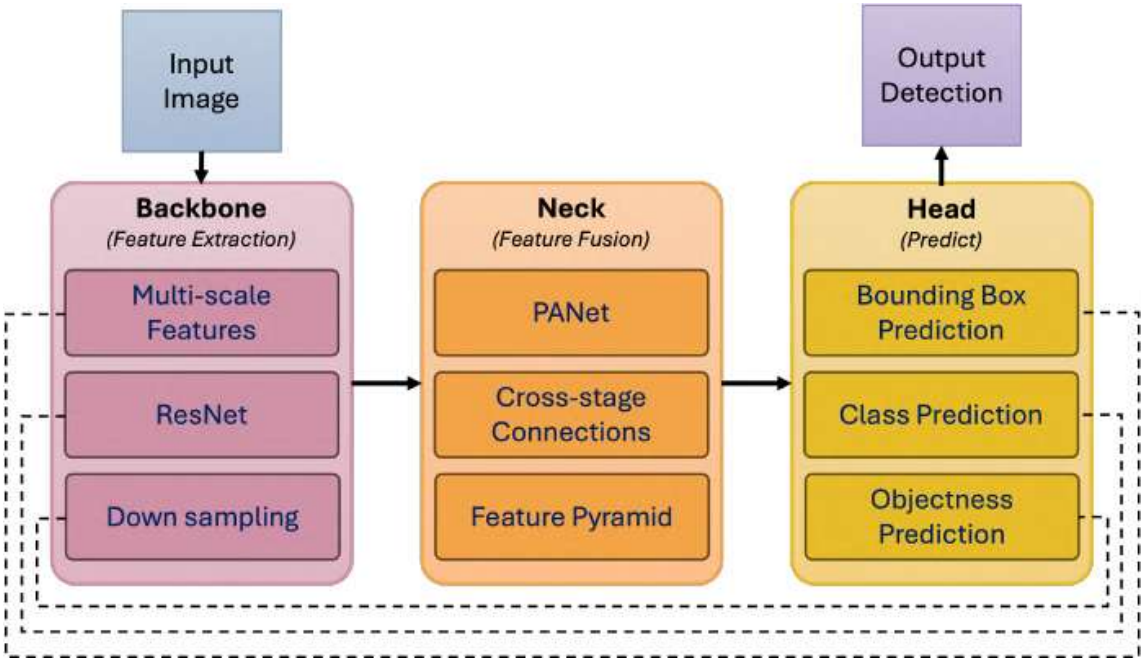

Figure D.1. YOLO architecture with labelled components: backbone for feature extraction, neck for feature refinement, and head for object detection tasks.

D.1.2.B. YOLO

YOLO, unlike traditional object detection models, employs a single-stage detection approach, enabling faster and more efficient real-time defect detection, thereby transforming the field of computer vision. On the other hand, like many other object detection algorithms, YOLO models can struggle with detecting relatively smaller objects in an image. YOLO models sometimes produce bounding boxes that include background pixels, affecting the accuracy of object localization [D.16]. YOLO divides an image into a grid and predicts bounding boxes and class probabilities directly for each grid cell in one pass through the network. It combines object localization and classification in one step [D.17]. YOLO architecture consists of three stages as shown in Figure D.1. The backbone in YOLO architecture is responsible for feature extraction from the input image. It consists of convolutional layers that process the image to generate feature maps, capturing essential spatial and semantic information. The neck acts as an intermediary between the backbone and the head. Its function is to refine and enhance the features extracted by the backbone. The head is where YOLO performs its actual object detection tasks [D.16].

D.1.2.C. Attention Mechanisms

Attention mechanisms in CNNs are techniques that help the network focus on more informative features in the spatial dimension. They improve CNN performance by strengthening channel-wise, spatial-wise, and domain attention [D.18].

1) Convolutional Block Attention Module: CBAM mechanism combines channel and spatial attention. Channel attention is applied through average-pooling and max-pooling followed by a shared MLP to generate channel-wise weights, while spatial attention applies pooling across

the channel axis to create a spatial map highlighting key regions. CBAM enhances feature representations by suppressing background noise and emphasizing diagnostically significant structures [D.19].

2) Squeeze-and-Excitation: SE mechanism refines feature maps by sequentially applying squeeze (global average pooling), excitation (two-layer gating to model channel dependencies), and re-weighting (emphasizing discriminative features). This approach dynamically optimizes channel-wise feature importance [D.20].

3) Efficient Channel Attention: ECA mechanism enables efficient cross-channel interaction without reducing the data. This improves the model's ability to focus on the most relevant features in an image, such as distinguishing small or similarlooking pests for real-time detection tasks [D.21].

4) Normalisation-based Attention Module: NAM is generated by applying a spatial attention mechanism to a feature map. The NAM highlights which spatial regions in the feature map are considered most important by the model [D.22].

5) Coordinate Attention: CA embeds precise positional information into the attention process, allowing the network to better capture both "what" and "where" aspects of objects within an image [D.23].

D.1.3. Research Methodology

The primary aim of this study is to evaluate the performance advantages of attention-augmented YOLO models for detecting printing defects in industry-ready settings. To achieve this, a systematic methodology is adopted to assess the efficacy of integrating attention mechanisms into YOLOv11, with YOLOv11 and YOLOv8 serving as baseline models for comparison.

D.1.3.A. Image Annotation

The dataset, sourced from [D.12], comprises 1,912 images of various printing defects, categorised into five initial defect classes including warping, stringing, and layer shifting. As the original dataset was unannotated, all images were manually annotated using the MATLAB Image Labeler toolbox. Several refinements were introduced during the annotation process. Firstly, the 'off-platform' class was relabelled as 'spaghetti' to more accurately reflect the visual characteristics of that defect. Additionally, a new class, 'curling,' was incorporated into the taxonomy. Notably, many images exhibited multiple co-occurring defects. While each image retained its original class-based assignment, additional defects were also annotated. Bounding boxes were drawn to encompass all visible defects within each image, thereby enabling multi-label object detection.

To ensure the accuracy and consistency of the annotations, both the classification of defect types and the delineation of bounding boxes were independently reviewed and validated by domain experts. The annotated final dataset comprises six classes of 3D printing defects: warping, spaghetti, cracking, stringing, layer shifting, and curling as shown in Figure D.2.

Figure D.2. Final annotated images illustrating various defect types. From top to bottom, the primary class (as the original dataset) for each row is: cracking, layer shifting, warping, stringing, and spaghetti (off-platform).

D.1.3.B. Data Preprocessing

Images were split into subsets using an 80/20 ratio for training and test, respectively. Then, to balance the class distribution among the training subset, targeted data augmentation was performed using geometric and photometric transformations such as flipping, rotation, scaling, affine shifts, and brightness/contrast adjustments [D.24]. Each class was augmented until it reached a label count similar to that of the most frequent class. However, since the 'warping' class also appeared in images primarily assigned to other defects, perfect balancing was not possible. In Table D.1, the defects and their counts before and after augmentation are presented.

Table D.1. Label counts

Defect Label	Before Augmentation	After Augmentation
warping	780	1211
spaghetti	155	830
cracking	417	921

stringing	474	911
layer shifting	380	937
curling	301	898

D.1.3.C. Implemented Attention-Augmented YOLOv11 Models

In this study, five distinct attention-augmented YOLOv11 models were benchmarked. For all models, the input tensor was of the shape [B, C, H, W]. Where B is the batch size, representing the number of input samples processed simultaneously. C is the number of channels, corresponding to different feature maps. H is the height of each feature map. W is the width of each feature map.

All the attention blocks were inserted directly after their respective blocks without altering the subsequent tensor dimensions or disrupting the original YOLOv11 structure. Inserting attention blocks into the backbone affects the feeding of the head block because it alters the size and appearance of the backbone. Thus, all the attention-augmented architectures were modified to maintain the same structure as the baseline.

The architecture of the implemented YOLO-CBAM model, illustrated in Figure C.3, follows the baseline head structure described above, with attention modules integrated into the backbone without altering tensor dimensions.

1) YOLO with Convolutional Block Attention Module (YOLO-CBAM): The implemented YOLO-CBAM consists of two modules: a channel attention module and a spatial attention module. The channel attention module uses global average pooling to squeeze the spatial dimensions, reducing the input tensor to [B, C, 1, 1]. This pooled output is flattened and passed through two linear layers with a ReLU activation in between. The first linear layer reduces the channel dimensionality by a given reduction ratio, and the second restores it.

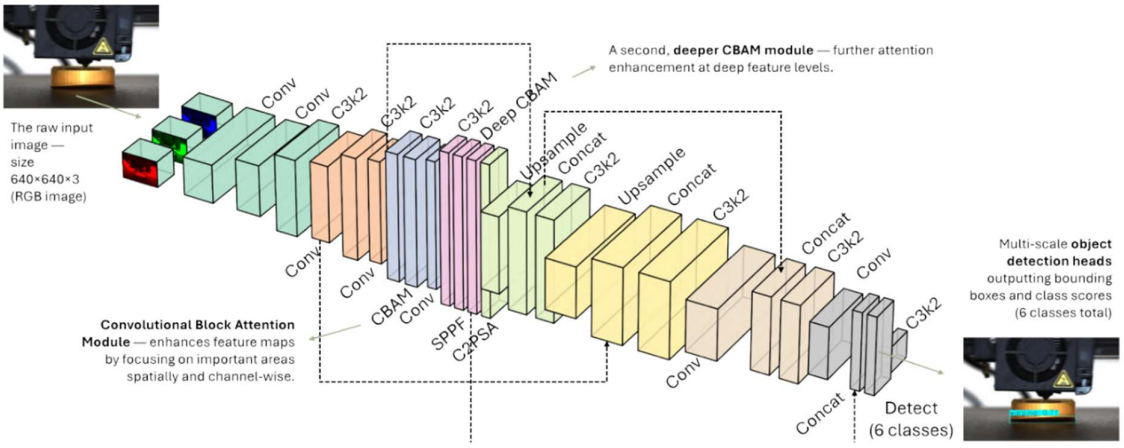

Figure D.3. YOLO-CBAM: YOLOv11 with integrated CBAM architecture

The result is passed through a sigmoid function and reshaped back to [*B, C,* 1*,* 1] to form a set of channel-wise attention weights. These weights are applied to the original input via element-wise multiplication, modulating the importance of each channel.

Next, the spatial attention module computes two spatial descriptors by performing average and max pooling operations along the channel axis, each producing a tensor of shape [*B,* 1*, H, W*]. These are concatenated along the channel dimension into a [*B,* 2*, H, W*] tensor and passed through a convolutional layer, followed by padding. The result is passed through a sigmoid function to produce a spatial attention map of shape [*B,* 1*, H, W*], which is then element-wise multiplied with the input from the channel attention stage. The final output has the same shape as the input.

CBAM blocks were integrated at two specific points within the backbone. A CBAM block was inserted after the second C3k2 block. Another CBAM block was inserted after the final C3k2 block before the SPPF block.

CBAM is introduced with the objective of enhancing feature representations by sequentially applying channel and spatial attention mechanisms. Channel attention aims to identify and amplify the most informative feature channels, while spatial attention aims to emphasize critical spatial regions within feature maps. By embedding these blocks after mid- and deepstage C3k2 blocks, the design was intended to guide the network to prioritize both important features and important spatial locations before multi-scale aggregation.

2) YOLO with Squeeze-and-Excitation (SE) Block (YOLO-SE): The SE block first applies a squeeze operation using global average pooling to the input tensor, reducing each channel to a scalar and producing a tensor of shape [*B, C,* 1*,* 1]. This is followed by an excitation operation, where the tensor passes through a lightweight two-layer bottleneck formed by two 1 × 1 convolutional layers. The first convolution reduces the number of channels by a given reduction ratio, followed by a ReLU activation, and the second convolution restores the number of channels to the original count. Then, the result is passed through a sigmoid function. Finally, the resulting attention tensor is multiplied element-wise with the original input tensor, producing an output tensor of the same shape as the input.

SE blocks were integrated at three points within the backbone. An SE block was inserted after the first C3k2 block. The second SE block was inserted after the second C3k2 block. The final SE block was inserted after the SPPF block.

SE is integrated with the aim of promoting channel-wise recalibration at different stages of feature extraction. By adaptively reweighting channel responses, the model is expected to suppress less informative features and highlight the most discriminative ones. This mechanism helps the network focus on useful channels across early, intermediate, and deep feature maps, thereby enriching representational capacity without modifying the spatial dimensions.

3) YOLO with Efficient Channel Attention (ECA) Block (YOLO-ECA): The ECA block first applies a squeeze operation using global average pooling, producing a tensor of shape [B, C, 1, 1]. The tensor is then reshaped to [B, 1, C] and passed through a one-dimensional convolution with a specified kernel size. The result is passed through a sigmoid function. Finally, the resulting attention tensor is reshaped back to [B, C, 1, 1] and multiplied element-wise with the original input tensor, resulting in an output tensor of shape [B, C, H, W].

The ECA blocks were integrated at three points within the backbone. The first ECA block was inserted after the first C3k2 block. The second ECA block was inserted after the second C3k2 block. The final ECA block was inserted after the C2PSA block.

ECA is integrated to encourage channel attention recalibration. Instead of introducing fully connected layers like SE, ECA employs a one-dimensional convolution to capture local cross-channel interactions efficiently. By embedding ECA at multiple stages — early, mid, and after the C2PSA block —the design aims to progressively refine channel importance across different depths of the network.

4) YOLO with Coordinate Attention (CA) Block (YOLOCA): The CA block first applies a coordinate pooling operation: global average pooling is performed separately along the width and height axes, resulting in two tensors of shapes [B, C, H, 1] and [B, C, 1, W], respectively. The height-pooled tensor is concatenated with a transposed version of the widthpooled tensor to form a combined tensor of shape [B, C, H +W, 1].

This combined tensor is passed through a shared bottleneck transformation consisting of a 1 × 1 convolution, batch normalisation, and a ReLU activation. The output is then split back into two branches corresponding to the height and width attention maps. Each branch passes through a separate 1 × 1 convolution to restore the original channel dimensions. Each branch is then passed through a sigmoid activation function. Finally, the original input tensor is element-wise multiplied with both the height and width attention maps. The resulting output tensor has the same shape as the input tensor.

CA blocks were integrated at two points within the backbone. The first CA block was integrated after the first C3k2 block. The second CA block was integrated after the SPPF block.

CA is integrated to encode positional information into the attention process, allowing the model to better localize salient features along spatial dimensions. By separately capturing width and height dependencies, the network aims to preserve fine-grained location information while performing channel recalibration. The integration after early and deep backbone modules was intended to enhance spatial sensitivity both at low- and high-level feature representations.

5) YOLO with normalisation-based Attention Module (NAM) (YOLO-NAM): The NAM block first applies instance normalisation to normalise each feature map individually across spatial dimensions. The normalised tensor is then passed through a 1 × 1 convolution that reduces the number of channels from C to 1, producing a spatial attention map. The result is passed through a sigmoid function. Finally, the original input tensor is element-wise multiplied with the generated spatial attention mask, resulting in an output tensor of the same shape [B, C, H, W].

NAM blocks were inserted at three points within the backbone. The first NAM block was integrated after the third C3k2 block. The second NAM block was integrated after the fourth C3k2 block. The final NAM block was integrated after the SPPF block. NAM is implemented with the goal of promoting spatial feature normalisation and selective emphasis. By applying instance normalisation followed by a learned spatial mask, NAM was intended to filter and enhance spatially significant regions. Their sequential placement after mid and deep C3k2 modules and after the SPPF block was intended to progressively guide spatial focus as feature maps advanced toward the detection heads.

D.1.3.D. Key Performance Indicators

The trained model is evaluated using the test split of the dataset, which contains labelled data with predefined ground truth bounding boxes. After making predictions on the test set, the model's outputs are compared against the ground truth annotations. A prediction is considered a True Positive (TP) if it correctly matches a ground truth object. If the model makes an incorrect prediction—such as detecting an object that doesn't exist or misclassifying it—it is counted as a False Positive (FP). A True Negative (TN) occurs when the model correctly identifies that no object is present where there is no ground truth annotation. If the model fails to detect an object that is present in the ground truth, it is recorded as a False Negative (FN). The proportion between TP detections and all detections (TP and FP) is defined as precision (P). Hence, the higher the precision, the better the prediction result.

The proportion between TP detections and all defects (TP and FN) is defined as recall (R). Hence, the higher the recall, the better the prediction result.

$$P = \frac{TP}{TP+FP} \quad R = \frac{TP}{TP+FN} \tag{D.1}$$

F1-Score is defined as the harmonic mean of the precision and recall.

$$F1 - Score = \frac{2}{{}^{1}/_{P} + {}^{1}/_{R}} \tag{D.2}$$

Intersection over Union (IoU) is an evaluation metric that measures the overlap between the prediction and the ground truth. mAP@0.5 is the mean Average Precision (mAP) across N classes when the IoU threshold is 0.5.

$$mAP@0.5 = \frac{1}{N}\sum_{i=1}^{N} AP(i) \tag{D.3}$$

mAP@0.5:0.95 is the mAP across N classes for IoU thresholds ranging from 0.5 to 0.95 in 0.05 increments.

$$mAP@0.5{:}\,0.95 = \frac{1}{10}\sum_{i=0.5}^{0.95} mAP@(i) \tag{D.4}$$

Specificity (S) is defined as the proportion of true negative predictions among all negative ground truth instances (TN + FP). Hence, the higher the specificity, the better the model is at avoiding false detections.

$$S = \frac{TN}{TN+FP} \tag{D.5}$$

D.1.4. Benchmark Results and Discussions

The selected models were trained using the Ultralytics framework with custom YAML configurations [D.25]. Each model was trained individually within a consistent environment, applying fixed parameters across all experiments. Specifically, all models, both with and without attention mechanisms, were trained for 50 epochs with a batch size of 64, using an input image size of 640 × 640 pixels. The AdamW optimizer was employed throughout the training process [D.26].

To minimize the impact of architectural variations and enable a fair comparison between attention-integrated models, 37 different architectures were created by systematically modifying the implementation locations of the attention blocks. In addition, targeted hyperparameter tuning was conducted, focusing solely on adjusting the kernel sizes and reduction ratios within the CBAM, SE, ECA, and CA modules. All other hyperparameters remained fixed across all experiments to ensure consistency.

The best results for ECA were achieved with a kernel size of 5. The best results for CA and SE were achieved with a reduction ratio of 16, and the best results for CBAM were achieved with a kernel size of 5 and a reduction ratio of 8. Following this process, the best-performing configuration for each attention mechanism was selected and subsequently used for benchmarking, thereby ensuring that performance comparisons reflected the optimized capabilities of each model rather than incidental architectural differences. In Section D.1.3.C, all given implementation architectures represent the best variations identified during these iterations.

The models were trained on a workstation equipped with an Intel i7-14700K CPU, 64 GB of RAM, and an NVIDIA RTX 4070 Ti GPU. To ensure consistency across results, evaluation was performed using the default tools provided by the Ultralytics framework. Validation metrics, including precision, recall, F1 score, mean Average Precision at IoU threshold 0.5 (mAP@0.5), and mean Average Precision across IoU thresholds from 0.5 to 0.95 (mAP@0.5:0.95), were reported individually for each class. Additionally, specificity per class was calculated from the confusion matrix, and Receiver Operating Characteristic (ROC) curves were generated based on the top-1 detection confidences for each class. The average detection time per image was also recorded using Python's timing libraries, providing an indication of the computational overhead introduced by each attention variant.

The training time for the baseline YOLOv8 was 12 minutes 52 seconds, and for the baseline YOLOv11 it was 13 minutes 20 seconds. The training times for CBAM, ECA, NAM, SE, and CA were 14 minutes 1 second, 14 minutes 6 seconds, 13 minutes 53 seconds, 14 minutes 15 seconds, and 14 minutes 7 seconds, respectively.

The average detection time per image for the baseline YOLOv8 was 0.0652 seconds, and for the baseline YOLOv11 it was 0.0654 seconds. The average detection times per image for CBAM, ECA, NAM, SE, and CA were 0.0664 second, 0.0663 seconds, 0.0666 seconds, 0.0678 seconds, and 0.0679 seconds, respectively.

Table D.2. Evaluation results for baselines and YOLOv11 models integrated with attention mechanisms

	YOLOv8 baseline	**YOLOv11 baseline**	**YOLOv11 CBAM**	**YOLOv11 CA**	**YOLOv11 SE**	**YOLOv11 ECA**	**YOLOv11 NAM**
Precision (%)	93.29	93.68	95.54	96.01	97.03	**97.28**	96.22
Recall (%)	89.74	87.82	91.55	90.32	90.63	**92.03**	90.65

F1 Score (%)	91.42	90.57	93.41	93.04	93.60	**94.67**	93.31
mAP@0.5 (%)	93.15	93.13	94.44	94.01	94.73	**95.64**	94.60
mAP@0.5:0.95 (%)	**61.20**	59.14	60.47	60.05	60.16	60.34	59.56
Specifity (%)	**99.09**	98.86	99.03	98.94	98.84	98.92	98.81

The evaluation results presented in Table D.2. demonstrate a clear performance improvement when attention mechanisms are integrated into the YOLOv11 architecture. Compared to the V8 and V11 baselines, all attention-augmented models achieved higher precision, recall, F1 scores, and mAP@0.5 values, indicating superior detection capability across classes. Notably, the ECA-enhanced model exhibited the highest precision (97.28%), recall (92.03%), and F1 score (94.67%), outperforming both the baseline models and other attention configurations. Similarly, the ECA-integrated model attained the highest mAP@0.5 value (95.64%), confirming its efficacy in accurately localizing objects across varying scales. Although the V8 baseline retained the highest mAP@0.5:0.95 score (61.20%), the marginal differences observed suggest that attention modules, while enhancing overall detection accuracy, may slightly compromise very fine-grained localization metrics. Specificity scores remained consistently high across all models, with minor variations, indicating that the introduction of attention mechanisms did not substantially affect the models' ability to correctly identify negative instances.

YOLOv11 introduces architectural enhancements over YOLOv8, including the use of C3k2 blocks and an attentionbased C2PSA module. However, baseline V11 has slightly underperformed compared to baseline V8. This is likely due to reduced feature richness in intermediate layers. V8 uses consistent C2f blocks with balanced expansion ratios, maintaining higher internal feature width (e.g., 128 hidden channels at 256 output), while V11 uses a mix of C3k2 configurations—some relying on narrower bottlenecks (e.g., 64 hidden channels with 0.25 expansion). This may explain its slightly better performance in precision-sensitive and finegrained localization tasks.

In examining the relative performance of the different attention mechanisms, it is evident that lightweight modules such as ECA and SE delivered notable gains with minimal computational overhead, compared to more complex modules like CBAM and CA. The ECA module, in particular, emerged as the most effective, striking an optimal balance between accuracy and model complexity. Conversely, the NAM-integrated model, while improving upon the baselines, exhibited slightly lower precision and mAP scores compared to ECA and SE, suggesting that the choice of attention mechanism significantly influences the detection performance. Overall, these results substantiate the hypothesis that incorporating attention mechanisms into the YOLOv11 backbone enhances feature representation, thereby leading to improved object detection outcomes without considerable degradation in computational efficiency.

Table D.3 presents the comparative F1 scores achieved by the baseline models and attention-augmented YOLOv11 variants across individual defect types. The results demonstrate that the integration of attention mechanisms consistently improves detection performance, particularly for more challenging classes such as spaghetti and curling. For instance, the YOLOv11 model enhanced with ECA achieved the highest F1 score of 92.88% for the spaghetti class, indicating a substantial improvement over the baseline models. Similarly, improvements were observed across other defect types, with the CBAM-integrated model achieving the best performance for layer shifting, and the CA-augmented model excelling in the detection of curling defects. Although the cracking class already exhibited near-perfect scores across all models, attention modules further stabilised detection performance, ensuring consistently high F1 values.

Table D.3. F1 Score comparison across individual defect types

	YOLOv8 baseline	**YOLOv11 baseline**	**YOLOv11 CBAM**	**YOLOv11 CA**	**YOLOv11 SE**	**YOLOv11 ECA**	**YOLOv11 NAM**
Warping	91.37	91.10	91.03	88.99	90.20	**92.00**	91.05
Spaghetti	73.12	71.40	86.92	84.07	89.59	**92.88**	85.67
Cracking	99.95	**99.96**	99.18	99.90	99.80	98.88	99.85
Stringing	94.41	93.63	93.03	93.62	**94.48**	94.42	93.09
Layer Shifting	99.31	98.69	**99.41**	98.08	98.28	98.44	99.31
Curling	90.34	88.64	90.87	**93.58**	89.28	92.44	90.87
Mean	91.42	90.57	93.41	93.04	93.60	**94.67**	93.31

The ROC-AUC curves presented in Figure D.4 provide a comparative evaluation of the models' discriminative capabilities across the individual defect classes. In general, all models exhibit high overall performance, with area under the curve (AUC) values exceeding 0.95 for the majority of classes, indicating excellent separability between defective and nondefective samples. Notably, the cracking and layer shifting classes consistently achieve near-perfect AUC scores (close to or exactly 1.0000) across all models, reflecting the relative ease of detecting these defects due to their distinct visual characteristics. Among the attention-augmented models, the YOLO-ECA variant demonstrated superior and consistently high AUC scores across all classes, particularly achieving an AUC of 0.9999 for the cracking class and 0.9997 for stringing, indicating exceptionally reliable classification performance. The NAM-integrated model also performed robustly, achieving the highest AUC for warping (0.9944) and maintaining strong scores across other classes. Importantly, the models integrating attention mechanisms notably improved the AUC for the more challenging spaghetti and curling classes when compared to the baseline models.

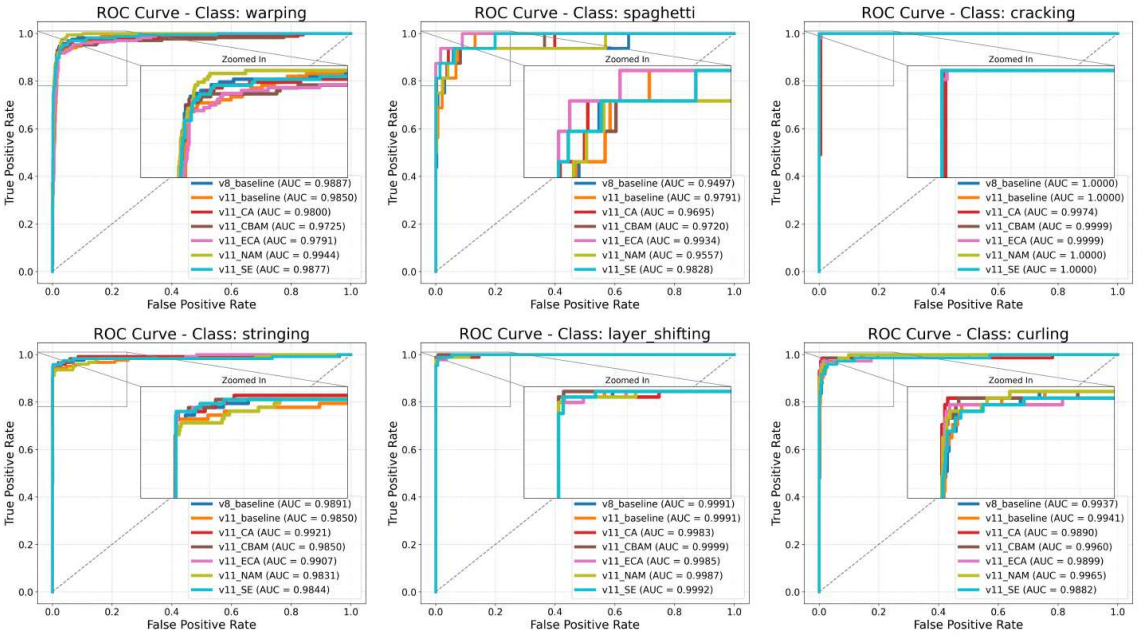

Figure D.4. ROC curves per defect class for baseline and attention-augmented YOLOv11 models

Based on the results, a sample detection batch from the ECA-integrated YOLO model, which achieved the best performance, is presented in Figure D.5. The images were taken from the test batch.

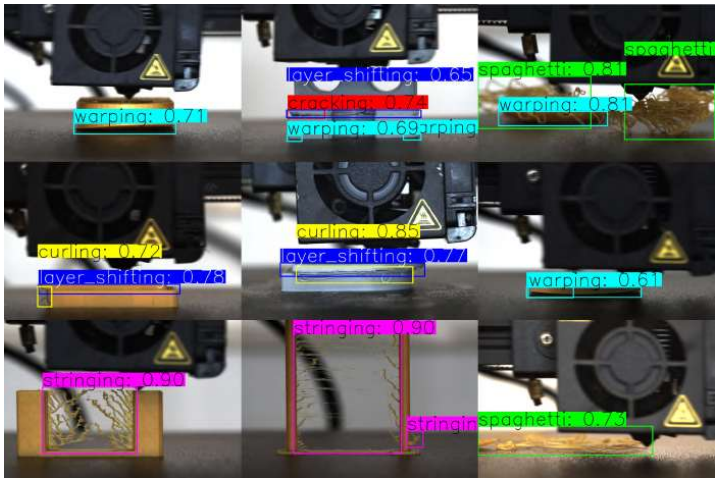

Figure D.5. Detected defects by YOLO-ECA model

In summary, this study presents a comprehensive framework for evaluating attention-augmented YOLO architectures in FDM 3D printing. The main contributions include benchmarking two baseline YOLO models (YOLOv8 and YOLOv11) and five attention-integrated YOLOv11 models (CBAM, SE, ECA, CA, NAM). While attention mechanisms significantly improve overall detection accuracy, they can introduce additional computational

overhead and may not uniformly benefit all defect types, particularly those requiring fine-grained localization.

D. References

[D.1] M. Baechle-Clayton, E. Loos, M. Taheri, and H. Taheri, "Failures and flaws in fused deposition modeling (fdm) additively manufactured polymers and composites," *Journal of Composites Science*, vol. 6, no. 7, p. 202, 2022.

[D.2] M. F. Khan, A. Alam, M. A. Siddiqui, M. S. Alam, Y. Rafat, N. Salik, and I. Al-Saidan, "Real-time defect detection in 3d printing using machine learning," *Materials Today: Proceedings*, vol. 42, pp. 521–528, 2021.

[D.3] O. A. Mohamed, S. H. Masood, and J. L. Bhowmik, "Optimization of fused deposition modeling process parameters: a review of current research and future prospects," *Advances in manufacturing*, vol. 3, pp. 42–53, 2015.

[D.4] K. Rajan, M. Samykano, K. Kadirgama, W. S. W. Harun, and M. M. Rahman, "Fused deposition modeling: process, materials, parameters, properties, and applications," *The International Journal of Advanced Manufacturing Technology*, vol. 120, no. 3, pp. 1531–1570, 2022.

[D.5] A.-M. Tal ˇ ˆınga, A. Had ˇ ar, M.-V. Dr ˇ agoi, I. Nisipeanu, H. A. Ali, and ˇ C. P. Suciu, "Yolo-v8 in capturing imperfections generated by changing 3d printer parameters," *U.P.B. Sci. Bull. Series C*, vol. 86, no. 4, 2024.

[D.6] U. Delli and S. Chang, "Automated process monitoring in 3d printing using supervised machine learning," *Procedia Manufacturing*, vol. 26, pp. 865–870, 2018, 46th SME North American Manufacturing Research Conference, NAMRC 46, Texas, USA.

[D.7] M. Hussain, "Yolo-v1 to yolo-v8, the rise of yolo and its complementary nature toward digital manufacturing and industrial defect detection," *Machines*, vol. 11, no. 7, p. 677, 2023.

[D.8] A. R. Sani, A. Zolfagharian, and A. Z. Kouzani, "Automated defects detection in extrusion 3d printing using yolo models," *Journal of Intelligent Manufacturing*, pp. 1–21, 2024.

[D.9] A. F. Rasheed and M. Zarkoosh, "Yolov11 optimization for efficient resource utilization," *arXiv preprint arXiv:2412.14790*, 2024.

[D.10] N. Jegham, C. Y. Koh, M. Abdelatti, and A. Hendawi, "Evaluating the evolution of yolo (you only look once) models: A comprehensive benchmark study of yolo11 and its predecessors," *arXiv preprint arXiv:2411.00201*, 2024.

[D.11] H. He, Z. Zhu, Y. Zhang, Z. Zhang, T. Famakinwa, and R. Yang, "Machine condition monitoring for defect detection in fused deposition modelling process: a review," *The International Journal of Advanced Manufacturing Technology*, vol. 132, no. 7, pp. 3149–3178, 2024.

[D.12] W. Hu, C. Chen, S. Su, J. Zhang, and A. Zhu, "Real-time defect detection for fff 3d printing using lightweight model deployment," *The International Journal of Advanced Manufacturing Technology*, vol. 134, no. 9, pp. 4871–4885, 2024.

[D.13] K. Singh, “Experimental study to prevent the warping of 3d models in fused deposition modeling,” *International Journal of Plastics Technology*, vol. 22, no. 1, pp. 177–184, 2018.

[D.14] O. Charia, H. Rajani, I. Ferrer Real, M. Domingo-Espin, and N. Gracias, “Real-time stringing detection for additive manufacturing,” *Journal of Manufacturing and Materials Processing*, vol. 9, no. 3, p. 74, 2025.

[D.15] K. Erokhin, S. Naumov, and V. Ananikov, “Defects in 3d printing and strategies to enhance quality of fff additive manufacturing. a review,” *ChemRxiv*, 2023.

[D.16] T. Diwan, G. Anirudh, and J. V. Tembhurne, “Object detection using yolo: Challenges, architectural successors, datasets and applications,” *Multimedia Tools and Applications*, vol. 82, no. 6, pp. 9243–9275, 2023.

[D.17] A. Vijayakumar and S. Vairavasundaram, “Yolo-based object detection models: A review and its applications,” *Multimedia Tools and Applications*, vol. 83, no. 35, pp. 83 535–83 574, 2024.

[D.18] W. Li, K. Liu, L. Zhang, and F. Cheng, “Object detection based on an adaptive attention mechanism,” *Scientific Reports*, vol. 10, no. 1, p. 11307, 2020.

[D.19] J. Yan, Y. Zeng, J. Lin, Z. Pei, J. Fan, C. Fang, and Y. Cai, “Enhanced object detection in pediatric bronchoscopy images using yolo-based algorithms with cbam attention mechanism,” *Heliyon*, vol. 10, no. 12, 2024.

[D.20] K. A. Gladis, J. B. Madavarapu, R. R. Kumar, and T. Sugashini, “In-out yolo glass: Indoor-outdoor object detection using adaptive spatial pooling squeeze and attention yolo network,” *Biomedical Signal Processing and Control*, vol. 91, p. 105925, 2024.

[D.21] Z. Tang, J. Lu, Z. Chen, F. Qi, and L. Zhang, “Improved pest-yolo: Realtime pest detection based on efficient channel attention mechanism and transformer encoder,” *Ecological Informatics*, vol. 78, p. 102340, 2023.

[D.22] H. Ahn, S. Son, J. Roh, H. Baek, S. Lee, Y. Chung, and D. Park, “Safpyolo: Enhanced object detection speed using spatial attention-based filter pruning,” *Applied Sciences*, vol. 13, no. 20, p. 11237, 2023.

[D.23] Y. Li, M. Zhang, C. Zhang, H. Liang, P. Li, and W. Zhang, “Yolo-ccs: Vehicle detection algorithm based on coordinate attention mechanism,” *Digital Signal Processing*, vol. 153, p. 104632, 2024.

[D.24] C. Santos, M. Aguiar, D. Welfer, and B. Belloni, “A new approach for detecting fundus lesions using image processing and deep neural network architecture based on yolo model,” *Sensors*, vol. 22, no. 17, p. 6441, 2022.

[D.25] R. G. Baldovino, A. J. P. Vidad, R. P. B. Abastillas, N. T. Bugtai, E. P. Dadios, R. R. P. Vicerra, A. A. Bandala, A. R. See, and N. R. Roxas Jr, “Comprehensive analysis on ultralytics-supported yolo models for detection and recognition of large office objects for indoor navigation,” *Procedia Computer Science*, vol. 246, pp. 3851–3858, 2024.

[D.26] R. Llugsi, S. El Yacoubi, A. Fontaine, and P. Lupera, “Comparison between adam, adamax and adam w optimizers to implement a weather forecast based on neural networks for the andean city of quito,” in *2021 IEEE Fifth Ecuador Technical Chapters Meeting (ETCM)*. IEEE, 2021, pp. 1–6.